

THESIS FOR THE DEGREE OF LICENTIATE OF PHILOSOPHY

Atomic scale modeling of  
ordering phenomena in inorganic clathrates

MATTIAS ÅNGQVIST

*Department of Physics*

CHALMERS UNIVERSITY OF TECHNOLOGY

Göteborg, Sweden 2018

Atomic scale modeling of  
ordering phenomena in inorganic clathrates  
MATTIAS ÅNGQVIST

© Mattias Ångqvist, 2018

Department of Physics  
Chalmers University of Technology  
SE-412 96 Göteborg, Sweden  
Telephone +46 31 772 10 00

Cover: 3D-rendering of a type I clathrate. The rendering was created in Blender.

Chalmers reproservice  
Göteborg, Sweden 2018

# Atomic scale modeling of ordering phenomena in inorganic clathrates

MATTIAS ÅNGQVIST  
*Department of Physics*  
Chalmers University of Technology

---

## Abstract

Ordering phenomena in materials often have a crucial impact on materials properties. They are governed by the competition between entropy and energy. Accordingly simulating these aspects requires the construction of models that enable an computationally efficient exploration of the relevant configuration space. Alloy cluster expansions are a technique that is particular suitable for this task as they can be trained to reach high accuracy while being computationally suitable for rapid sampling via Monte Carlo techniques.

In this thesis alloy cluster expansions have been applied in combination with Monte Carlo simulations to study the ordering behavior in various inorganic clathrates. Inorganic clathrates constitute a class of systems with a cage-like framework that can trap loosely bound atoms or even small molecules. These systems are small band gap semiconductors and have a very low lattice thermal conductivity, which gives rise to very good thermoelectric properties. Additionally the host atoms and cage framework can be occupied by a wide range of elements which provides extensive opportunities for property optimization. Inorganic clathrates are thus good examples for systems with a high degree of variability in composition, for which ordering phenomena play a crucial role.

In paper I we studied the ordering behaviour of  $\text{Ba}_8\text{Ga}_{16}\text{Ge}_{30}$ . Configurations representative for different annealing temperatures were extracted from Monte Carlo simulations and further analyzed to obtain the temperature dependency of the thermoelectric power factor. These data was subsequently used to construct a cluster expansion for the power factor itself, which enabled us to optimize the chemical ordering that maximizes this property. The approach developed in this work is generalizable and can be adapted to other materials.

In paper II we studied the ordering behavior and related properties in the clathrate systems  $\text{Ba}_8\text{Al}_x\text{Si}_{46-x}$ ,  $\text{Ba}_8\text{Al}_x\text{Ge}_{46-x}$ ,  $\text{Ba}_8\text{Ga}_x\text{Ge}_{46-x}$ , and  $\text{Ba}_8\text{Ga}_x\text{Si}_{46-x}$  as a function of composition and temperature. We achieved very good agreement with the available experimental data for the site occupancy factors (SOFs). This enabled us to reconcile experimental data from different sources and explain the non-monotonic variations of the SOFs. In particular, we provided a rationale for the extreme SOF behavior with varying composition observed in Al based clathrates.

**Keywords:** Cluster expansion, Monte Carlo, Inorganic clathrates, ordering phenomena

## LIST OF PUBLICATIONS

This thesis consists of an introductory text and the following papers:

**I Optimization of the Thermoelectric Power Factor: Coupling between Chemical Order and Transport Properties**

Mattias Ångqvist, Daniel O. Lindroth and Paul Erhart  
Chemistry of Materials **28**, 6877 (2016)

**II Understanding Chemical Ordering in Intermetallic Clathrates from Atomic Scale Simulations**

Mattias Ångqvist and Paul Erhart  
Chemistry of Materials **29**, 7554 (2017)

Specification of the authors contribution to the publications:

- I The author developed the software for constructing and sampling cluster expansions used in the paper. The author constructed the cluster expansions, carried out the Monte Carlo simulations and the associated analysis, and created all figures related to Monte Carlo and cluster expansions.
- II The author developed the software for constructing and sampling cluster expansions used in the paper. The author constructed the cluster expansions, carried out the Monte Carlo simulations and associated analysis, and prepared all figures related to Monte Carlo and cluster expansions. The author also wrote the first draft of the paper.



# Contents

|          |  |           |
|----------|--|-----------|
| <b>1</b> | <b>Introduction</b>                          | <b>1</b>  |
| 1.1      | Ordering phenomena                           | 1         |
| 1.1.1    | Entropy and order                            | 1         |
| 1.1.2    | Free energy                                  | 2         |
| 1.1.3    | Examples                                     | 3         |
| 1.2      | Mixing in multi-component systems            | 3         |
| 1.2.1    | The dilute limit                             | 3         |
| 1.2.2    | Concentrated solutions: Mean-field treatment | 4         |
| 1.2.3    | Concentrated solutions: Beyond mean-field    | 4         |
| 1.3      | Thesis guide                                 | 6         |
| <b>2</b> | <b>Inorganic clathrates</b>                  | <b>7</b>  |
| 2.1      | Crystal structure                            | 7         |
| 2.2      | The Zintl concept                            | 8         |
| 2.3      | Ordering                                     | 9         |
| 2.3.1    | Empirical rules for SOFs                     | 9         |
| 2.3.2    | Guideline for variations of SOFs             | 10        |
| <b>3</b> | <b>Alloy cluster expansions</b>              | <b>11</b> |
| 3.1      | Introduction                                 | 11        |
| 3.2      | Definition of a cluster                      | 12        |
| 3.3      | Formal theory                                | 14        |
| 3.3.1    | Point functions                              | 14        |
| 3.3.2    | Orthogonal basis                             | 14        |
| 3.3.3    | Further considerations                       | 15        |
| 3.3.4    | Symmetrically indistinct clusters            | 16        |
| 3.4      | Construction of a cluster expansion          | 17        |
| 3.5      | Compressive sensing                          | 18        |
| 3.5.1    | Split Bregman algorithm                      | 18        |
| 3.6      | Cross-validation                             | 19        |
| 3.6.1    | Leave-one-out cross validation               | 20        |

|          |  |           |
|----------|--|-----------|
| 3.6.2    | k-fold cross validation . . . . .                  | 20        |
| 3.7      | Cluster expansion for a binary system . . . . .    | 21        |
| <b>4</b> | <b>Monte Carlo simulations</b>                     | <b>23</b> |
| 4.1      | Monte Carlo integration . . . . .                  | 23        |
| 4.2      | Importance sampling . . . . .                      | 24        |
| 4.3      | Thermodynamic integration on the lattice . . . . . | 24        |
| 4.4      | The Metropolis algorithm . . . . .                 | 25        |
| 4.4.1    | Markov chain Monte Carlo . . . . .                 | 25        |
| 4.5      | Probability of a state . . . . .                   | 28        |
| 4.6      | The canonical ensemble . . . . .                   | 29        |
| 4.7      | Semi-grand canonical ensemble . . . . .            | 30        |
| 4.8      | Validity of lattice based models . . . . .         | 30        |
| <b>5</b> | <b>Summary of the papers</b>                       | <b>33</b> |
| 5.1      | Paper I . . . . .                                  | 33        |
| 5.2      | Paper II . . . . .                                 | 34        |
|          | <b>Acknowledgments</b>                             | <b>35</b> |
|          | <b>Bibliography</b>                                | <b>37</b> |
|          | <b>Papers I-II</b>                                 | <b>41</b> |

# Introduction

## 1.1 Ordering phenomena

This thesis deals with ordering phenomena in inorganic clathrates. The ordering in a material is dictated by the energetics and the entropy of the material. Common methods used to model mixtures in multi-component systems is demonstrated in this chapter. It will be shown that in order to model the ordering of complex materials the best available models are required.

### 1.1.1 Entropy and order

Entropy is a measure of the disorder in a system. The second law of thermodynamics states that disorder in a closed system can only increase; in other words closed systems tend to evolve from ordered to disordered states. A simplified example of this is the process of shuffling a fresh deck of cards. The initial state when the deck of cards are in perfect order will “never” appear again in the process of the shuffling since, assuming random shuffling, the probability to end up in the initial state are roughly 1 in  $10^{68}$ . As the shuffling continues the deck of cards becomes more and more disordered.

Another example is the tossing of coins. Imagine having 100 coins and tossing them all at once. A particular sequence can be denoted as head–tail–head–head–... and so on. The probability that all come up heads is the probability of the first coin coming up as heads times the probability that the second coin comes up as heads and so on, hence the probability is  $(1/2)^{100}$ . This probability is the same for any sequence of the coin toss. Yet from intuition we would expect that all coins coming up as heads should almost never happen.

The resolution to this conundrum lies in the distinction of a specific sequence of coin tosses, called microstates, and the total number of heads and tails of a particular sequence, called a macrostate. All microstates are equally probable but the probabilities for different macrostates vary over a wide range. The probability of the macrostate is the number of all microstates that correspond to that macrostate divided by the number of all possible microstates. The number of total microstates are  $2^{100}$  and the number of microstates for a macrostate is given by  $\binom{100}{n} = 100! / n! (100 - n)!$ . Consequently the probability of all coins ending up as heads is  $1/2^{100}$  whereas the probability of ending up with 50 heads is  $10^{29}$  more likely with a probability of about  $10^{29}/2^{100}$ . Note that the number of microstates for a particular macrostate is commonly referred to as the multiplicity of that macrostate.

Mathematically entropy is measured as  $S = k_B \ln \Omega$ , where  $S$  is the entropy,  $k_B$  is the Boltzmann constant and  $\Omega$  is the multiplicity of the system. Hence increasing the entropy, or the disorder, simply implies that the system has changed to a more likely state.

The principles of the coin toss example are easily extended to atomic systems. Imagine a system comprised of 100  $A$  atoms. By mixing one  $B$  atom into the system the number of possible microstates increases by a factor of 100, as there are 100 possible sites to insert the  $B$  atom. A system of atoms obeys the same combinatorics as the coin flipping. Hence the entropy increases by mixing and if we are neglecting the atomic interactions the system will have a tendency to spontaneously start mixing.

### 1.1.2 Free energy

Entropy goes a long way in explaining the ordering behaviour of materials. Yet, in nature many materials are observed to exhibit ordered states, which have (much) lower entropy than disordered states. Thus if entropy is one half of the picture to explain disordering, the energy is the other half that has to be included. Consider again the case of the  $AB$  atomic system, for which we saw that the entropy can be tremendously increased by mixing  $A$  and  $B$  atoms. In general there is an energetic cost associated with mixing. If the formation of  $A - B$  bonds is energetically unfavorable compared to  $A - A$  and  $B - B$  bonds there is a penalty for mixing and less mixing is expected. On the other hand if  $A - B$  bonds are more favorable, the system can both lower its energy and increase its entropy by mixing and more mixing is expected. This interplay of entropy and energy is expressed in the Helmholtz free energy of the system

$$F = U - TS, \tag{1.1}$$

where  $U$  is the internal energy and  $T$  is the temperature. Generally speaking a system described in the canonical ensemble will strive to minimize its free energy. According to Eq. (1.1) the entropy term becomes more important for higher temperatures. Hence, at a low temperature a system is more likely to be observed in its low energetic state, where the chemical bonds dictate the ordering of the material. As the temperature is increased, however, the material becomes more disordered.

### 1.1.3 Examples

Many materials can exhibit some form of chemical order which are crucial to understanding their properties. One example is  $\text{Zn}_4\text{Sb}_3$  which is a material with a high thermoelectric figure of merit, which is partially due to its low thermal conductivity [1]. It has been identified that the source of this low thermal conductivity is due to Zn disorder and Zn nanostructuring which are sources of phonon scattering [2, 3, 4].

Skutterudites are another example of material with chemical order, which are a type of cage like materials which are high performance thermoelectric materials [5, 6, 7, 8, 9]. The skutterudites owe some of its success as good thermoelectric materials from their low thermal conductivity. These materials can lower their thermal conductivity by filling these voids with rare earth metals [10, 11]. It has been observed that the minima of the thermal conductivity is obtained for a partial filling of the voids for some skutterudites [7]. An understanding of how these filler atoms order can thus be very helpful in order to design optimal skutterudites [12].

Yet another example of thermoelectric materials with chemical ordering are the inorganic clathrates. The clathrates possesses a large unit cell which can support a wide range of elemental components and compositions. The ordering in inorganic clathrates show large variations with compositions and constituent atoms [13, 14, 15]. The power factor, which is an integral part of thermoelectric efficiency, has been demonstrated to be able to be optimized by more than 60% for certain chemical ordering patterns [16]. Inorganic clathrates are described in more detail in chapter 2.

## 1.2 Mixing in multi-component systems

### 1.2.1 The dilute limit

Consider a system of  $N$  particles where all particles are of type  $A$  except for  $n$  particles of type  $B$ . This system is said to be in the dilute limit if  $N \gg n$ . In the dilute limit the  $B$  particles are so few and spread out so it is assumed that interactions between  $B$  particles can be neglected. Hence,  $\Delta F$ , the free energy associated with adding or subtracting a  $B$  particle, is constant as a function of

composition. The equilibrium concentration in the dilute limit is then given by  $c = c_0 \exp[-\Delta F/k_B T]$ , where  $c_0$  is the concentration of sites available for substitution.

### 1.2.2 Concentrated solutions: Mean-field treatment

When the condition  $N \gg n$  is no longer fulfilled the system is said to be in the concentrated limit. Here, the  $B$  atoms have become so numerous that their mutual interaction must be taken into account and the free energy of adding or removing a  $B$  atom becomes dependent of the concentration. The simplest treatment applied in the concentrated limit is provided by the mean field approximation to the Ising model. The energy, entropy and the free energy of the system can be expressed in terms of an order parameter, which describes, e.g., the average number of  $A - B$  bonds in the structure. The order parameter observed for a certain temperature and concentration is the one that minimizes  $F$ . The Helmholtz free energy of the system is given by [17, 18]

$$\begin{aligned}\Delta F_{\text{mix}} &= \Delta U_{\text{mix}} - T\Delta S_{\text{mix}}, \\ \Delta U_{\text{mix}} &= \omega c(1 - c), \\ \Delta S_{\text{mix}} &= -k_B [c \ln c + (1 - c) \ln (1 - c)],\end{aligned}\tag{1.2}$$

where  $\omega$  describes the energy cost of mixing and creating an  $A - B$  bond,  $c$  is the  $B$  concentration and  $k_B$  is the Boltzmann constant. The effects of  $\Delta U_{\text{mix}}$  and  $T$  on  $\Delta F_{\text{mix}}$  are illustrated in Fig. 1.1. Some comments are in order. First, all expressions are symmetric in the concentration  $c$ . Secondly, the mixing entropy,  $\Delta S$ , is positive across the entire concentration range. Consequently the contribution of entropy to the free energy is always negative. Hence, for  $T \rightarrow \infty$ , entropy will be the dominating term and the free energy will always be minimized by mixing ( $\Delta F_{\text{mix}} < 0$ ). For the case of  $\Delta U_{\text{mix}} > 0$  there is a competition between energy and entropy that determines whether the components mix or segregate. For  $\Delta U_{\text{mix}} > 0$  and low  $T$ ,  $\Delta F_{\text{mix}}$  can change sign, giving rise to a miscibility gap (Fig. 1.1d).

This very simple form is not suitable for modeling the vast majority of systems. It can, however, be generalized leading to the semi-empirical CALPHAD approach to modeling phase diagrams. In this case, the various contributions to the mixing energy and entropy are expressed in polynomial expansions in temperature and composition. The expansion coefficients are most commonly obtained by fitting to experimental data and, more recently, also from first-principles calculations. The resulting models are widely used in industry for alloy design and optimization.

### 1.2.3 Concentrated solutions: Beyond mean-field

The mean-field approach outlined in the previous section is fundamentally semi-empirical in its nature and requires input in the form of either experimental or

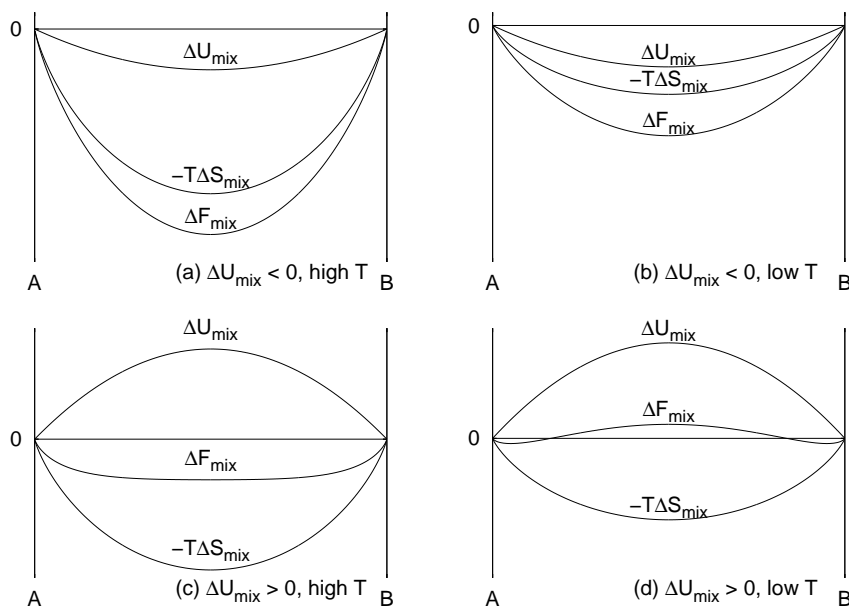


Figure 1.1: The free energy of mixing  $\Delta F_{\text{mix}}$  as a function of composition assuming mixing is (a,b) energetically favorable ( $\Delta U_{\text{mix}} < 0$ ) and (c,d) unfavorable ( $\Delta U_{\text{mix}} > 0$ ), respectively, at (a,c) high and (b,d) low temperature  $T$ .

computational data. Experimental data is often difficult and/or expensive to acquire; there are also various cases, in which it is downright impossible to extract meaningful data from experiments. This applies for example at low temperatures when thermodynamic equilibrium cannot be reached reliably.

For illustration consider the W–Ti system as analyzed using a combination of first-principles calculations, lattice models and Monte Carlo simulations. The analysis reveals a ground state structure at 80% tungsten concentration [19]. At low temperatures this configuration is much more likely to be observed than other configurations leading to a distinct feature in the mixing energy (Fig. 1.2a) and even more so the mixing entropy (Fig. 1.2b). These features are absent in CALPHAD assessments of the W–Ti system, which instead commonly assume complete immiscibility, i.e. a positive mixing energy throughout. This approximation is owed to the fact that W is a refractory metal, which renders experimental data below approximately 1300 K unreliable.

The combination of first-principles calculations (commonly [density functional theory \(DFT\)](#)) and lattice models (usually [alloy cluster expansions \(CEs\)](#)) allows one to accurately predict the behavior of multi-component mixtures with little or no experimental input. In the present thesis the application range of these techniques is further extended to analyze ordering in inorganic clathrates.

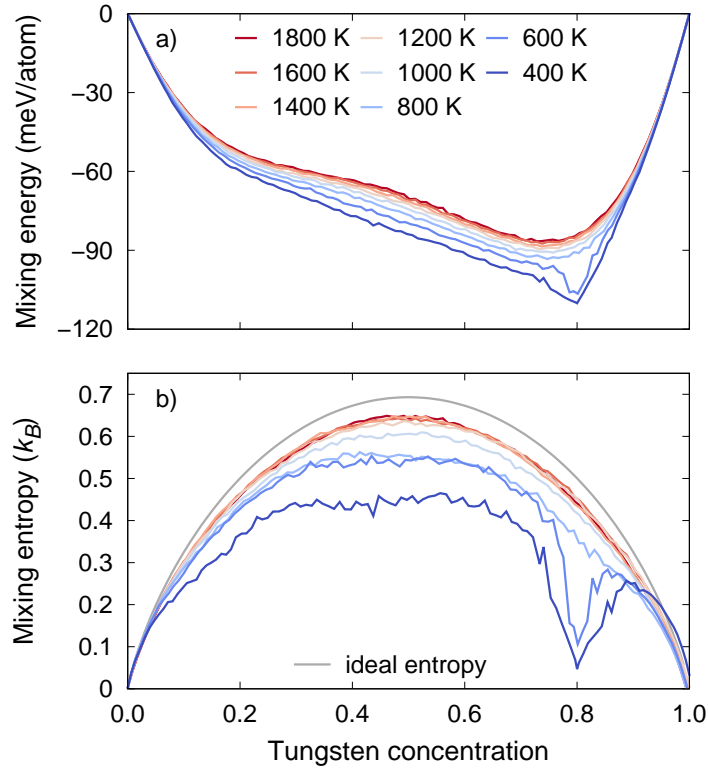


Figure 1.2: (a) Mixing energy and (b) mixing entropy as a function of composition.

### 1.3 Thesis guide

In this thesis a series of inorganic clathrates (chapter 2) has been investigated. Clathrates are inclusion compounds with complex ordering of the constituent atoms. For the systems of interest in this work, there are  $\binom{46}{16} \approx 10^{12}$  possible ways to place the atoms in the unit cell, excluding symmetry. One therefore requires extremely efficient means to evaluate the energies of different configurations in order to investigate the vast configurational space of these systems. In this work this is achieved by means of cluster expansions (chapter 3) while Monte Carlo simulations are employed to obtain thermodynamical averages (chapter 4). The results of this work have been published in two peer-reviewed journal articles (chapter 5).

# Inorganic clathrates

Inorganic clathrates constitute a class of inclusion compounds that exhibit a cage-like framework in which the cages are occupied by guest atoms or small molecules [20, 21]. The guest atoms, which are undersized relative to their respective cage, can act as so-called rattlers, lowering the lattice thermal conductivity. The framework structure can support a rather wide range of compositions, from binary systems to ternary and higher order. The availability of different compositions and the resulting variability of the distribution of elements in the framework provide opportunities for optimizing material properties. Inorganic clathrates have been studied in particular as potential high-performance thermoelectric materials due to their low intrinsic thermal conductivity [22, 23], suitable band gap [24, 25, 26], good dopability, and compositional variability [13].

## 2.1 Crystal structure

Inorganic clathrate can be categorized according to their symmetry [20, 21]. The present thesis focuses on type I clathrates, which have received the most attention so far (Fig. 2.1). The framework structure of type I inorganic clathrates contains 46 tetrahedrally coordinated host atoms in the unit cell. It is the geometrical arrangement of these 46 atoms that provides eight voids (or cages) per unit cell for the guest atoms. There are two smaller dodecahedral cages and six larger tetrakaidecahedral cages. The crystal structure belongs to the cubic space group  $Pm\bar{3}n$ . In Wyckoff notation the center of the cages are  $2a$  and  $6d$  for the dodecahedral and tetrakaidecahedral cages, respectively, whereas the framework atoms occupy Wyckoff sites  $6c$ ,  $16i$  and  $24k$ .

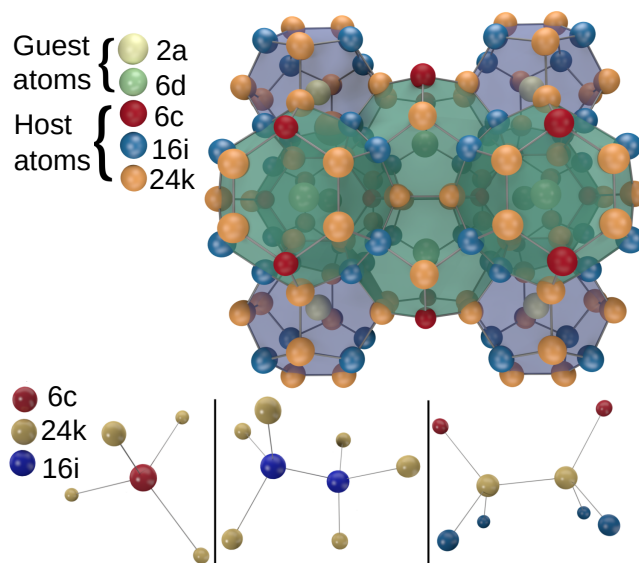


Figure 2.1: Crystal structure of type I clathrates. The guest species (Ba) occupies Wyckoff sites of type  $2a$  and  $6d$ , while the host species (Ga, Al, Ge, Si) occupy Wyckoff sites of type  $6c$ ,  $16i$ , and  $24k$ . The configurations in the bottom row illustrate the environments for  $6c$ ,  $16i$ , and  $24k$  sites, respectively.

## 2.2 The Zintl concept

The Zintl concept provides a rationale for the stoichiometry of semiconducting clathrates. It requires four electrons to be available for each tetrahedrally bonded host atom, while the guest atom is assumed to donate its valence electrons to the host framework. The number of electrons required to form bonds between the 46 host atoms is thus 184.

The general formula for type I clathrates is  $A_8M_xM'_{46-x}$ . The clathrates studied in this thesis are comprised of Ba, Ga/Al, Ge/Si for A, M and M' respectively. Each Ba atom can donate two electrons, whereas Ga/Al and Ge/Si provide three and four valence electrons, respectively. Therefore, for  $x = 16$  all bonds saturated. Lowering the Ga/Al composition thus leads to electron deficiency and the material is expected to be n-doped. Likewise, increasing the Ge/Si concentration creates a p-doped material. As a thermoelectric element requires both an n-doped and p-doped material to function, clathrates can in principle achieve both of these limits by variation of the composition.

## 2.3 Ordering

The host framework of inorganic clathrates usually comprises several different Wyckoff sites (in the present work  $6c$ ,  $16i$ , and  $24k$ ), which occupied by several different species (here Ga, Ge, Si, Al). If the different sites were occupied statistically one would expect for a stoichiometric sample ( $x = 16$ )  $16/46 \approx 35\%$  of the sites to be occupied by Al or Ga. Measurements of the so-called **site occupancy factors (SOFs)** reveal, however, dramatic deviations from this average [13]. The deviation from an entropically desirable random occupation (i.e., 35%) indicates that the interaction between the constituents plays a crucial role and the experimentally observed ordering (i.e. **SOFs**) arise from a competition of energy and entropy.

The **SOFs** vary between the compounds and can also show strong, non-monotonic variations with the stoichiometry [13, 14, 15]. Furthermore, the **SOFs** show an impact on transport properties [16]. Hence, understanding the ordering of these materials is crucial for understanding their thermoelectric performance.

### 2.3.1 Empirical rules for SOFs

A set of guideline rules for the **SOFs** has been formulated on the basis of a range of experimental data [13]. They are mostly based on the environment of each Wyckoff site and the observation that direct bonds between trivalent atoms species are unfavorable. There are three different bonding environments, one for each Wyckoff site. The  $6c$  sites have four  $24k$  sites as nearest neighbors; the  $24k$  sites have one  $6c$  site, two  $16i$  sites and one  $24k$  site as nearest neighbors; finally, the  $16i$  sites have three  $24k$  site and one  $16i$  site as nearest neighbors.

The geometry of the lattice thus leads to the following set of rules.

1. A  $6c$  site has no other  $6c$  sites in its surrounding and hence  $6c < 100\%$ .
2. The same argument can be made to the other two sites giving  $24k < 50\%$  and  $16i < 50\%$  since there is one  $24k - 24k$  and one  $16i - 16i$  pair per  $24k$  site and  $16i$ , respectively.
3. Furthermore,  $6c + 24k < 100\%$  since the  $6c$  site binds to four  $24k$  sites and the sum of the **SOFs** should be below 100%.
4. Also  $16i + 24k \leq 50\%$ . As pointed out in Ref. [14], however, this rule is too restricted and the condition to avoid trivalent nearest neighbors is actually  $16i + 24k \leq 83.3\%$ .

The violation of the last rule can also be seen in papers I and II in this thesis, where we present ground state **SOFs** with no trivalent nearest neighbor and  $16i + 24k = 56.25\%$ . With that small modification, the rules, based on simple assumptions, are in good agreement with the experimental data.

### 2.3.2 Guideline for variations of SOFs

The rules described above cannot provide a direct rationale for explaining the *variations* in the SOFs as a function of composition. Different components in the framework structure will show different variations due to composition [15]. Here, atomic scale simulation, e.g., based on cluster expansions parametrized using first-principles calculations, provide a way to obtain very detailed information [16, 27, 15]. In Ref. [15] it was found that Al-based clathrates ( $\text{Ba}_8\text{Al}_x\text{Ge}_{46-x}$ ,  $\text{Ba}_8\text{Al}_x\text{Si}_{46-x}$ ) exhibit a strong, non-monotonic variation of the SOFs with Al content, whereas Ga-based clathrates ( $\text{Ba}_8\text{Ga}_x\text{Ge}_{46-x}$ ,  $\text{Ba}_8\text{Ga}_x\text{Si}_{46-x}$ ) show a monotonic dependence on Ga content. It was argued that the differences observed were largely due to the Al–Al repulsion being twice as strong as the Ga–Ga repulsion. In other words, the Al-based clathrates demonstrate a more extreme SOF behavior in order to avoid costly Al–Al bonds. The observations and conclusions from paper [15] have not been transferred to a general SOF model of clathrates. The results, however, demonstrate that information from first-principles calculations provides an efficient and accurate means to predict and rationalize ordering in these materials.

# Alloy cluster expansions

## 3.1 Introduction

The partition function  $\mathcal{Z}$ , contains all thermodynamic information of a system. To compute  $\mathcal{Z}$  one needs to calculate the potential energy for each possible microstate of the system. For this to be feasible, however, one needs very efficient energy calculations. To this end, the alloy CE technique provides a computationally efficient and accurate way of calculating the energy for different microstates. In the cluster expansion formalism the system being operated on is described by the occupation vector  $\sigma$  where  $\sigma_i$  can, for a binary system, assume a value of either 0 or 1 depending on if an A or B atom is on lattice point  $i$  (Fig. 3.1). Even though the cluster expansion acts on a perfect lattice it can still capture the contribution of relaxations of the atoms by mapping relaxed structures onto the perfect lattice.

The remainder of the chapter is organized as follows:

- The definition of a cluster can be found in section 3.2
- The formal theory of cluster expansions can be found in section 3.3.
- The construction of a cluster expansion and how it can be seen as solving a linear equation system can be found in section 3.4
- In section 3.5 the concept of compressive sensing is introduced. **compressive sensing (CS)** are a class of algorithms that can be used to find the **effective cluster interactions (ECIs)** that describe a CE by solving the linear equation system.

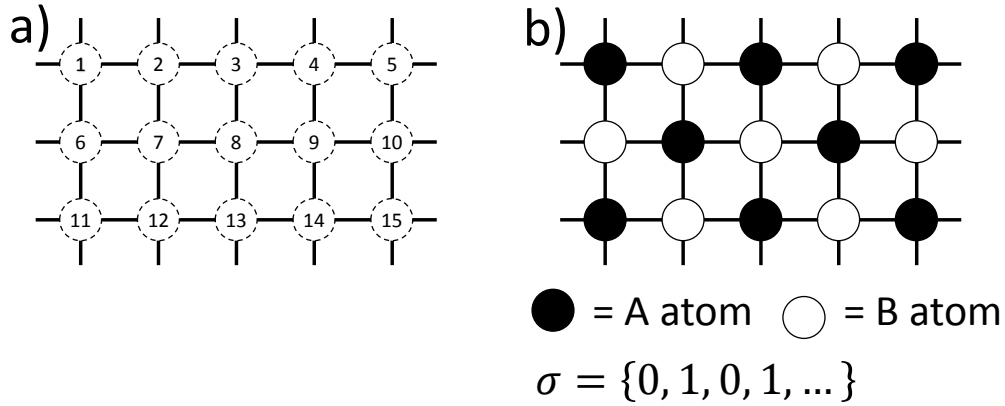


Figure 3.1: a) A fixed lattice with numbered lattice points. b) When the lattice points are occupied by atoms the state of the system can be described by the  $\sigma$  vector where  $\sigma_i$  is the occupation on site  $i$ .

- Cross-validation is introduced in section 3.6. Cross-validation is used both to estimate the error of the obtained ECIs and can also be used to find the best ECIs.
- An example of the procedure for constructing a cluster expansion for a simple binary system can be found in section 3.7

## 3.2 Definition of a cluster

A cluster is defined as a set of lattice points,  $\alpha = \{\sigma_1, \sigma_2, \dots, \sigma_n\}$ . A cluster is thus associated with a cell and possible periodic boundary conditions. The order of a cluster is defined as the number of lattice points in the cluster. A cluster of order 1 is called a singlet and order 2, 3 and 4 are called pair, triplet and quadruplet respectively. The radius, or the size, of the cluster is defined as the average distance of all the lattice points from the geometric center of the cluster. For a given lattice a set of clusters can conveniently be defined as a vector of cutoffs,  $r^{\text{cutoff}}$ . The set of clusters will contain all clusters of order  $i + 2$  with a maximum interatomic distance of less than or equal to  $r_i^{\text{cutoff}}$ . Figure 3.3 shows the clusters with the smallest radius of a **body-centered cubic (bcc)** lattice up to sixth order.

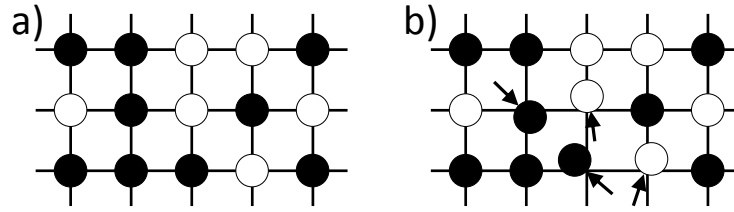


Figure 3.2: Two microstates of the lattice with the same  $\sigma$  vector. a) The atoms sit perfectly on the underlying lattice. b) Some atoms have small displacements away from the ideal positions.

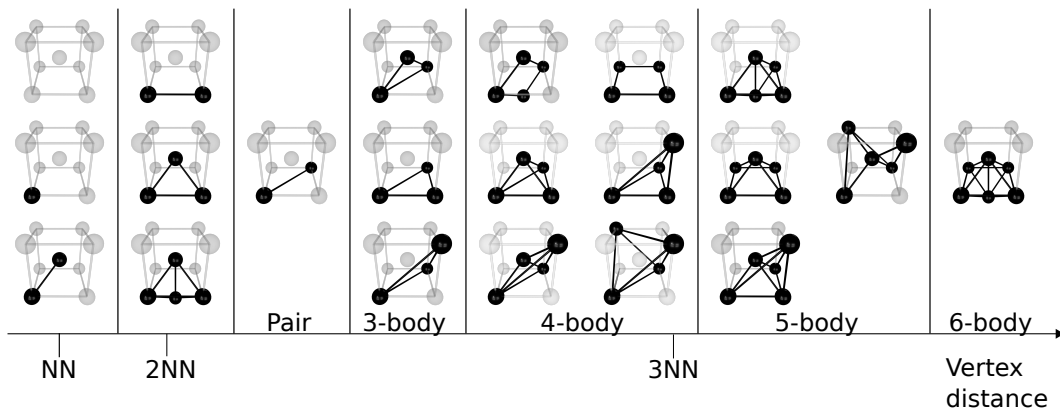


Figure 3.3: Illustration of the smallest clusters up to sixth order in a bcc lattice.

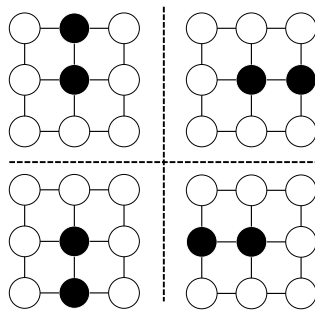


Figure 3.4: Symmetrically equivalent first nearest neighbor pair clusters in a square lattice. These can be found by taking any one of the specific decorations and repeatedly applying a 90 degree rotation until all four equivalent clusters are found.

### 3.3 Formal theory

A CE is able to represent *any* function of the configuration,  $f(\boldsymbol{\sigma})$  if one can construct a complete orthogonal basis of functions with respect to the scalar product [28]

$$\langle f, g \rangle = \frac{1}{M^N} \sum_{\boldsymbol{\sigma}_1, \dots, \boldsymbol{\sigma}_{M^N}} f(\boldsymbol{\sigma})g(\boldsymbol{\sigma}) \quad (3.1)$$

where  $f(\boldsymbol{\sigma})$  and  $g(\boldsymbol{\sigma})$  are two arbitrary functions of the configuration,  $M$  is the allowed number of elements and  $N$  is the number of lattice points in  $\boldsymbol{\sigma}$ .

#### 3.3.1 Point functions

For each lattice point  $p$  we define the  $M$  orthogonal point functions  $\Theta_n(\sigma_p)$

$$\Theta_n(\sigma_p) = \begin{cases} 1 & \text{if } n = 0 \\ -\cos(\pi(n+1)\sigma_p/M) & \text{if } n \text{ is odd} \\ -\sin(\pi n\sigma_p/M) & \text{if } n \text{ is even.} \end{cases} \quad (3.2)$$

It can be verified that these point functions form an orthogonal set over all possible occupation numbers [29],

$$\langle \Theta_n, \Theta_{n'} \rangle = \sum_{\sigma_p=0}^{M-1} \Theta_n(\sigma_p)\Theta_{n'}(\sigma_p) = \begin{cases} 0 & \text{if } n \neq n' \\ \neq 0 & \text{if } n = n'. \end{cases} \quad (3.3)$$

For example, in a three component system ( $M = 3$ ) with  $\sigma_p = \{0, 1, 2\}$  the possible point functions are

$$\Theta_0(\sigma_i) = 1, \quad \Theta_1(\sigma_i) = -\cos 2\pi \frac{\sigma_i}{3}, \quad \Theta_2(\sigma_i) = -\sin 2\pi \frac{\sigma_i}{3}. \quad (3.4)$$

#### 3.3.2 Orthogonal basis

With these point functions an orthogonal set of functions  $\Pi_{\boldsymbol{\alpha}}^{(s)}(\boldsymbol{\sigma})$  in the space of the  $M^N$  configurations on the lattice can be produced by generating the point functions for all possible combinations of  $s$  and lattice points  $\boldsymbol{\alpha}$ . So for a cluster of lattice sites  $\boldsymbol{\alpha} = \{1, 2, \dots, |\boldsymbol{\alpha}|\}$ , and a vector of allowed point function indices,  $s = n_1, n_2, \dots, n_l$  the basis functions are given by,

$$\Pi_{\boldsymbol{\alpha}}^{(s)}(\boldsymbol{\sigma}) = \Theta_{n_1}(\sigma_1)\Theta_{n_2}(\sigma_2)\dots\Theta_{n_l}(\sigma_{\boldsymbol{\alpha}}), \quad (3.5)$$

and it can be verified that these form an orthogonal set[29],

$$\langle \Pi_{\boldsymbol{\alpha}}^{(s)}, \Pi_{\boldsymbol{\beta}}^{(s')} \rangle = \delta_{\boldsymbol{\alpha}\boldsymbol{\beta}}\delta_{ss'}. \quad (3.6)$$

Since the basis functions  $\Pi_\alpha^{(s)}$  form an orthogonal set we can express any function of the configuration as

$$f(\sigma) = \sum_\alpha \sum_s f_{\alpha s} \Pi_\alpha^{(s)}(\sigma). \quad (3.7)$$

Since all basis functions  $\Pi_\alpha^{(s)}$  have one configuration invariant component that is equal to 1 when  $s = \{0, 0, \dots, 0\}$  we can exclude this term from the sum in Eq. (3.7) to obtain

$$f(\sigma) = f_0 + \sum_\alpha \sum_s f_{\alpha s} \Pi_\alpha^{(s)}(\sigma). \quad (3.8)$$

Finally, for practical reasons, we modify Eq. (3.8) by averaging over each distinct cluster and point functions and multiply with the multiplicity and arrive at the final expression for our cluster expansion function

$$f(\sigma) = f_0 + \sum_\alpha \sum_s \langle \Pi_\alpha^{(s)}(\sigma) \rangle_{\alpha'} m_\alpha^{(s)} J_\alpha^{(s)}. \quad (3.9)$$

Here, the summation is carried out over all symmetrically distinct clusters of lattice points. The  $\langle \dots \rangle_{\alpha'}$  function takes the average over the basis functions for all clusters  $\alpha'$  that are symmetry equivalent to  $\alpha$ .  $J_\alpha^{(s)}$  are the ECIs, which determine a specific cluster expansion. Finally,  $m_\alpha^{(s)}$  is the multiplicity of cluster  $\alpha$  for a specific combinations of point functions  $\mathbf{s}$ .

### 3.3.3 Further considerations

As we have seen from the construction of the basis, all combinations of point functions are required for constructing the basis. For a binary system where only the first point function was needed the permutations of these point functions for any cluster order are all equal. For a ternary system both the first and second point functions are needed and thus a pair will have four different combinations of the point functions, i.e. (1, 1), (1, 2), (2, 1) and (2, 2). As will be shown now, not all of these permutations will result in additional parameters in the CE due to symmetry. If our pair cluster  $\alpha = \{\sigma_1, \sigma_2\}$  can be transformed under periodic boundary conditions and the lattice translational and rotational symmetry operations to construct the symmetrically equivalent cluster  $\alpha' = \{\sigma_2, \sigma_1\}$  then the choice of the ordering in  $\alpha = \{\sigma_1, \sigma_2\}$  must produce the same contribution to Eq. (3.9) as choosing  $\alpha = \{\sigma_2, \sigma_1\}$ . Writing out the different choices we have

$$\begin{aligned} \Pi_\alpha^{1,1}(\sigma) &= \Theta_1(\sigma_1)\Theta_1(\sigma_2) \\ \Pi_\alpha^{1,2}(\sigma) &= \Theta_1(\sigma_1)\Theta_2(\sigma_2) \\ \Pi_\alpha^{2,1}(\sigma) &= \Theta_2(\sigma_1)\Theta_1(\sigma_2) \\ \Pi_\alpha^{2,2}(\sigma) &= \Theta_2(\sigma_1)\Theta_2(\sigma_2) \end{aligned} \quad (3.10)$$

and for  $\alpha'$  we get

$$\begin{aligned}
 \Pi_{\alpha'}^{1,1}(\sigma) &= \Theta_1(\sigma_2)\Theta_1(\sigma_1) \\
 \Pi_{\alpha'}^{1,2}(\sigma) &= \Theta_1(\sigma_2)\Theta_2(\sigma_1) \\
 \Pi_{\alpha'}^{2,1}(\sigma) &= \Theta_2(\sigma_2)\Theta_1(\sigma_1) \\
 \Pi_{\alpha'}^{2,2}(\sigma) &= \Theta_2(\sigma_2)\Theta_2(\sigma_1).
 \end{aligned} \tag{3.11}$$

The point functions basis functions (1, 1) and (2, 2) are thus symmetric in terms of permuting the lattice points. For (1, 2) and (2, 1) there is, however, an asymmetry and the choice of the order in the cluster  $\alpha$  will matter for the end result in Eq. (3.9). The choice of ordering the lattice points in a cluster is completely arbitrary and should not matter to the final result of the cluster expansion. To circumvent the choice of ordering of lattice points in a cluster one instead only use the point functions (1, 1), (1, 2) and (2, 2) for this cluster. Additionally, for the cluster basis (1, 2) one uses both possibilities of ordering the pair. The final basis functions for cluster  $\alpha$  then become the following

$$\begin{aligned}
 \Pi_{\alpha}^{1,1}(\sigma) &= \Theta_1(\sigma_1)\Theta_1(\sigma_2) \\
 \Pi_{\alpha}^{1,2}(\sigma) &= \Theta_1(\sigma_1)\Theta_2(\sigma_2) + \Theta_1(\sigma_2)\Theta_2(\sigma_1), \\
 \Pi_{\alpha}^{2,2}(\sigma) &= \Theta_2(\sigma_1)\Theta_2(\sigma_2)
 \end{aligned} \tag{3.12}$$

where it is apparent that the choice of the order in the cluster has no effect on its representation in the cluster space. Note that in Eq. (3.9) the multiplicity  $m_{\alpha}^{(1,2)}$  will be twice as large as the other multiplicities.

### 3.3.4 Symmetrically indistinct clusters

This section describes the identification of equivalent clusters by using symmetry operations. For the  $n$ -body cluster  $\alpha = \{\sigma_0, \sigma_1, \dots, \sigma_{n-1}\}$  the symmetrically equivalent clusters are found by converting the lattice points into fractional positions  $\alpha = \{\mathbf{r}_0, \mathbf{r}_1, \dots, \mathbf{r}_{n-1}\}$ . A symmetry operation  $\hat{\mathbf{s}}$  consists of a linear transformation by a  $3 \times 3$  matrix,  $\bar{\gamma}$  and a translation  $\boldsymbol{\tau}$

$$\mathbf{r}' = \hat{\mathbf{s}}\mathbf{r} = \bar{\gamma}\mathbf{r} + \boldsymbol{\tau}. \tag{3.13}$$

A lattice typically have a number of associated symmetry operations  $\mathbf{S} = \hat{\mathbf{s}}_0, \hat{\mathbf{s}}_1, \dots, \hat{\mathbf{s}}_{m-1}$ . These symmetry operations can then be used to produce  $m$  symmetrically indistinct clusters where the cluster  $i$  is given by

$$\alpha_i = \{\hat{\mathbf{s}}_i\mathbf{r}_0, \hat{\mathbf{s}}_i\mathbf{r}_1, \dots, \hat{\mathbf{s}}_i\mathbf{r}_{n-1}\}. \tag{3.14}$$

Additionally, depending on the periodic boundary conditions, one can also translate all positions in a cluster with multiples of the unit cell vectors. Figure 3.4 illustrates the set of equivalent clusters for the nearest neighbor pair.

### 3.4 Construction of a cluster expansion

Equation (3.9) can represent any function of the configuration  $f(\boldsymbol{\sigma})$ . The task remaining in the construction of a cluster expansion is to find the **ECIs**. To this end, one requires reference data in the form of a set of configurations  $\{\boldsymbol{\sigma}_1, \boldsymbol{\sigma}_2, \dots, \boldsymbol{\sigma}_n\}$  as well as target data  $\{E_1, E_2, \dots, E_n\}$ . The sums in Eq. (3.9) can be replaced with a dot product

$$f(\boldsymbol{\sigma}) = f_0 + \sum_{\alpha} \sum_s \langle \Pi_{\alpha}^{(s)}(\boldsymbol{\sigma}) \rangle_{\alpha'} m_{\alpha}^{(s)} J_{\alpha}^{(s)} = \boldsymbol{\omega}(\boldsymbol{\sigma}) \cdot \boldsymbol{J}, \quad (3.15)$$

where

$$\boldsymbol{\omega}(\boldsymbol{\sigma}) = \left\{ 1, \langle \Pi_{\alpha_1}^{(s_{\alpha_1})}(\boldsymbol{\sigma}) \rangle_{\alpha'_1} m_{\alpha_1}^{(s_{\alpha_1})}, \dots, \langle \Pi_{\alpha_1}^{(s'_{\alpha_1})}(\boldsymbol{\sigma}) \rangle_{\alpha'_1} m_{\alpha_1}^{(s'_{\alpha_1})}, \dots, \langle \Pi_{\alpha_n}^{(s_{\alpha_n})}(\boldsymbol{\sigma}) \rangle_{\alpha'_n} m_{\alpha_n}^{(s_{\alpha_n})} \right\},$$

and  $\boldsymbol{J}$  denotes the vector of **ECIs** where  $J_0 = f_0$ . The vector  $\boldsymbol{\omega}(\boldsymbol{\sigma})$  is commonly called cluster vector. Note that it can sometimes be useful to exclude  $m_{\alpha}^{(s)}$  from  $\boldsymbol{\omega}$  and let the target values  $E_i$  refer to the primitive unit cell. This will ensure all elements in  $\boldsymbol{\omega}$  are in the interval  $[-1, 1]$  and avoid a bias due to the number of elements in  $\boldsymbol{\sigma}$ . Now we can cast the problem of finding the **ECIs** in the form of a linear equation

$$\begin{bmatrix} \boldsymbol{\omega}(\boldsymbol{\sigma}_1) \\ \boldsymbol{\omega}(\boldsymbol{\sigma}_2) \\ \vdots \\ \boldsymbol{\omega}(\boldsymbol{\sigma}_n) \end{bmatrix} \begin{bmatrix} J_{\alpha_1}^{(s)} \\ J_{\alpha_2}^{(s)} \\ \vdots \\ J_{\alpha_n}^{(s)} \end{bmatrix} = \begin{bmatrix} E_1 \\ E_2 \\ \vdots \\ E_n \end{bmatrix} \quad (3.16)$$

The effective cluster interactions, i.e the  $J_{\alpha}^{(s)}$  of each cluster  $\alpha$ , are unknown and since the number of clusters is in principle infinite there is an infinite number of unknown parameters to determine. Based on physical intuition we, however, expect that physical interactions are short-ranged and few-bodied. Therefore, if we construct our basis functions starting from singlets and geometrically small pairs, triplets etc. the **CE** is expected to converge quickly to yield an acceptable tolerance and the number of unknown parameters remains manageable.

There have also been advances in the algorithms that solve Eq. (3.16). These **CS** algorithms can find the **ECIs** even if the problem is severely under-determined, i.e. the number of unknowns are much larger than the number of available data points. The choice of when to truncate is thus not so important which effectively removes much of the ‘‘human factor’’ when it comes to constructing a cluster expansion. Solving under determined problems and how to do validation is discussed in the following sections.

### 3.5 Compressive sensing

One way to solve Eq. (3.16) when the problem is underdetermined is by taking advantage of CS algorithms. The CS technique provides a simple and efficient way to extract the important ECIs and compute their values in one shot [30, 31, 32]. To demonstrate CS it helps to first define the  $l_p$  norm of a vector  $u$

$$\|u\|_p = \left( \sum_i |u_i|^p \right)^{1/p}. \quad (3.17)$$

In the CS method the problem is solved by searching for the solution with the smallest  $l_1$  norm while still reproducing the results with a given accuracy

$$J_{\text{CS}} = \arg \min_J \left\{ \|J\|_1 : \|\bar{\Pi}J - E\|_2 < \epsilon \right\}. \quad (3.18)$$

Where, in the case of cluster expansions,  $\bar{\Pi}$  is the matrix of cluster vectors,  $J$  is the ECIs and  $E$  is the target properties. The form in Eq. (3.18) is inconvenient to work with and it is common practice to work with an unconstrained approach that minimizes the  $l_1$  norm and the least squares sum of the fitting error

$$J = \arg \min_J \left\{ \mu \|J\|_1 + \frac{1}{2} \|E - \bar{\Pi}J\|^2 \right\}, \quad (3.19)$$

where the parameter  $\mu$  controls the accuracy of the fit. A high value of  $\mu$  leads to sparse solution but larger prediction error and vice versa. It is, however, difficult to efficiently implement mixed  $l_1$  and  $l_2$  minimization problems such as Eq.(3.19).

#### 3.5.1 Split Bregman algorithm

Goldstein and Osher proposed the split Bregman algorithm which eliminates this problem [33]. The split Bregman iteration splits the  $l_1$  norm of the solution from the objective function and replaces it with a variable  $d$  which then converges towards the  $l_1$  term  $\lim_{k \rightarrow \infty} (d - \mu J) = \mathbf{0}$ , where  $k$  is the number of split Bregman iterations. To this end a least-squares  $l_2$  term is added to the objective function to ensure that  $d = \mu J$

$$J = \arg \min_{J,d} \left\{ \|d\|_1 + \frac{1}{2} \|\bar{\Pi}J - E\|^2 + \frac{\lambda}{2} \|d - \mu J\|^2 \right\}. \quad (3.20)$$

This formulation is advantageous because the minimization involving the quadratic form  $\frac{1}{2} \|\bar{\Pi}J - E\|^2$  does not involve any  $l_1$  terms and can be minimized efficiently using efficient  $l_2$  minimization algorithms. The split Bregman algorithm comprises the following steps

$$J^{k+1} = \arg \min_J \left\{ \frac{1}{2} \|\bar{\Pi}J - E\|^2 + \frac{\lambda}{2} \|d^k - \mu J - b^k\|^2 \right\} \quad (3.21)$$

$$\mathbf{d}^{k+1} = \arg \min_{\mathbf{d}} \left\{ \|\mathbf{d}\|_1 + \frac{\lambda}{2} \|\mathbf{d} - \mu \mathbf{J}^{k+1} - \mathbf{b}^k\|^2 \right\} \quad (3.22)$$

$$\mathbf{b}^{k+1} = \mathbf{b}^k + \mu \mathbf{J}^{k+1} - \mathbf{d}^{k+1} \quad (3.23)$$

Where in Eq.(3.23) the residual after iteration  $k$  is added back to the residual vector  $\mathbf{b}^{k+1}$  for the next iteration in style with a Bregman iteration which result in a quicker convergence [34]. Starting from  $\mathbf{d}^0 = 0$ ,  $\mathbf{b}^0 = 0$  and  $\mathbf{J}^0 = 0$ . First, the  $l_2$  minimization in Eq.(3.21) is solved, the second step, Eq.(3.22) separates into individual vector components and is solved by shrinkage,

$$\mathbf{d}_n^{k+1} = \text{shrink}(\mu \mathbf{J}_n^{k+1} + \mathbf{b}_n^k, 1/\lambda) \quad (3.24)$$

which is defined by

$$\text{shrink}(y, \alpha) \equiv \text{sign}(y) \max(|y| - \alpha, 0) \quad (3.25)$$

Shrinkage decreases the absolute magnitude of the  $y$  vector by  $\alpha$  and sets it to zero if  $y \leq \alpha$ . This procedure is then usually repeated until the  $\mathbf{J}$  vector has converged within a target tolerance.

## 3.6 Cross-validation

When training a model such as a CE one requires a set of data points that can be used to train and test the obtained model. Commonly the data points is split up in a training set and a test set. The training set is the data points used as input to optimization algorithms that solve problems similar to equation (3.18). A training set has an associated training error defined as  $\|\bar{\Pi} \mathbf{J} - \mathbf{E}\|_2$  where  $\mathbf{J}$  is the parameters obtained from training with the training set,  $\mathbf{E}$  and  $\bar{\Pi}$  is the target property and the description matrix for the training set respectively. The test set is data points which were not used in the training set. The test error is the  $l_2$  norm of the prediction error of the test set. The usefulness of these different sets and errors come in when trying to find a good model. For example, if for a particular value of  $\mu$ , the training error is zero but the test error is high, the trained model is excellent at predicting already seen data but are unable to predict new and unseen data. This is called overfitting and must be avoided. Another type of overfitting is when one instead find values of  $\mu$  that finds the minimum test error. Even though the test set is not part of the training set, information about the training set still seeps into the training procedure since the parameters obtained in the training are optimal for the specific test set. **Cross-validation (CV)** is a way to overcome both these types of overfitting both when estimating the error and when finding a model. In CV the training and tests sets do not remain fixed which reduces the risk of overfitting to a specific training or testing set. The use of CV scores is widely accepted as the quantity for determining the accuracy of the CE.

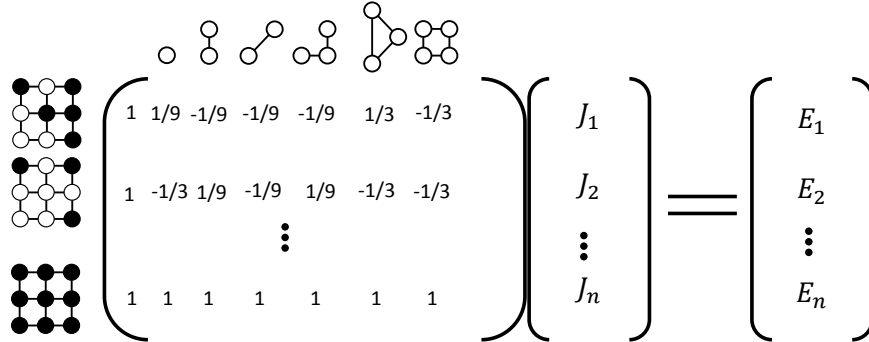


Figure 3.5: Cluster expansions can be constructed by solving a set of linear equation systems.

### 3.6.1 Leave-one-out cross validation

One type of cross validation is the [leave-one-out CV \(LOO-CV\)](#), which is defined as

$$(\text{CV})^2 = \frac{1}{N} \sum_{n=1}^N (\hat{E}_{(n)} - E_n)^2, \quad (3.26)$$

where  $E_n$  is the calculated energy for structure  $n$  and  $\hat{E}_{(n)}$  is the predicted value of the energy of structure  $n$  as calculated with the CE fit with the  $(N - 1)$  other structures. This method requires making  $N$  cluster expansions so it can be computationally expensive. When the training curve is steep and the number of available structures are few the LOO-CV can be a good estimator compared to other estimators which splits the available structures more and hence over estimate the error.

### 3.6.2 k-fold cross validation

Another commonly used estimator for the error are k-folds cross validations. Here, the data is randomly divided up into  $k$  evenly sized subsets. One of the  $k$  subsets will be left out for validation and the remaining  $k-1$  subsets will be used for training. This is repeated for all  $k$  subsets and the final cross validation score is the average validation for the  $k$  validation scores. Note that  $k$ -fold validation reduces to [LOO-CV](#) when  $k$  is the number of available data points.

### 3.7 Cluster expansion for a binary system

To demonstrate the formalism developed in this chapter we will now explicitly describe the construction of a CE for simple binary system. In a binary system only one point function will be used in the cluster functions,  $\Theta_1(\sigma_p) = -\cos(\pi\sigma_p)$ . Only two occupation numbers are needed as well, 0 and 1, which have a corresponding point function value of  $-1$  and  $+1$  respectively. Hence a binary cluster expansions share a lot of similarities with the Ising model. Next, make the choice that white and black atoms are to be indicated by occupation 0 and 1 respectively. The average over symmetrically distinct clusters  $\alpha'$  in equation (3.9) will for the singlet cluster be

$$\langle \Pi_{\alpha=\text{singlet}}(\boldsymbol{\sigma}) \rangle_{\alpha'} = \frac{N_{\boldsymbol{\sigma}_{\alpha'}=(1)} - N_{\boldsymbol{\sigma}_{\alpha'}=(0)}}{N_{\boldsymbol{\sigma}_{\alpha'}=(0\|1)}}. \quad (3.27)$$

For a pair the averages will become

$$\langle \Pi_{\alpha=\text{pair}}(\boldsymbol{\sigma}) \rangle_{\alpha'} = \frac{N_{\boldsymbol{\sigma}_{\alpha'}=(0,0)} + N_{\boldsymbol{\sigma}_{\alpha'}=(1,1)} - N_{\boldsymbol{\sigma}_{\alpha'}=(0,1)}}{N_{\boldsymbol{\sigma}_{\alpha'}=(0,0\|0,1\|1,1)}}, \quad (3.28)$$

where  $N_{\boldsymbol{\sigma}_{\alpha'}=(i,j)}$  is the number of equivalent clusters that have occupation  $(i,j)$  or  $(j,i)$ . To calculate values such as  $N_{\alpha'=(0,0)}$  a summation is done over all index pairs  $(i,j)$  that are symmetrically equivalent. Hence, the construction of the cluster vector,  $\boldsymbol{\omega}(\boldsymbol{\sigma})$ , is obtained by summation and averaging of the cluster functions. All the  $\boldsymbol{\alpha}$  can be precomputed so a summation can be performed very efficiently with a computer program. Then all available configurations can be mapped to cluster vectors,  $\boldsymbol{\omega}$ , which can constitute different training and test sets (Fig. 3.5) as described in the previous sections. Once a suitable value for the fitting parameter  $\mu$  have been found, by using various cross validation techniques, the final set of ECIs,  $\mathbf{J}_{\text{final}}$ , can be obtained. The construction of the cluster expansion is now complete and the expanded property can for a configuration  $\boldsymbol{\sigma}$  be computed very efficiently with  $\boldsymbol{\omega}(\boldsymbol{\sigma})\mathbf{J}_{\text{final}}$ .



# Monte Carlo simulations

## 4.1 Monte Carlo integration

Monte Carlo (MC) methods represent a broad class of computer algorithms that are based on the use of random numbers to sample high-dimensional functions. MC integration is one example of such a technique where the average value of an integral

$$I = \int_0^1 dx f(x) = \langle f(x) \rangle \quad (4.1)$$

can be approximated by evaluating  $f(x)$  at  $N$  points  $x_i$  chosen at random with uniform probability over the interval  $[0, 1]$ . The mean value becomes

$$I_N = \langle f \rangle = \frac{1}{N} \sum_{i=1}^N f(x_i) = \frac{1}{N} \sum_{i=1}^N f_i, \quad (4.2)$$

and the variance

$$\sigma_f^2 = \langle f^2 \rangle - \langle f \rangle^2. \quad (4.3)$$

Such that the integral is approximated by

$$I = I_N \pm \frac{\sigma_f}{\sqrt{N}}. \quad (4.4)$$

By increasing the number of points  $N$  the error of the approximation becomes smaller and as  $N \rightarrow \infty$  one approaches the correct value of  $I$ .

## 4.2 Importance sampling

An alternative approach to decreasing the error is to choose the points  $x_i$  based on the magnitude of  $f(x)$ . Consider a probability density function  $p(x) > 0$  that is positive and normalized to 1 on  $[0, 1]$ . We can rewrite equation (4.1) to obtain

$$I = \int_0^1 dx f(x) = \int_0^1 dx \frac{f(x)}{p(x)} p(x) = \int_0^1 dx g(x) = \langle g(x) \rangle_p, \quad (4.5)$$

where  $g(x) = f(x)/p(x)$  and the notation  $\langle \dots \rangle_p$  signifies that the average is obtained from sampling values of  $x$  according to  $p(x)$ . The mean value of the integral can then be written as

$$I_N = \langle f \rangle = \frac{1}{N} \sum_{i=1}^N g_i \quad (4.6)$$

and  $I$  can be approximated with

$$I = I_N \pm \frac{\sigma_g}{\sqrt{N}}. \quad (4.7)$$

Assume now that  $p(x)$  follows the approximate behavior of  $f(x)$ , i.e.  $p(x)$  has high probability density when  $|f(x)|$  is large and vice versa. Then  $g(x)$  will become a smoother function than  $f(x)$  and  $\sigma_g < \sigma_f$ . This approach of choosing values of  $x$  where  $|f(x)|$  is large is called importance sampling.

## 4.3 Thermodynamic integration on the lattice

Now, instead of approximating a one-dimensional integral let us consider a binary atomic lattice  $\sigma$  at a certain temperature  $T$  and find the average of some quantity  $A$  that depends on the configuration. Let the atomic lattice vector  $\sigma$  have dimensionality  $N$ , where  $N$  is the number of lattice points and the elements of the vector can assume values of either 0 or 1. The average value is then

$$\langle A \rangle = \frac{1}{M^N} \sum_{\text{all possible } \sigma} A(\sigma) P(\sigma). \quad (4.8)$$

The probability of finding the system at  $\sigma$  is  $P(\sigma)$ , which is defined as

$$P(\sigma) = \frac{\exp(-U(\sigma)/k_B T)}{\sum_{\text{all possible } \sigma'} \exp(-U(\sigma')/k_B T)}, \quad (4.9)$$

where  $U(\sigma)$  is the internal energy of the configuration and  $k_B$  is the Boltzmann constant. Carrying out the sum in equation (4.8) is unfortunately impossible to

carry out exactly. For illustration, consider that for a system with 100 sites the number of possible configurations, ignoring symmetry, is  $2^{100} \approx 10^{30}$ . Also assume that each evaluation of  $A(\boldsymbol{\sigma})$  requires only one floating point operation (FLOP). The time to calculate the sum by using the largest computer cluster available<sup>1</sup> would still require around  $10^6$  times longer than the age of the universe. This demonstrates the necessity to find efficient methods to solve to Eq. (4.8).

## 4.4 The Metropolis algorithm

A naive approach to approximate Eq. (4.8) using a MC approach is to generate a large number of different configurations,  $\boldsymbol{\sigma}$ , where each element is randomly assigned a value of either 0 or 1, and estimating the average. This approach would, however, lead to very slow convergence due the probability function  $P(\boldsymbol{\sigma})$  commonly being a very sharp function, which would lead to  $P(\boldsymbol{\sigma})$  being close to zero for most choices of  $\boldsymbol{\sigma}$ . A more prudent approach would be to try to apply the importance sampling approach introduced earlier. A direct implementation of importance sampling is difficult, however, since it is not obvious how to efficiently generate configurations  $\boldsymbol{\sigma}$  according to a suitable probability. Instead, an efficient way to generate configurations is to implement a so-called Markov chain, where each new configuration generated is based on a probability ratio that depends on the previous configuration.

The first adaptation of such a approach was introduced in 1953 by Metropolis *et al.* to determine the equation of state for a hard sphere liquid [35]. It is based on the understanding that thermodynamic averaging only requires knowledge of relative rather than absolute probabilities such as in Eq. (4.8). It uses a Markov chain to generate configurations that are more important by rejecting configurations that are unlikely, similar to importance sampling.

### 4.4.1 Markov chain Monte Carlo

A Markov chain is a stochastic process, in which a system undergoes transitions from one state to another. The Markov process is characterized by a lack of memory of where it has been. The future of the chain depends solely on the current state. The transition probability is given by a transition matrix

$$T(X \rightarrow X') \equiv T_{XX'}, \quad (4.10)$$

for a transition from state  $X$  to state  $X'$ . The transition probability has to satisfy

$$0 \leq T_{XX'} \leq 1 \quad (4.11)$$

---

<sup>1</sup>The Sunway TaihuLight in China is currently the largest non-distributed computer cluster with a peak performance at about 125 PFLOPS.

and the probability has to be normalized

$$\sum_{X'} T_{XX'} = 1. \quad (4.12)$$

The task is to generate a Markov chain of configurations such that they have a distribution proportional to the Boltzmann factor and this distribution should be independent on the position of the chain and of the initial configuration. The Markov chain can exhibit these properties under certain conditions, at least for a sufficiently long time so that the configuration can loose memory of its initial state. These conditions are:

- The Markov chain needs to be irreducible, that is every configuration included in the ensemble should be accessible from every other configuration within a finite number of steps.
- There should be no periodicity. Periodicity means that it is not possible to revisit a configuration except after  $t = nk$  steps,  $n = 1, 2, 3 \dots$ , where  $k$  is fixed.

A Markov chain that satisfies these conditions is called ergodic. If the Markov chain is ergodic it converges to a unique stationary distribution. The transition probability needs to be chosen such that the stationary distribution is the desired distribution. To assure this, consider the stationary distribution  $\rho(X)$ ; one can also introduce a new function  $\rho(X, t)$ , which gives the probability of finding configuration  $X$  after  $t$  Markov steps, which for an ergodic chain becomes independent of  $t$  if  $t$  is large. This function can change from one step to another by

- going from  $X$  at step  $t$  to  $X'$  at  $t + 1$  leading to a decrease in  $\rho(X)$
- going from  $X'$  at step  $t$  to  $X$  at  $t + 1$  leading to an increase in  $\rho(X)$

that can be summarized with

$$\rho(X, t+1) - \rho(X, t) = - \sum_{X'} T(X \rightarrow X') \rho(X, t) + \sum_{X'} T(X' \rightarrow X) \rho(X', t). \quad (4.13)$$

This equation is called the master equation. The stationary solution of this equation is found by requiring  $\rho(X, t + 1) = \rho(X, t)$  so we have

$$\sum_{X'} T(X \rightarrow X') \rho(X, t) = \sum_{X'} T(X' \rightarrow X) \rho(X', t). \quad (4.14)$$

Leaving out the  $t$ -dependence, which is allowed due to the “memory loss” of a Markov chain, yields

$$T(X \rightarrow X') \rho(X) = T(X' \rightarrow X) \rho(X'), \quad (4.15)$$

which is known as the condition of detailed balance. This means that in equilibrium the average number of steps that results in the system leaving state  $X$  must be exactly equal to the number of steps from all other states  $X'$  to  $X$ . This means that  $\rho(X)$  and  $\rho(X')$  do not change. Since this is true for all pairs of  $X$  and  $X'$  the probability distributions will remain stationary. Reformulating the detailed balance condition with the transition probability in this form yields

$$T(X \rightarrow X') = \omega_{XX'} A_{XX'}, \quad (4.16)$$

where  $\omega_{XX'}$  is the probability for going from state  $X$  to state  $X'$  and is symmetric  $\omega_{XX'} = \omega_{X'X}$ .  $A_{XX'}$ , which must lie between 0 and 1, is the acceptance probability for actually committing the change. The detailed balance condition can then be expressed as

$$\frac{A_{XX'}}{A_{X'X}} = \frac{\rho(X')}{\rho(X)}. \quad (4.17)$$

If the sought after distribution is the Boltzmann distribution,  $\rho(X) = \exp -\beta U(X)$ , there are a number of choices for the acceptance probability  $A_{XX'}$  that will accomplish this. The choice of Metropolis *et al.* was

$$\begin{cases} A_{XX'} = \exp \beta [U(X') - U(X)] & \text{if } \rho(X') < \rho(X) \\ A_{XX'} = 1 & \text{if } \rho(X') \geq \rho(X). \end{cases} \quad (4.18)$$

The Metropolis algorithm can now be formulated as follows:

- Starting from a state  $X$ , make a small trial move into a new state  $X'$  with a probability of  $\omega_{XX'}$ .
- Compare the weights of the distribution for the different states  $\rho(X)$  and  $\rho(X')$ .  $A_{XX'}$ , the acceptance probability, is chosen equal to 1 if  $\rho(X') > \rho(X)$  else it is chosen to be equal to  $\rho(X')/\rho(X)$ .
- The new state  $X'$  is accepted with probability  $A_{XX'}$  (the system moves from  $X$  to  $X'$ ) and is rejected with probability  $1 - A_{XX'}$  (the system remains in state  $X$ ). To decide if a state is accepted or not a random number is generated uniformly in the range  $[0, 1]$  and compared to the acceptance probability. If the random number is larger than the acceptance probability the trial move is accepted.

Since each trial move is only a small change in the configuration there is an inherent correlation between the states  $X$  and  $X'$ . There is thus a correlation length  $s$  for the Markov chain and it is necessary to carry out  $s$  trial steps before reaching a new uncorrelated configuration. One MC step (or cycle) is defined as  $N$  trial steps, where  $N$  is the number of particles which is commonly used to approximate  $s$ . There is also a need to equilibrate the initial configuration meaning that it is necessary to run the Metropolis algorithm before the actual sampling commences.

## 4.5 Probability of a state

The sampling procedure described in the previous section requires the probability ratio of two microstates. Let us consider again the rigid binary lattice introduced above. Each possible combination of zeros and ones on the  $\sigma$  vector describes a microstate of the system. Consider the case where this system is in thermal contact with a heat reservoir with constant temperature and an infinitely large heat capacity, i.e. we can add and remove as much energy as necessary without affecting the temperature of the reservoir. Since the composition of the system might change there can also be an exchange of atoms between system and reservoir.

For an isolated system, all possible microstates are equally probable. The system of  $N$  sites considered here is, however, not isolated since it is in contact with a heat reservoir. Rather the *joint* system and the heat reservoir form an isolated system. The joint microstates of system and heat reservoir will therefore be equally probable.

Consider two microstates  $s_1$  and  $s_2$  with a corresponding number of accessible states  $\Omega_R(s_1)$  and  $\Omega_R(s_2)$  for each respective reservoir. At this point there is no way of telling what the actual probabilities of the different states are since the number of accessible states associated with the heat reservoirs is unknown. All we know at this point is that the probability of a state is proportional to the total number of accessible microstates, i.e.  $P(s_1) \propto \Omega_R(s_1)$ . Consider now the ratio of probabilities

$$\frac{P(s_1)}{P(s_2)} = \frac{\Omega_R(s_1)}{\Omega_R(s_2)}. \quad (4.19)$$

Rewriting this equation by using the definition of entropy  $S = k_B \ln \Omega$  one obtains

$$\frac{P(s_1)}{P(s_2)} = \frac{e^{S_R(s_1)/k_B}}{e^{S_R(s_2)/k_B}} = e^{[S_R(s_1) - S_R(s_2)]/k_B}. \quad (4.20)$$

Now the ratio of probabilities depends on the change of entropy in the reservoir when going from state  $s_1$  to state  $s_2$ . The change in the entropy of the reservoirs should be small since the system is small compared to the reservoir. Then we can use the thermodynamic identity

$$dS = \frac{1}{T} (dU + PdV - \mu dN). \quad (4.21)$$

Since all ensembles discussed in this thesis have constant volume  $V$  and fixed number of total atoms (or sites)  $N$ , the expression can be simplified to  $dS = S(s_2) - S(s_1) = \frac{1}{T} (dU - \Delta\mu \Delta N_A) = - (E(s_2) - E(s_1) - \Delta\mu(N_A(s_2) - N_A(s_1)))$ , where  $E$  is the internal energy of the system,  $N_A(s_2)$  and  $N_A(s_1)$  are the numbers of  $A$  atoms in system  $s_2$  and  $s_1$ , respectively, and  $\Delta\mu$  is the chemical potential difference

between species  $A$  and  $B$

$$\frac{P(s_1)}{P(s_2)} = e^{(E(s_2)-E(s_1)-\Delta\mu\Delta N_A)/k_B T}. \quad (4.22)$$

As was shown in section 4.5 this ratio of probabilities is all that is needed to carry out a Metropolis MC simulation.

For the sake of completeness, however, let us determine the actual probability of the microstate. First we separate all terms in Eq. (4.22) related to  $s_1$  to one side and terms related to  $s_2$  to the other side,

$$P(s_1)e^{(E(s_1)-\Delta\mu N_A(s_1))/k_B T} = P(s_2)e^{(E(s_2)-\Delta\mu N_A(s_2))/k_B T}. \quad (4.23)$$

The right hand side does not depend on state  $s_1$  and vice versa and must therefore be equal to a constant

$$P(s_1)e^{(E(s_1)-\Delta\mu N_A(s_1))/k_B T} = A \quad (4.24)$$

and the probability becomes

$$P(s_1) = Ae^{-(E(s_1)+\Delta\mu N_A(s_1))/k_B T}. \quad (4.25)$$

Furthermore, the probabilities of all states must sum up to 1

$$\sum_{s_i} P(s_i) = A \sum_{s_i} e^{-(E(s_i)+\Delta\mu N_A(s_i))/k_B T} = 1, \quad (4.26)$$

which leads to

$$A = \frac{1}{\sum_{s_i} e^{-(E(s_i)+\Delta\mu N_A(s_i))/k_B T}}. \quad (4.27)$$

Thus we see that the normalization constant  $A$  is equal to  $1/\mathcal{Z}$  where  $\mathcal{Z}$  is the partition function and the probability of state  $s_1$  becomes

$$P(s_1) = \frac{e^{-(E(s_1)+\Delta\mu N_A(s_1))/k_B T}}{\mathcal{Z}} = \frac{e^{-(E(s_1)+\Delta\mu N_A(s_1))/k_B T}}{\sum_{s_i} e^{-(E(s_i)+\Delta\mu N_A(s_i))/k_B T}}. \quad (4.28)$$

## 4.6 The canonical ensemble

In the canonical ensemble the volume  $V$ , the temperature,  $T$ , and the number of atoms for each species  $N_i$  are fixed. Equation (4.28) is then simplified so that the probability of a state only depends on its energy,

$$P_{\text{canonical}}(s_1) = \frac{e^{-E(s_1)/k_B T}}{\sum_{s_i} e^{-E(s_i)/k_B T}}. \quad (4.29)$$

The probability ratio used in the MC simulation becomes

$$\frac{P_{\text{canonical}}(s_1)}{P_{\text{canonical}}(s_2)} = e^{(E(s_2)-E(s_1))/k_B T}. \quad (4.30)$$

Since the number of atoms of each kind is kept fixed the only configurations being explored in the MC simulations correspond to a re-ordering of atoms from the initial configuration. Therefore in lattice based models trial steps consist of swapping the species between two sites.

## 4.7 Semi-grand canonical ensemble

In the semi-grand canonical (SGC) ensemble the volume  $V$ , the temperature  $T$ , the chemical potential difference(s)  $\Delta\mu_i$  and the number of sites  $N$  are fixed but the composition is allowed to change. Equation (4.28) is then kept as is and the probability of a state becomes (for a binary system)

$$P_{\text{SGC}}(s_1) = \frac{e^{-(E(s_1)+\Delta\mu N_A(s_1))/k_B T}}{\sum_{s_i} e^{-(E(s_i)+\Delta\mu N_A(s_i))/k_B T}}. \quad (4.31)$$

The probability ratio used in the MC simulation becomes

$$\frac{P_{\text{SGC}}(s_1)}{P_{\text{SGC}}(s_2)} = e^{(E(s_2)-E(s_1)-\Delta\mu\Delta N_A)/k_B T}, \quad (4.32)$$

In the SGC ensemble the concentrations (yet not the total number of sites) are allowed to change. Therefore the trial step consists of selecting a site and changing its occupation to another species.

## 4.8 Validity of lattice based models

The partition function that has been discussed in this chapter only considers the summation over occupations  $\sigma$ . The CE technique namely only considers the occupation vector and not displacements of the atoms. For real materials, however, the atoms also undergo vibrations around their equilibrium positions. This displacive degree of freedom is thus neglected in the CE, yet it can play a role in the actual value of a thermodynamical average. This might raise concerns about the validity of the calculated thermodynamical averages using CEs to represent the Hamiltonian in MC simulations. This section therefore considers the approximations made when using a CE in MC simulations for calculating thermodynamical averages.

In the canonical ensemble (Sect. 4.6) the partition function is defined as

$$\mathcal{Z}(N, V, T) = \sum_{\text{all states } j} \exp[-\beta E_j(N, V, T)]. \quad (4.33)$$

The partition function involves a sum over all microstates  $j$  of the system, each of which can be split up into one part consisting of the ordering of the atoms on a lattice and one part consisting of all possible displacements of the atoms for that specific ordering

$$\mathcal{Z}(N, V, T) = \sum_{\{\boldsymbol{\sigma}\}} \sum_{\{\nu \in \boldsymbol{\sigma}\}} \exp[-\beta E(\boldsymbol{\sigma}, \nu, N, V, T)], \quad (4.34)$$

where  $\{\boldsymbol{\sigma}\}$  is the set of all possible  $\boldsymbol{\sigma}$  with constant  $N$  and  $\{\nu \in \boldsymbol{\sigma}\}$  is the set of all displacements of the atoms which project on  $\boldsymbol{\sigma}$ . Thus  $\{\nu \in \boldsymbol{\sigma}\}$  represents a subspace of the phase space of the original ensemble. The partition function can then be written as

$$\mathcal{Z}(N, V, T) = \sum_{\{\boldsymbol{\sigma}\}} \Lambda(\boldsymbol{\sigma}, N, V, T), \quad (4.35)$$

with

$$\Lambda(\boldsymbol{\sigma}, N, V, T) = \sum_{\{\nu \in \boldsymbol{\sigma}\}} \exp[-\beta E(\boldsymbol{\sigma}, \nu, N, V, T)]. \quad (4.36)$$

In other words  $\Lambda(\boldsymbol{\sigma}, N, V, T)$  is the partition function for the subspace of the full ensemble for which all microstates project to the same configuration  $\boldsymbol{\sigma}$ . We can associate a free energy,  $H(\boldsymbol{\sigma}, N, V, T)$ , to this partition function as

$$H(\boldsymbol{\sigma}, N, V, T) = -\frac{1}{\beta} \ln \Lambda(\boldsymbol{\sigma}, N, V, T). \quad (4.37)$$

The canonical partition function can then be written as

$$\mathcal{Z}(N, V, T) = \sum_{\{\boldsymbol{\sigma}\}} \exp(-\beta H(\boldsymbol{\sigma}, N, V, T)). \quad (4.38)$$

Consider now the Hamiltonian  $H(\boldsymbol{\sigma}, \nu, N, V, T)$ , which represents the free energy of a system, in which there are only displacive degrees of freedom. For a given  $\boldsymbol{\sigma}$  it can be expressed as

$$H(\boldsymbol{\sigma}, \nu, N, V, T) = U^0(\boldsymbol{\sigma}, N, V, T) + F_{\text{ex}}(\boldsymbol{\sigma}, \nu, N, V, T), \quad (4.39)$$

where  $U^0$  is the energy of the static configuration in the  $\{\nu \in \boldsymbol{\sigma}\}$  subspace with the lowest energy, i.e. the fully relaxed configuration and  $F_{\text{ex}}$  will then contain the remaining part of the free energy. The probability of a state described by  $\boldsymbol{\sigma}$  is then

$$P(\boldsymbol{\sigma}, N, V, T) = \frac{\exp(-\beta [U^0(\boldsymbol{\sigma}, N, V, T) + F_{\text{ex}}(\boldsymbol{\sigma}, N, V, T)])}{\mathcal{Z}(N, V, T)}. \quad (4.40)$$

As it has been shown in this chapter, in order to use  $P$  for calculating thermodynamical averages one needs to evaluate ratios of probabilities  $P$ ,

$$\frac{P(\boldsymbol{\sigma}_1, N, V, T)}{P(\boldsymbol{\sigma}_2, N, V, T)} = \frac{\exp(-\beta [U^0(\boldsymbol{\sigma}_1, N, V, T) + F_{\text{ex}}(\boldsymbol{\sigma}_1, N, V, T)])}{\exp(-\beta [U^0(\boldsymbol{\sigma}_2, N, V, T) + F_{\text{ex}}(\boldsymbol{\sigma}_2, N, V, T)])}. \quad (4.41)$$

$U^0(\boldsymbol{\sigma}, N, V, T)$  can now be approximated by taking the zero Kelvin value, which effectively is to approximate the Fermi-Dirac distribution by a step function [36]. Furthermore, in practice it is expected that  $F_{\text{ex}}$  is dominated by the vibrational free energy. A common approximation is therefore to remove the dependency of  $\boldsymbol{\sigma}$  on  $F_{\text{ex}}$  and also assume that  $F_{\text{ex}}$  is a linear combination of the composition [36]

$$F_{\text{ex}}(N, V, T) = N_a F_{\text{ex},A}(T) + N_b F_{\text{ex},B}(T). \quad (4.42)$$

If  $F_{\text{ex}}$  is linear in the composition then it can be completely removed in the canonical ensemble since it cancels out in the probability ratio. For the SGC ensemble it can also for many purposes be left out completely since a linear combination of concentration is just a shift of the chemical potential by a constant. The value of  $U^0(\boldsymbol{\sigma}, N, V)$  can now be calculated with a CE that maps  $\boldsymbol{\sigma}$  to the fully relaxed configuration. Finally  $P$  reduces to

$$P(\boldsymbol{\sigma}, N, V, T) = \frac{1}{\mathcal{Z}} e^{-\beta U^0(\boldsymbol{\sigma}, N, V)}. \quad (4.43)$$

A thermodynamic average of a property  $A(\boldsymbol{\sigma}, \nu)$  at  $N, V, T$  is then approximated by the value of  $A$  for the fully relaxed configuration. This means that even if the cluster expansion acts on the perfect lattice  $\boldsymbol{\sigma}$ , relaxation effects are still taken into consideration when calculating  $\langle A \rangle$ . Yet, any vibrational or temperature dependence of a property is largely neglected in this approach. If vibrational effects are important there are ways to incorporate these effects into a MC by also including the vibrational part of the free energy in the CE [37].

## Summary of the papers

### 5.1 Paper I

Paper I focused on the inorganic clathrate  $\text{Ba}_8\text{Ga}_{16}\text{Ge}_{30}$ . A CE was constructed to represent the energies of fully relaxed structures obtained from DFT calculations and subsequently sampled by MC simulations, from which the chemical order as a function of temperature was obtained, specifically the SOFs. Representative configurations for specific temperatures were extracted from the simulations and further analyzed with respect to their electrical transport properties using DFT

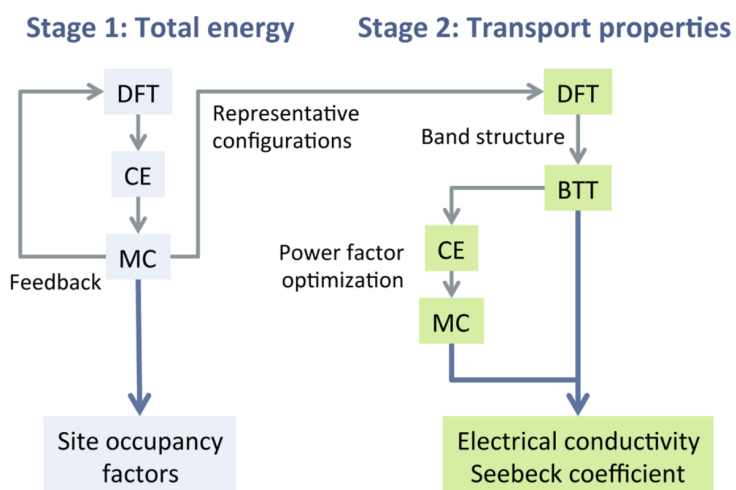


Figure 5.1: Schematic illustration of the methods employed in paper I. DFT: density functional theory; MC: Monte Carlo simulations; CE: alloy cluster expansion; BTT: Boltzmann transport theory.

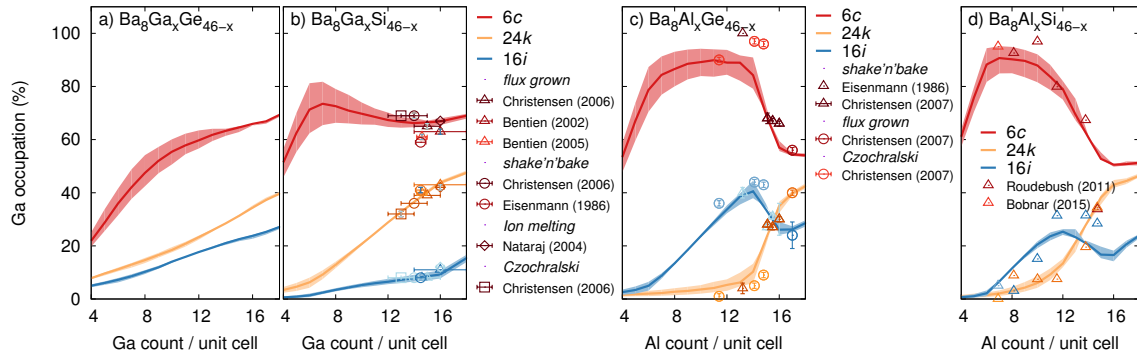


Figure 5.2: Site occupancy factors in intermetallic clathrates as a function of composition for Wyckoff sites 6c (red), 16i (blue), and 24k (orange). Solid lines show simulation results obtained at 700 K whereas the shaded regions indicate a variation by  $\pm 100$  K.

and Boltzmann transport theory (BTT) calculations. This combination of CE and MC simulations as well as DFT and BTT allowed us to obtain the thermoelectric power factor as a function of temperature (Fig. 5.1). The approach was validated by comparing the SOFs and transport coefficients with experimental data. Another CE was then constructed to represent the power factor as a function of the chemical configuration and was employed to determine the chemical ordering that maximized the power factor. The optimized structure yielded a power factor increase by more than 60% that was achieved by reducing the number of trivalent species on the 6c Wyckoff site. Hence, the approach developed in this paper demonstrates the use of CEs for structure optimization.

## 5.2 Paper II

Paper II addressed the chemical ordering in the clathrate systems  $\text{Ba}_8\text{Ga}_x\text{Ge}_{46-x}$ ,  $\text{Ba}_8\text{Ga}_x\text{Si}_{46-x}$ ,  $\text{Ba}_8\text{Al}_x\text{Ge}_{46-x}$ , and  $\text{Ba}_8\text{Al}_x\text{Si}_{46-x}$  as a function of composition (Fig. 5.2). In particular Al-based clathrates were found to display an extreme variation of SOFs as function of composition (Fig. 5.2c,d). The ordering in these materials can significantly impact the material properties, see e.g., paper I. Hence, an understanding of the ordering is crucial in order to understand and optimize these materials. To that end, in paper II for each system a CE was constructed based on the energies of fully relaxed structures obtained from DFT calculations and the SOFs were obtained from MC simulations. The simulated SOFs agree very well with experimental data (Fig. 5.2), which allowed us to clarify variations and trends in the experimental data. In particular the CE-MC simulations provide an explanation of the extreme variations of the SOFs in Al-based clathrates.

# Acknowledgments

To my family, thank you for all your love and support.

To Emma, thank you for making our home such a warm and affectionate place.

To my friends, both local and those from up north, thank you for all the fun times.

To my supervisor Paul Erhart, thank you for giving me the opportunity to do this work. Your dedication and knowledge about physics and especially your enthusiasm to share it is greatly appreciated. Also, thanks for your unwavering demand of quality in all of my work.

To my examiner, Göran Wahnström, thank you for your wisdom and leadership. Also, thank you for your dedication to deadlines which made sure this thesis was written on time.

I would also like to thank Thomas Holm Rod and the whole data analysis & modelling group at ESS in Copenhagen for welcoming me to visit the group and learn how professional software development is carried out.

To my office mate, Erik Fransson, thank you for being such a good friend and rubber duck. I only want to say one thing: *Tänk dig att du har en cell....*

To William Armando Muñoz, Magnus Rahm, Erik Fransson and Paul Erhart, thank you for working with me to develop icet.

To Joakim Brorsson and Anders Palmqvist, thank you for many helpful discussions regarding clathrates.

Finally, I am grateful for all current and former members of the Materials and Surface theory division that provide such a fun and exciting work atmosphere.



# Bibliography

- [1] T. Caillat, J.-P. Fleurial, and A. Borshchevsky, *Preparation and thermoelectric properties of semiconducting  $Zn_4Sb_3$* , Journal of Physics and Chemistry of Solids **58**, 1119 (1997).
- [2] E. S. Toberer, K. A. Sasaki, C. R. I. Chisholm, S. M. Haile, G. W. A., and S. G. J., *Local structure of interstitial Zn in  $\beta$ - $Zn_4Sb_3$* , physica status solidi (RRL) – Rapid Research Letters **1**, 253 (2007).
- [3] G. Jeffrey Snyder, M. Christensen, E. Nishibori, T. Caillat, and B. Brummerstedt Iversen, *Disordered zinc in  $Zn_4Sb_3$  with phonon-glass and electron-crystal thermoelectric properties*, **3**, 458 (2004).
- [4] H. J. Kim, E. S. Božin, S. M. Haile, G. J. Snyder, and S. J. L. Billinge, *Nanoscale  $\alpha$ -structural domains in the phonon-glass thermoelectric material  $\beta$ - $Zn_4Sb_3$* , Phys. Rev. B **75**, 134103 (2007).
- [5] C. Uher, in *Recent Trends in Thermoelectric Materials Research I*, Vol. 69 of *Semiconductors and Semimetals*, edited by T. M. Tritt (Elsevier, Atlanta, 2001), pp. 139 – 253.
- [6] B. C. Sales, D. Mandrus, and R. K. Williams, *Filled Skutterudite Antimonides: A New Class of Thermoelectric Materials*, Science **272**, 1325 (1996).
- [7] G. P. Meisner, D. T. Morelli, S. Hu, J. Yang, and C. Uher, *Structure and Lattice Thermal Conductivity of Fractionally Filled Skutterudites: Solid Solutions of Fully Filled and Unfilled End Members*, Phys. Rev. Lett. **80**, 3551 (1998).
- [8] G. S. Nolas, J. L. Cohn, and G. A. Slack, *Effect of partial void filling on the lattice thermal conductivity of skutterudites*, Phys. Rev. B **58**, 164 (1998).
- [9] G. Snyder and E. Toberer, *Complex thermoelectric materials*, Nature Materials **7**, 105 (2008).
- [10] D. T. Morelli and G. P. Meisner, *Low temperature properties of the filled skutterudite  $CeFe_4Sb_{12}$* , Journal of Applied Physics **77**, 3777 (1995).

## Bibliography

---

- [11] B. C. Sales, D. Mandrus, B. C. Chakoumakos, V. Keppens, and J. R. Thompson, *Filled skutterudite antimonides: Electron crystals and phonon glasses*, Phys. Rev. B **56**, 15081 (1997).
- [12] H. Kim, M. Kaviani, J. C. Thomas, A. Van der Ven, C. Uher, and B. Huang, *Structural Order-Disorder Transitions and Phonon Conductivity of Partially Filled Skutterudites*, Phys. Rev. Lett. **105**, 265901 (2010).
- [13] M. Christensen, S. Johnsen, and B. B. Iversen, *Thermoelectric clathrates of type I*, Dalton Trans. **39**, 978 (2010).
- [14] J. H. Roudebush, C. de la Cruz, B. C. Chakoumakos, and S. M. Kauzlarich, *Neutron Diffraction Study of the Type I Clathrate  $Ba_8Al_xSi_{46-x}$ : Site Occupancies, Cage Volumes, and the Interaction between the Guest and the Host Framework*, Inorg. Chem. **51**, 1805 (2012).
- [15] M. Ångqvist and P. Erhart, *Understanding Chemical Ordering in Intermetallic Clathrates from Atomic Scale Simulations*, Chemistry of Materials **29**, 7554 (2017).
- [16] M. Ångqvist, D. O. Lindroth, and P. Erhart, *Optimization of the Thermoelectric Power Factor: Coupling between Chemical Order and Transport Properties*, Chem. Mater. **28**, 6877 (2016).
- [17] J. Walecka, *Introduction to Statistical Mechanics* (World Scientific, 5 Toh Tuck Link, Singapore 596224, 2011).
- [18] D. Porter, K. Easterling, and M. Sherif, *Phase Transformations in Metals and Alloys, Third Edition (Revised Reprint)* (CRC Press, 6000 broken sound parkway nw suite 300, 2009).
- [19] L. Gharaee, M. Ångqvist, M. Rahm, and P. Erhart (unpublished).
- [20] P. Rogl, *Thermoelectrics Handbook* (CRC Press, 6000 broken sound parkway nw suite 300, 2005), Chap. 32, pp. 1–24.
- [21] A. V. Shevelkov and K. Kovnir, in *Zintl Phases*, No. 139 in *Structure and Bonding*, edited by T. F. Fässler (Springer Berlin Heidelberg, Tiergartenstraße 17, 69121 Heidelberg, 2011), pp. 97–142.
- [22] M. A. Avila, K. Suekuni, K. Umeo, H. Fukuoka, S. Yamanaka, and T. Takabatake,  *$Ba_8Ga_{16}Sn_{30}$  with type-I clathrate structure: Drastic suppression of heat conduction*, Applied Physics Letters **92**, 041901 (2008).

- 
- [23] G. S. Nolas, J. L. Cohn, G. A. Slack, and S. B. Schujman, *Semiconducting Ge clathrates: Promising candidates for thermoelectric applications*, Appl. Phys. Lett. **73**, 178 (1998).
- [24] G. K. H. Madsen, K. Schwarz, P. Blaha, and D. J. Singh, *Electronic structure and transport in type-I and type-VIII clathrates containing strontium, barium, and europium*, Phys. Rev. B **68**, 125212 (2003).
- [25] T. Matsui, J. Furukawa, K. Tsukamoto, H. Tsuda, and K. Morii, *Structure and properties of  $Ba_8Ga_{16}Ge_{30}$  clathrates by a novel synthesis method using CO gas reductive atmosphere*, Journal of Alloys and Compounds **391**, 284 (2005).
- [26] N. P. Blake, S. Lattturner, J. D. Bryan, G. D. Stucky, and H. Metiu, *Band structures and thermoelectric properties of the clathrates  $Ba_8Ga_{16}Ge_{30}$ ,  $Sr_8Ga_{16}Ge_{30}$ ,  $Ba_8Ga_{16}Si_{30}$ , and  $Ba_8In_{16}Sn_{30}$* , The Journal of Chemical Physics **115**, 8060 (2001).
- [27] M. Troppenz, S. Rigamonti, and C. Draxl, *Predicting Ground-State Configurations and Electronic Properties of the Thermoelectric Clathrates  $Ba_8Al_xSi_{46-x}$  and  $Sr_8Al_xSi_{46-x}$* , Chem. Mater. **29**, 2414 (2017).
- [28] J. M. Sanchez, F. Ducastelle, and D. Gratias, *Generalized cluster description of multicomponent systems*, Physica **128**, 334 (1984).
- [29] A. van de Walle, *Multicomponent multisublattice alloys, nonconfigurational entropy and other additions to the Alloy Theoretic Automated Toolkit*, Calphad **33**, 266 (2009), tools for Computational Thermodynamics.
- [30] L. J. Nelson, G. L. W. Hart, F. Zhou, and V. Ozolinš, *Compressive sensing as a paradigm for building physics models*, Phys. Rev. B **87**, 035125 (2013).
- [31] L. J. Nelson, V. Ozolinš, C. S. Reese, F. Zhou, and G. L. W. Hart, *Cluster expansion made easy with Bayesian compressive sensing*, Phys. Rev. B **88**, 155105 (2013).
- [32] E. Candes and M. Wakin, *An Introduction To Compressive Sampling*, IEEE Signal Processing Magazine **25**, 21 (2008).
- [33] T. Goldstein and S. Osher, *The Split Bregman Method for  $L_1$ -Regularized Problems*, SIAM Journal on Imaging Sciences **2**, 21 (2009).
- [34] W. Yin, S. Osher, D. Goldfarb, and J. Darbon, *Bregman Iterative Algorithms for  $l_1$ -Minimization with Applications to Compressed Sensing*, SIAM Journal on Imaging Sciences **1**, 26 (2008).

## Bibliography

---

- [35] N. Metropolis, A. W. Rosenbluth, M. N. Rosenbluth, A. H. Teller, and E. Teller, *Equation of State Calculations by Fast Computing Machines*, The Journal of Chemical Physics **21**, 1087 (1953).
- [36] G. Ceder, *A derivation of the Ising model for the computation of phase diagrams*, Computational Materials Science **1**, 144 (1993).
- [37] A. van de Walle and G. Ceder, *The effect of lattice vibrations on substitutional alloy thermodynamics*, Rev. Mod. Phys. **74**, 11 (2002).

# Paper I

## **Optimization of the Thermoelectric Power Factor: Coupling between Chemical Order and Transport Properties**

Mattias Ångqvist, Daniel O. Lindroth and Paul Erhart  
Chemistry of Materials **28**, 6877 (2016)



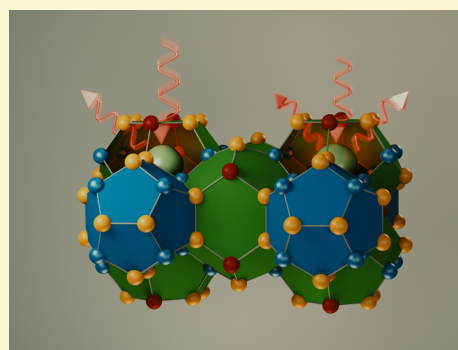
# Optimization of the Thermoelectric Power Factor: Coupling between Chemical Order and Transport Properties

Mattias Ångqvist, Daniel O. Lindroth, and Paul Erhart\*

Chalmers University of Technology, Department of Physics, S-412 96 Gothenburg, Sweden

Supporting Information

**ABSTRACT:** Many thermoelectric materials are multicomponent systems that exhibit chemical ordering, which can affect both thermodynamic and transport properties. Here, we address the coupling between order and thermoelectric performance in the case of a prototypical inorganic clathrate ( $\text{Ba}_8\text{Ga}_{16}\text{Ge}_{30}$ ) using a combination of density functional and Boltzmann transport theory as well as alloy cluster expansions and Monte Carlo simulations. The calculations describe the experimentally observed site occupancy factors and reproduce experimental data for the transport coefficients. By inverting the cluster expansion, we demonstrate that the power factor can be increased by more than 60% for certain chemical ordering patterns that involve reducing the number of the trivalent species on the 6c Wyckoff site. This enhancement is traced to specific features of the electronic band structure. The approach taken in the present work can be readily adapted to other materials and enables a very general form of band structure engineering. In this fashion, it can guide the computational design of compounds with optimal transport properties.



## 1. INTRODUCTION

Thermoelectric materials allow one to extract electrical currents from thermal gradients and vice versa.<sup>1,2</sup> They have found applications in various areas including, for example, power generation in remote locations, waste heat recuperation, and active cooling. The thermodynamic efficiency of the conversion process is quantified by the thermoelectric figure of merit  $zT$ . The latter depends on the Seebeck coefficient  $S$ , which measures the coupling strength between a thermal gradient and the generated potential difference, the electrical conductivity  $\sigma$  as well as the thermal conductivity  $\kappa$  according to

$$zT = TS^2\sigma/\kappa \quad (1)$$

The  $S^2\sigma$  term in the numerator is known as the thermoelectric power factor.<sup>3</sup> While in efforts to increase  $zT$  it has received relatively less attention than the thermal conductivity  $\kappa$ ,<sup>4–7</sup> several strategies for its enhancement have been proposed. The key challenge is that  $S$  and  $\sigma$  are anticorrelated insofar as the Seebeck coefficient usually decreases with carrier concentration, whereas the electrical conductivity increases.<sup>3</sup> To mitigate this situation, Hicks and Dresselhaus suggested to reduce dimensionality by means of quantum well structures,<sup>8,9</sup> while Mahan and Sofo showed conceptually that optimal conditions are obtained for a very narrow distribution of states with high group velocities.<sup>10</sup> These ideas were in fact later realized, for example, in the form of nanostructuring,<sup>11–13</sup> which also is useful for reducing the thermal conductivity, resonant levels,<sup>3</sup> and band structure engineering.<sup>14–16</sup> It is also worthwhile noting the extremely high power factors that were achieved at low temperatures in  $\text{FeSb}_2$ .<sup>17,18</sup> They have been attributed to

strong electronic correlation resulting from the interplay between localization and partially occupied states.

While most of the aforementioned approaches have been devised in the context of “simple” lattice structures, many thermoelectric materials including skutterudites, inorganic clathrates as well as other Zintl compounds, and half-Heusler alloys<sup>2</sup> are multicomponent systems that exhibit some form of chemical order. Here, using the prototypical inorganic clathrate<sup>19,20</sup>  $\text{Ba}_8\text{Ga}_{16}\text{Ge}_{30}$  (Figure 1) as an example, we demonstrate that the power factor can be enhanced by more than 60% by optimizing the chemical order. To this end, we first resolve the coupling between the chemical order and

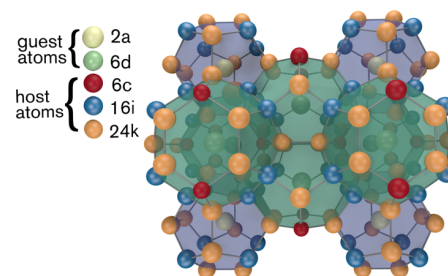


**Figure 1.** Crystal structure of type I clathrates. The guest species (Ba) occupies Wyckoff sites of type 2a and 6d, while the host species (Ga, Ge) occupy Wyckoff sites of type 6c, 16i, and 24k.

Received: May 25, 2016

Revised: September 10, 2016

Published: September 12, 2016

transport properties, in particular the power factor, and we then employ an inverse design approach to identify the structure that maximizes the power factor. This approach yields a clear guideline for maximizing the power factor by structural optimization that we anticipate to be in principle transferable to other inorganic clathrates.

In this work, we employ a combination of density functional theory (DFT) and Boltzmann transport theory (BTT) calculations with alloy cluster expansions (CE) and Monte Carlo (MC) simulations (Figure 2). This approach is directly

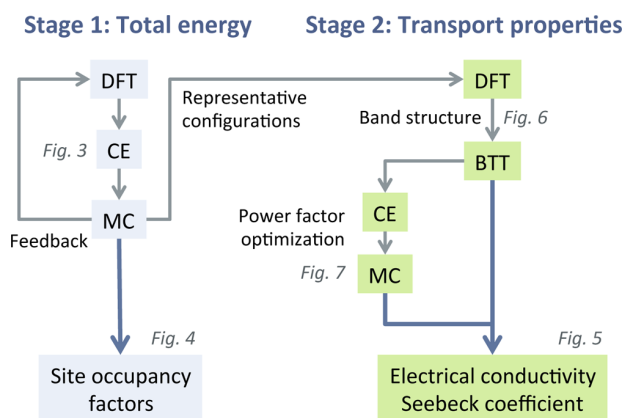


**Figure 2.** Schematic illustration of the relation between the methods employed in the present work. DFT: density functional theory; MC: Monte Carlo simulations; CE: alloy cluster expansion; BTT: Boltzmann transport theory.

applicable to other materials that exhibit a variable chemical order. It thereby opens up the avenue for a more controlled and systematic design of structures with optimal transport properties that is not limited to thermoelectric materials.

The remainder of the paper is organized as follows. In the following section, we construct a model for the chemical order based on electronic structure calculations and describe the variation of the site occupancy factors with temperature. Using configurations that are representative for the chemical order at different temperatures, we then analyze the transport properties and construct a model that maps ordering patterns to the power factor at 900 K. This model is subsequently employed to determine the chemical ordering that maximizes the power factor.

## 2. CALCULATION METHODS

**2.1. Chemical Ordering.** Density functional theory (DFT) calculations were carried out using the projector augmented wave method<sup>21,22</sup> as implemented in the Vienna ab initio simulation package.<sup>23,24</sup> Exchange–correlation effects were treated within the generalized gradient approximation as parametrized by Perdew, Burke, and Ernzerhof (PBE).<sup>25</sup> A set of 200 structures based on the 54-atom primitive unit cell was created by randomly assigning Ga and Ge atoms to different Wyckoff sites that comprise the host structure. A further set of 100 structures was created in the same fashion but subject to the condition that Ga–Ga first-nearest neighbors were disallowed. For each structure, both the ionic positions and the cell metric were fully relaxed until all atomic forces were less than 10 meV/Å and absolute stresses below 0.1 kbar. In these calculations, the Brillouin zone was sampled using a  $\Gamma$ -centered  $3 \times 3 \times 3$   $k$ -point mesh, the plane wave basis set was

expanded up to a cutoff energy of 243 eV, and the electronic self-consistency loop was terminated if the change in the total energy dropped below  $10^{-5}$  eV between consecutive iterations.

Subsequently, the DFT energy landscape as well as quantities such as the band gap and the power factor were represented by cluster expansions (CE) of the form<sup>26,27</sup>

$$A = A_0 + \sum_{\alpha} m_{\alpha} J_{\alpha} \bar{\Pi}_{\alpha}(\Sigma) \quad (2)$$

where  $A$  denotes the respective quantity of interest and the summation runs over all symmetry distinct clusters (singlets, pairs, triplets...). Each cluster has a multiplicity  $m_{\alpha}$  and is associated with an effective cluster interaction (ECI)  $J_{\alpha}$ . The cluster correlations  $\bar{\Pi}_{\alpha}$  are computed as symmetrized averages of products over the pseudospin vector  $\Sigma$ . The latter represents the lattice sites associated with the host matrix where  $\Sigma = \pm 1$  for Ge and Ga, respectively.

The ECIs were obtained using the compressive sampling technique<sup>28</sup> adapted for CE construction.<sup>29</sup> The split Bregman algorithm<sup>30,31</sup> was employed to solve the optimization problem using parameters of  $\mu = 0.001$  (which controls the sparseness of the solution) and  $\lambda = 100$  (see refs 29, 31 for details concerning the role of these parameters). A range of different values for  $\mu$  and  $\lambda$  were tested. Within reasonable bounds (see e.g., ref 29), these parameters were found to have inconsequential effects on the results presented here.

Each CE was carefully tested with respect to its predictive power using both cross-validation and ground-state searches. Due to the large number of different crystallographic sites, there is a large number of distinct clusters, 3 singlets, 13 pairs, and 26 triplets relative to a 5 Å cutoff radius, respectively. These numbers are noticeably larger than for simpler structures such as face-centered cubic (see Figure S7), whence the compressive sampling approach is particularly useful.<sup>29</sup>

The CEs were sampled using Monte Carlo (MC) simulations in the canonical ensemble. Supercells typically comprising  $2 \times 2 \times 2$  unit cells were initialized at a temperature of 1200 K and then cooled to 0 K at a rate of 50 K per MC cycle (1 MC cycle is equivalent to  $N$  trial moves, where  $N$  is the number of sites in the simulation). At each new temperature, the system was first equilibrated for 50 000 MC cycles and then sampled for 100 000 MC cycles. The effect of supercell size on the SOFs is illustrated in Figure S8.

**2.2. Electrical Transport Properties.** For several configurations, the wave function of the fully relaxed structure was converged using a  $\Gamma$ -centered  $4 \times 4 \times 4$   $k$ -point mesh, followed by a non self-consistent computation of the eigenenergy spectra on a  $\Gamma$ -centered  $20 \times 20 \times 20$  mesh. Using the interpolated eigenenergy spectra and electronic group velocities, the electrical conductivity and the Seebeck coefficient were computed using both an in-house and the BOLTZTRAP code<sup>32</sup> by evaluating the following expressions that are obtained within the relaxation time approximation to the Boltzmann transport equation<sup>32–34</sup>

$$\sigma = \frac{2e^2}{\Omega} \sum_{ik} g_k v_{ik} \otimes v_{ik} \tau_{ik} \left( \frac{\partial f}{\partial \epsilon} \right)_{\epsilon=\epsilon_{ik}} \quad (3)$$

$$S = \frac{\sigma^{-1}}{eT} \sum_{ik} g_k v_{ik} \otimes v_{ik} \tau_{ik} [\epsilon_{ik} - \mu_c] \left( \frac{\partial f}{\partial \epsilon} \right)_{\epsilon=\epsilon_{ik}} \quad (4)$$

Here,  $\Omega$  is the unit cell volume,  $g_k$  is the  $k$ -point weight,  $i$  refers to the band index,  $\tau_{ik}$  is the mode and momentum dependent

lifetime,  $v_{ik} = \hbar^{-1} \partial \epsilon_{ik} / \partial k$  is the group velocity,  $f$  is the occupation function, and  $\mu_e$  is the electron chemical potential. In the present work, the scattering time was assumed to be momentum- and state-independent as commonly done in calculations of this type.<sup>32,34,35</sup>

We note that semilocal exchange–correlation functionals such as the PBE functional used in the present work are known to systematically underestimate the band gap. This error can have a strong impact on the transport properties in weakly doped materials. In the present work we are, however, concerned with very high charge carrier concentrations as thermoelectrics are typically heavily (degenerately) doped semiconductors. As shown in Figure S3, under these conditions, the magnitude of the band gap (while assuming rigid bands) has a very small effect on the transport properties, whence the band gap underestimation is of minor concern for the present work.

As a further validation, we also carried out calculations for selected structures using the modified Becke–Johnson (mBJ) functional,<sup>36,37</sup> which yields much improved band gaps and band structures compared to PBE-DFT. The results (Figure S4) demonstrate that, apart from an increase in the band gap, the conduction and valence band structure near the band edges are, however, very similar between PBE and mBJ-DFT, especially in the region that determines the transport properties under degenerate doping conditions. For all calculations reported below, we therefore employ the PBE-DFT band structure.

### 3. CHEMICAL ORDERING

Inorganic clathrates of type I, such as  $\text{Ba}_8\text{Ga}_{16}\text{Ge}_{30}$ , belong to space group  $^{38} Pm\bar{3}n$  (international tables of crystallography number 223) and feature two smaller and six larger cages per unit cell.<sup>19,20,39</sup>  $\text{Ba}_8\text{Ga}_{16}\text{Ge}_{30}$  has been investigated extensively both experimentally<sup>40–45</sup> and theoretically,<sup>35,41,46–48</sup> especially because of its promising thermoelectric properties. Here, the host structure is composed of Ga and Ge atoms, which occupy 6c, 16i, and 24k Wyckoff sites (Figure 1)<sup>49</sup> as revealed by experimental measurements of the site occupancy factors (SOFs).<sup>39</sup> Analysis of diffraction data yields for example Ga occupancies between 60 and 76% for the 6c site, which deviates considerably from the value of  $\text{Ga}/(\text{Ga}+\text{Ge}) = 16/(16 + 30) = 35\%$  corresponding to the nominal stoichiometry of the compound.<sup>43</sup> The experimental observations have been condensed into a set of rules for the SOFs,<sup>39</sup> partially based on calculations,<sup>46</sup> which have shown that bonds between trivalent species, in the present case Ga atoms, are energetically unfavorable.

Here, in order to model the chemical order, we constructed an alloy CE based on a set of total energies for two hundred structures that were obtained from DFT calculations. The structures were generated by randomly assigning Ga and Ge atoms to lattice sites, while maintaining a ratio of 16:30. The number of structures can be compared to the total number of possible configurations, which, excluding symmetry, is close to  $10^{12}$  for the 54-atom primitive unit cell. The CE nonetheless yields a very low cross-validation score of 0.9 meV/atom and excellent overall agreement with the reference data as illustrated by a juxtaposition of total energies from DFT and CE (Figure 3a). The final CE includes 3 singlet, 13 pair, and 24 triplet terms and is rather short ranged (Figure 3b).

It must be noted that the stoichiometry of experimentally synthesized clathrates often deviates from the ideal ratio of

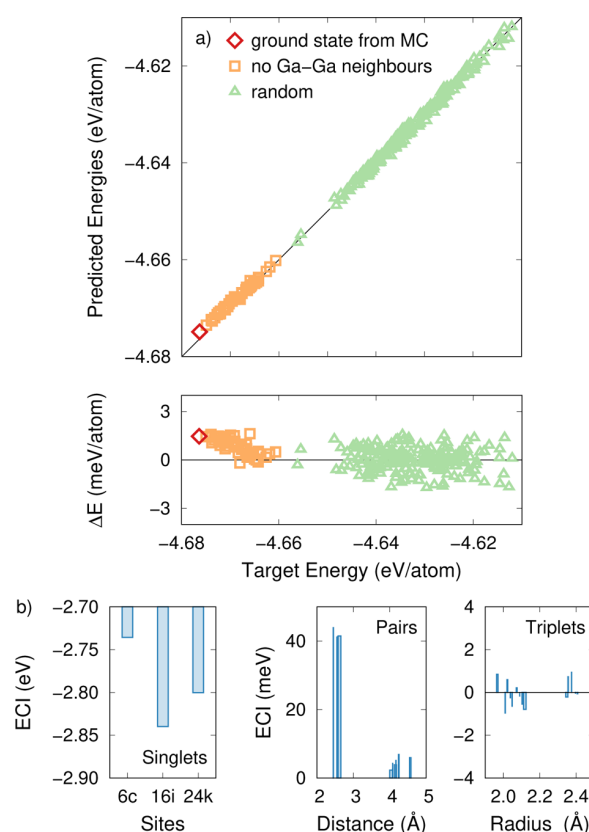


**Figure 3.** (a) Total energies obtained from cluster expansion (predicted) and electronic structure calculations (target). The data points shown by triangles were employed for constructing a cluster expansion for the total energy. Squares indicate data from structures without first-nearest-neighbor Ga–Ga bonds, whereas diamonds represent the structure obtained via a simulated annealing procedure from MC simulations. (b) Effective cluster interactions (ECI) of the total energy cluster expansion as a function of cluster size.

8:16:30 for Ba:Ga:Ge.<sup>39,50</sup> These effects can in fact be represented using the total energy CE used in the present work.<sup>51</sup> In the case of  $\text{Ba}_8\text{Ga}_{16}\text{Ge}_{30}$ , the variation of the SOFs with composition is, however, relatively weak and, as apparent from the comparison below, its description is not essential for achieving good agreement with experimental transport coefficients. The effect of composition on ordering will therefore be the topic of a separate publication.<sup>51</sup>

The temperature dependence of the Ga SOFs was extracted by sampling the total energy CE with Monte Carlo (MC) simulations (Figure 4a). From the data, it is apparent that already close to the melting temperature the SOFs deviate strongly from the stoichiometric ratio, which would imply a value of  $16/(16 + 30) = 35\%$ , indicating that the configurational entropy does not entirely override the energy associated with ordering even at these temperatures. As the temperature is reduced, the SOFs deviate more strongly from 35%, as the chemical distribution is increasingly dictated by energy. The variation in the SOFs is primarily the result of the energy penalty on trivalent (Ga) first-nearest-neighbor pairs that has been pointed out earlier<sup>46</sup> and is also apparent in the ECIs (Figure 3b). It is therefore logical that the number of Ga–Ga bonds monotonically decreases with decreasing temperature, as shown in Figure 4b.

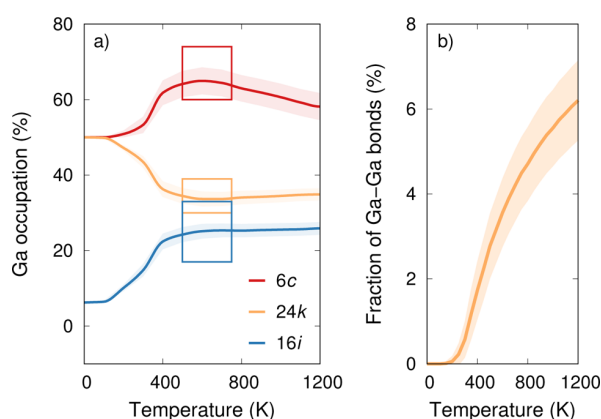


**Figure 4.** (a) Gallium site occupancy factors as a function of temperature from MC simulations using a  $2 \times 2 \times 2$  supercell. The shaded regions indicate one standard deviation. The boxes represent the range of the experimental SOF data and roughly indicate the temperature range, over which the chemical order appears to be frozen during sample preparation. (b) Fraction of first-nearest Ga–Ga bonds as a function of temperature. For comparison, the average fraction of Ga–Ga bonds for a completely random structure is  $c_{\text{Ga}}^2 = 12.1\%$ .

The experimentally observed SOF ranges are indicated by rectangles in Figure 4a. In experimental settings, chemical ordering will at some temperature become kinetically hindered as it requires atomic rearrangement, which is a temperature activated process. The precise conditions, at which freezing of the chemical order occurs, are unknown whence a temperature window between 550 and 720 K has been indicated in Figure 4a. Within the indicated temperature range, the agreement between experiment and model is actually excellent, supporting the present approach. The experimentally observed structure can thus be considered as a state of intermediate chemical order, which has been established during cooling as the result of slowing kinetics.

At low temperatures, the system eventually reaches a fully ordered state with rhombohedral symmetry (space group R3, ITC no. 146, see Table S1 for a compilation of the crystallographic parameters). As a further validation of the CE, the total energy of this ordered-state structure was calculated with DFT, which gave a value that deviates by less than 2 meV/atom from the CE value, demonstrating not only the accuracy but the predictive quality of the latter. This fact is even more remarkable given that the structures used for CE construction, which were obtained by random sampling, generally contain a much larger number of Ga–Ga bonds than the configurations observed during the MC simulations, even at temperatures close to the melting point.

The ordered configuration, from here on referred to as the ground-state structure, is characterized by the absence of Ga–Ga bonds in the first neighbor shell and a minimal number of Ga–Ga bonds in the second and third shell. In addition, it also minimizes the Ga SOF for Wyckoff site 16i.

## 4. ELECTRICAL TRANSPORT PROPERTIES

**4.1. Comparison to Experiment.** The electrical transport properties of  $\text{Ba}_8\text{Ga}_{16}\text{Ge}_{30}$  have been previously investigated using first-principles calculations employing either structures that were constructed using intuition and energy minimization<sup>34,35,46</sup> or the virtual crystal approximation.<sup>47</sup> Here, we therefore systematically discriminate the effect of thermally

induced disorder on these properties. Specifically, we target *n*-type material, which is commonly associated with Ge-excess. In this section, we benchmark our structural model and establish two crucial parameters, namely, the charge carrier density and the effective electronic lifetime, by comparing our calculations with experimental transport data for *n*-type  $\text{Ba}_8\text{Ga}_{16}\text{Ge}_{30}$ .<sup>42,44,52–55</sup>

Five representative configurations per temperature were extracted from MC simulations at 600, 900, and 1200 K, respectively. The average and standard deviation of the total energy of these configurations correspond to the energy distribution at the respective temperatures sampled by MC simulations. In addition, we considered ten random structures and the ground-state structure. The electrical conductivity  $\sigma$  and the Seebeck coefficient  $S$  were computed within the framework of the Boltzmann transport equation,<sup>32</sup> as described in the above.

We first consider the Seebeck coefficient  $S$  (see eq 4), which varies with the charge carrier concentration  $n_e$  (Figure S1). For  $n_e = 3 \times 10^{20} \text{ cm}^{-3}$ , the calculations for the MC generated structures agree well with the experimental data (Figure 5a).<sup>42,44,52,53</sup> This charge carrier density in turn is in good agreement with previous estimates based on experimental data.<sup>35,47</sup> While the variation among the MC generated structures—regardless of the temperature they represent—is rather small, the results for the random structures—and to a lesser extent the ground-state structure—differ more notably both in magnitude and the temperature at which  $S$  is extremal.

We note that with regard to the Seebeck coefficient, the temperature dependence in the experiments appears slightly more linear than in the calculations, which leads to some deviation at low temperatures. This behavior could be related to the assumption of a mode- and momentum-independent relaxation time (compare section on Calculation Methods) and also affects the power factor (see below).

After having established the carrier density, which is kept constant at  $n_e = 3 \times 10^{20} \text{ cm}^{-3}$  from this point onward, it is possible to assess the electrical conductivity  $\sigma$  (see eq 3). The electronic lifetimes were assumed to be mode- and momentum-independent  $\tau_{\text{eff}} \approx \tau_i(\mathbf{k})$  (see e.g., refs 32, 34, 35, 46, 47).<sup>56</sup> Since an explicit calculation of  $\tau_i(\mathbf{k})$  for  $\text{Ba}_8\text{Ga}_{16}\text{Ge}_{30}$  is computationally currently impractical, we use an effective lifetime model with a simple temperature dependence  $\tau_{\text{eff}} = \tau_{300}(300 \text{ K}/T)^{1/2}$  to represent acoustic phonon (piezoelectric) scattering,<sup>57</sup> which using  $\tau_{300} = 15 \text{ fs}$  yields very good agreement with experimental data (Figure 5b). The thus obtained effective lifetime at 300 K is in fact very similar to values from previous studies (see e.g., refs 35, 47), which, however, neglected the variation of  $\tau$  with temperature. It is apparent that the electrical conductivity  $\sigma$  again shows only a modest variation among the MC structures.

Given the Seebeck coefficient  $S$  and the electrical conductivity  $\sigma$ , we can now evaluate the power factor  $S^2\sigma$ , which most clearly highlights the effect of order on the electrical transport properties (Figure 5c). The MC-generated structures yield power factors of 15 to  $18 \mu\text{W}/\text{K}^2\text{cm}$  at 900 K, which agrees well with experimental data.<sup>42,44,52,53</sup> The maximum power factor occurs at approximately 800–900 K, which matches the range observed in most experiments. By comparison, the ground-state ( $14 \mu\text{W}/\text{K}^2\text{cm}$  at 900 K) and random structures ( $9.6 \pm 3.7 \mu\text{W}/\text{K}^2\text{cm}$  at 900 K) yield somewhat lower maxima. This suggests that the chemical ordering that is naturally established during synthesis

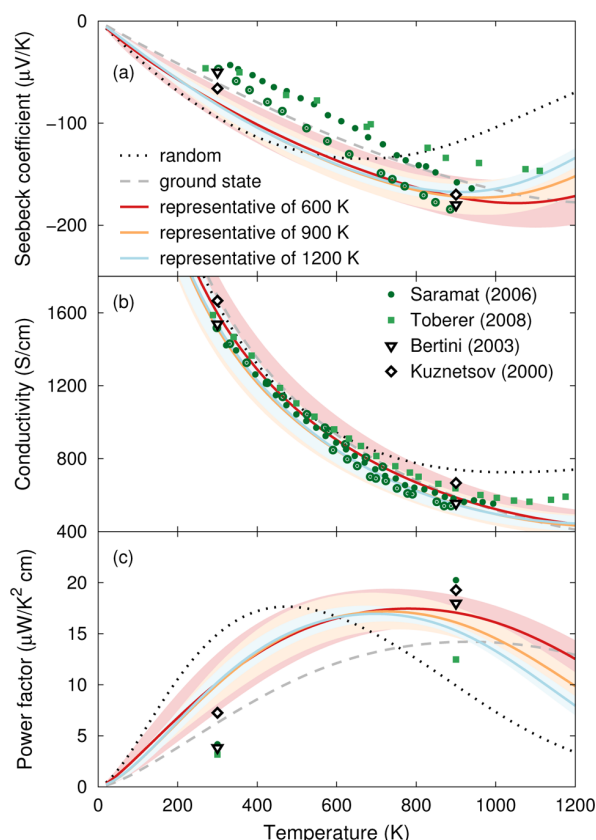


**Figure 5.** Electrical transport properties of *n*-type material at a carrier density of  $3 \times 10^{20} \text{ cm}^{-3}$ . (a) Seebeck coefficient, (b) electrical conductivity, and (c) power factor as a function of temperature from calculations in comparison with experimental data from refs 42, 44, 52, 53. The degree of chemical order has a clear effect on the electrical transport properties as is evident by comparing the results from samples with a random distribution (dotted lines), the ground-state structure (dashed lines), and configurations representative of the chemical order at 600 K (solid red), 900 K (solid orange), and 1200 K (solid blue). In the case of the MC-generated structures, the corresponding shaded areas represent one standard deviation.

corresponds to relatively optimal conditions with regard to the power factor, an observation that will be explored in detail below. Furthermore, we find that maximizing the power factor by variation of the charge carrier density  $n_e$  (Figure S2) yields only a slight improvement of about 5%. This suggests that the experimental samples are already close to optimality with regard to  $n_e$ .

**4.2. Order and Electronic Structure.** The data presented above demonstrates that the power factor changes non-monotonically as a function of chemical order: The MC generated structures (intermediate level of order) exhibit on average higher power factors than both the ground state (highest degree of order) and the random structures (lowest degree of order). To resolve this behavior, it is instructive to explore the effect of chemical order on the electronic structure as both Seebeck coefficient  $S$  and electrical conductivity  $\sigma$  are primarily determined by the electronic eigenenergies and group velocities, see eqs 3 and 4.

The electronic band structures of configurations representing different degrees of chemical order (Figure 6) reveal that decreasing chemical order causes a systematic lowering of the band gap and a reduction in the dispersion of the lowermost conduction band level, which implies decreasing group velocities. With regard to the electrical conductivity  $\sigma$ , these two effects oppose each other as the  $(\partial f / \partial \epsilon)_\epsilon = \epsilon_{ik}$  term in eq 3 increases with decreasing band gap, whereas smaller group velocities  $v_i(k)$  cause a reduction of the other term in the integrand. (In the widely adopted effective mass approximation, this is equivalent to asserting an increase in the charge carrier concentration and a reduction of the mobility due to a higher effective mass (smaller curvature), see e.g., ref 2.) In the current case, the two terms appear to largely cancel each other as the net effect of order on  $\sigma$  is comparably small (Figure 5b).

To further resolve the coupling between order and the electrical transport properties, a closer inspection of the underlying band structures is instructive. To this end, we analyzed the mode-resolved contributions to the power factor, which are most sensitive to the group velocity. It is found that for the ground-state configuration, the largest contribution to  $S$  stems from states in the vicinity of the  $M$  point, which is the location of the CBM [fully ordered, Figure 6a,  $S^2\sigma = 14.2 \mu\text{W/}$

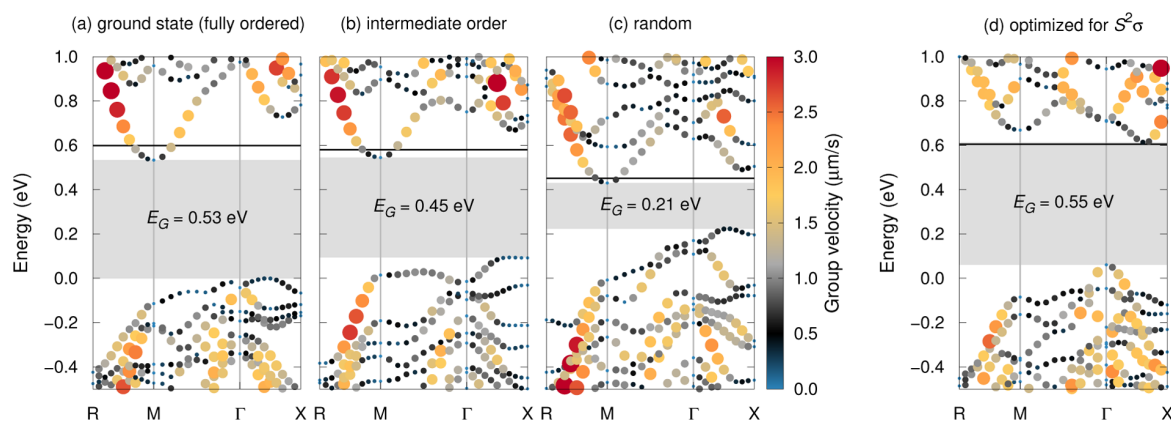


**Figure 6.** Effect of chemical order on the electronic structure. Band structures representing (a) the fully ordered ground state, (b) a configuration with intermediate order extracted from a MC simulation, (c) a random distribution, and (d) the structure optimized for maximum power factor at 900 K. The color scale and the size of the circles indicate the group velocity. The position of the Fermi level is shown by horizontal dashed lines. The energy scales of the different configurations were aligned using the Ba-1s states as described in ref 58, and the VBM of the ground state was arbitrarily set to zero.

$\text{K}^2 \text{ cm}$  at 900 K and  $n_e = 3 \times 10^{20}/\text{cm}^3$ ]. While in the case of intermediate chemical order the relative contribution of these states is reduced, higher lying states for example along the  $\Gamma$ -X direction are shifted downward and thus closer to the Fermi level, providing a significantly larger contribution than in the case of the ground-state structure (Figure 6b,  $S^2\sigma = 18.7 \mu\text{W}/\text{K}^2 \text{ cm}$ ). The gain in the density of states in the vicinity of  $\mu_e + k_B T$  outweighs the reduced dispersion (smaller group velocities) around the  $M$ -point and gives rise to a slight increase of the power factor relative to the ground-state configuration. If the degree of chemical order is further reduced, the effect of an increase in the density of states near the Fermi energy levels off (Figure 6c,  $S^2\sigma = 12.2 \mu\text{W}/\text{K}^2 \text{ cm}$ ), whereas level localization (and thus reduction of the group velocities) proceeds, causing the power factor to drop again.

The origin of the reduction of band gap and level of dispersion with decreasing chemical order can be understood by recalling some general principles from defect physics. The ground-state structure represents a fully ordered structure, whereas disordering can be thought of as the insertion of antisite defects.<sup>59</sup> As these are intrinsic defects with small lattice distortions, the associated defect states are hybridized with band states (see e.g., refs 3, 60, 61); yet, the associated levels are to some extent localized. In  $\text{Ba}_8\text{Ga}_{16}\text{Ge}_{30}$  (and similar systems), the formation energies for such antisites are obviously very small, whence defect concentrations are easily in the percent range and the collective effect on the band structure becomes significant.

**4.3. Power Factor Optimized Structures.** To substantiate the above argumentation, additional CEs were constructed for the band gap  $E_G$  as well as the power factor at 900 K ( $n_e = 3 \times 10^{20}/\text{cm}^3$ ), for which we obtained cross-validation scores of 0.05 eV and  $1.5 \mu\text{W}/\text{cmK}^2$ , respectively. The CEs were subsequently sampled using MC simulations based on the CE for the total energy constructed earlier. Using the total energy as order parameter,<sup>62</sup> these simulations confirm for a large data sample that the band gap decreases monotonically with chemical disordering (Figure 7b), whereas the power factor exhibits a maximum at a finite amount of disorder, which quite closely coincides with the average level of order between 600 and 1200 K.

Based on the CE for the power factor, we are now in a position to search for chemical ordering patterns that maximize the power factor. To this end, simulated annealing runs were carried out on the landscape corresponding to  $-S^2\sigma$  with an appropriate effective temperature scale. In this fashion, several structures were obtained with predicted power factors of approximately  $S^2\sigma = 24 \mu\text{W}/\text{K}^2 \text{ cm}$ , which were confirmed by a subsequent DFT-BTT calculation yielding about  $27 \mu\text{W}/\text{K}^2 \text{ cm}$  (Table S1).

The optimized structures are only about 8 meV/atom higher than the ground-state structure, and thus, they are energetically comparable to the structures obtained during the MC simulations described above. The most striking difference to both the ground state and MC-generated representative structures described above is the redistribution of Ga occupation from the  $6c$  to the  $16i$  site (ground-state structure:  $\text{SOF}(6c) = 50\%$ ; power factor optimized structure:  $\text{SOF}(6c) = 0\%$ ; see Table S1), whereas the average occupation of  $24k$  sites is unaffected. In terms of the electronic structure, this redistribution gives rise to a significantly higher density of states in the vicinity of the conduction band edge along with a notably larger contribution from Ga atoms on  $24k$  sites than in

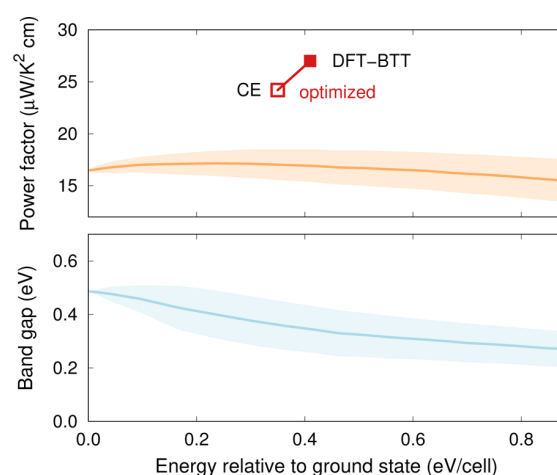


**Figure 7.** (a) Power factor and (b) band gap as a function of order (measured by the total energy) from MC-CE simulations. The maximum attainable power factor according to CE and DFT-BTT is indicated by red symbols. The shaded regions represent one standard deviation.

either the ground state or the MC-generated structures (Figure S6). Here, the vanishing Ga occupancy of  $6c$  Wyckoff sites is a key feature as we generally find that larger power factors are correlated with a low  $6c$  SOF.

It is now very instructive to analyze the features of the electronic structure that underlie the outstanding power factor of this configuration. A closer inspection of the band structure (Figure 6d) reveals that unlike the other structures (Figure 6a–c), all of which feature a CBM at the  $M$ -point, for the optimized structure the CBM is located along the  $\Gamma$ -X direction. This is the result of the lower energy of the corresponding states compared to the other structures. At the same time, the high degree of order ensures that the configuration has a large band gap ( $E_G = 0.55$  eV) comparable in magnitude to the ground-state structure ( $E_G = 0.54$  eV).

The integrand in the expression for the Seebeck coefficient eq 4 is maximal if the group velocity at approximately  $\mu_e + 1.5k_B T$  is large, which requires dispersed (delocalized) states. At the same time, it is desirable to have many states in this energy window, which would be achieved by localization (nondispersed states). Since similar considerations apply to  $\sigma$ , optimizing  $S^2\sigma$  thus tries to strike a balance between two diametrically opposed features. A three-dimensional visualization of the CBM (Figure S5) shows that the optimized configuration achieves a large power factor by featuring multiple CBM pockets with large group velocities in the relevant energy range.

Similar features in the band structure involving “complex carrier pocket shapes”<sup>63</sup> were found to enhance thermoelectric performance also in other materials (see e.g., refs 14, 16, 63–65). The electronic structures that were observed in these cases can be thought of as realizations of the conditions formulated by Mahan and Sofo<sup>10</sup> according to which one seeks a narrow distribution of states near the Fermi level with high group velocities. While enhanced thermoelectric performance due to the existence of multiple band extrema has been shown to be intrinsic to some materials,<sup>64,65</sup> it has been demonstrated that the relevant features can also be engineered by, for example, nano-inclusions,<sup>14</sup> careful selection of the components,<sup>16</sup> or volumetric band alignment via alloying.<sup>63</sup> The

present results show that this level of band structure engineering can even be accomplished by controlling the chemical order in a material. Furthermore, the present approach demonstrates that the identification of materials and compositions can be achieved using models that do not explicitly describe the electronic structure as long as they are properly trained with respect to higher-level calculations.

## 5. CONCLUSIONS

In the present work, we used density functional theory calculations in conjunction with Monte Carlo simulations, alloy cluster expansions, and Boltzmann transport theory to investigate the coupling between chemical order and the electrical transport properties in the prototypical inorganic clathrate  $\text{Ba}_3\text{Ga}_{16}\text{Ge}_{30}$ .

The temperature dependence of the SOFs obtained from MC–CE simulations shows a strong asymmetry between different Wyckoff sites. The predicted SOFs in the temperature range between 550 and 720 K are in good agreement with experimental data. This observation provides a very sensible estimate for the temperature range, in which the chemical order is kinetically frozen in as the material cools down after synthesis. A simulated annealing procedure furthermore lead to a ground-state structure that is primarily characterized by the absence of first-nearest neighbor Ga–Ga bonds.

Subsequently, the electrical conductivity  $\sigma$  and Seebeck coefficient  $S$  were computed for  $n$ -type conditions using a DFT–BTT approach for the ground-state structure, a set of configurations representing the chemical order at different temperatures, as well as several random structures. The magnitude and temperature dependence of the Seebeck coefficient calculated for the representative structures at an electron concentration of  $n_e = 3 \times 10^{20}/\text{cm}^3$  was shown to match experimental data. Using a minimal model for the electronic lifetime based on scattering by acoustic phonons, we then achieved close agreement between experiment and calculations for both the electrical conductivity  $\sigma$  and power factor  $S^2\sigma$ . Thus-equipped, the relation between chemical order and the power factor was scrutinized. It was shown that the power factor exhibits a nonmonotonic dependence on order (and temperature) with its average value exhibiting a maximum roughly in the range found in previous experiments.

Using a direct combination of DFT–BTT and MC–CE, we then identified structural motifs that maximize the power factor. Specifically, it was demonstrated that this can be achieved by minimizing the Ga SOF for  $6c$  Wyckoff sites, which gives yields calculated power factors up to  $27 \mu\text{W}/\text{K}^2\text{cm}$ , corresponding to an improvement of about 60% compared to the “normal” order. The enhancement can be traced to an increase in the density of states near the conduction band edge with only a small reduction in the group velocities.

It is beyond the scope of this work to provide a recipe for synthesizing the exact structure in question, but the relatively small energy cost associated with the depopulation of the  $6c$  site suggests that it is thermodynamically within reach. It is possible, for example, that alloyed clathrates<sup>66–69</sup> provide means to control order more consciously, albeit at the cost of a much more complex parameter range. Other materials that exhibit partial ordering/disordering such as the cobaltates and skutterudites, Zintl compounds, as well as complex alloys<sup>2,16,70–75</sup> can be anticipated to exhibit similar features and thus also warrant further study.

Here, modeling and simulation could provide useful guidance for navigating the complex and multidimensional composition space. In this context, the approach utilized in the present work, which combines electronic structure calculations of transport properties with machine learning protocols, could prove to be highly useful for band structure engineering. In this fashion, it can guide the computational design of compounds with optimal transport properties.

## ■ ASSOCIATED CONTENT

### Supporting Information

The Supporting Information is available free of charge on the ACS Publications website at DOI: [10.1021/acs.chemmater.6b02117](https://doi.org/10.1021/acs.chemmater.6b02117).

Additional crystallographic information for the ground-state structure (CIF)

Additional crystallographic information for the power-factor-optimized structure (CIF)

Table with additional information for the two structures; supplementary figures documenting the temperature, doping level, and carrier density dependence of Seebeck coefficient and power factor, the sensitivity of the band structure to the exchange–correlation functional, the structure and composition of the band edges, the number of ECIs as a function of cluster size, as well as the convergence of the SOFs with supercell size (PDF)

## ■ AUTHOR INFORMATION

### Corresponding Author

\*E-mail: [erhart@chalmers.se](mailto:erhart@chalmers.se).

### Notes

The authors declare no competing financial interest.

## ■ ACKNOWLEDGMENTS

We are grateful to Anders Palmqvist and Richard Hejl for many helpful discussions. This work was funded by the Knut and Alice Wallenberg Foundation and the Swedish Research Council, and supported by computer time allocations by the Swedish National Infrastructure for Computing at NSC (Linköping) and PDC (Stockholm).

## ■ REFERENCES

- (1) *Thermoelectrics Handbook: Macro to Nano*; Rowe, D., Ed.; CRC Press: Boca Raton, FL, 2005.
- (2) Snyder, G. J.; Toberer, E. S. Complex thermoelectric materials. *Nat. Mater.* **2008**, *7*, 105–114.
- (3) Heremans, J. P.; Wiendlocha, B.; Chamoire, A. M. Resonant levels in bulk thermoelectric semiconductors. *Energy Environ. Sci.* **2012**, *5*, 5510–5530.
- (4) Feldman, J. L.; Singh, D. J.; Kendziora, C.; Mandrus, D.; Sales, B. C. Lattice dynamics of filled skutterudites:  $\text{La}(\text{Fe},\text{Co})_4\text{Sb}_{12}$ . *Phys. Rev. B: Condens. Matter Mater. Phys.* **2003**, *68*, 094301.
- (5) Garg, J.; Bonini, N.; Kozinsky, B.; Marzari, N. Role of Disorder and Anharmonicity in the Thermal Conductivity of Silicon-Germanium Alloys: A First-Principles Study. *Phys. Rev. Lett.* **2011**, *106*, 045901.
- (6) Biswas, K.; He, J.; Zhang, Q.; Wang, G.; Uher, C.; Dravid, V. P.; Kanatzidis, M. G. Strained endotaxial nanostructures with high thermoelectric figure of merit. *Nat. Chem.* **2011**, *3*, 160–166.
- (7) Biswas, K.; He, J.; Blum, I. D.; Wu, C.-I.; Hogan, T. P.; Seidman, D. N.; Dravid, V. P.; Kanatzidis, M. G. High-performance bulk thermoelectrics with all-scale hierarchical architectures. *Nature* **2012**, *489*, 414–418.

- (8) Hicks, L. D.; Dresselhaus, M. S. Effect of quantum-well structures on the thermoelectric figure of merit. *Phys. Rev. B: Condens. Matter Mater. Phys.* **1993**, *47*, 12727–12731.
- (9) Heremans, J. P.; Dresselhaus, M. S.; Bell, L. E.; Morelli, D. T. When thermoelectrics reached the nanoscale. *Nat. Nanotechnol.* **2013**, *8*, 471–473.
- (10) Mahan, G. D.; Sofo, J. O. The best thermoelectric. *Proc. Natl. Acad. Sci. U. S. A.* **1996**, *93*, 7436–7439.
- (11) Heremans, J. P.; Thrush, C. M.; Morelli, D. T. Thermopower enhancement in PbTe with Pb precipitates. *J. Appl. Phys.* **2005**, *98*, 063703–063703–6.
- (12) Heremans, J. P.; Jovic, V.; Toberer, E. S.; Saramat, A.; Kurosaki, K.; Charoenphakdee, A.; Yamanaka, S.; Snyder, G. J. Enhancement of Thermoelectric Efficiency in PbTe by Distortion of the Electronic Density of States. *Science* **2008**, *321*, 554–557.
- (13) Faleev, S. V.; Léonard, F. Theory of enhancement of thermoelectric properties of materials with nanoinclusions. *Phys. Rev. B: Condens. Matter Mater. Phys.* **2008**, *77*, 214304.
- (14) Zhao, L.-D.; Dravid, V. P.; Kanatzidis, M. G. The panoramic approach to high performance thermoelectrics. *Energy Environ. Sci.* **2014**, *7*, 251–268.
- (15) Zhao, L.-D.; Tan, G.; Hao, S.; He, J.; Pei, Y.; Chi, H.; Wang, H.; Gong, S.; Xu, H.; Dravid, V. P.; Uher, C.; Snyder, G. J.; Wolverton, C.; Kanatzidis, M. G. Ultrahigh power factor and thermoelectric performance in hole-doped single-crystal SnSe. *Science* **2016**, *351*, 141–144.
- (16) Bilc, D. I.; Hautier, G.; Waroquiers, D.; Rignanese, G.-M.; Ghosez, P. Low-Dimensional Transport and Large Thermoelectric Power Factors in Bulk Semiconductors by Band Engineering of Highly Directional Electronic States. *Phys. Rev. Lett.* **2015**, *114*, 136601.
- (17) Bientien, A.; Madsen, G. K. H.; Johnsen, S.; Iversen, B. B. Experimental and theoretical investigations of strongly correlated FeSb<sub>2-x</sub>Sn<sub>x</sub>. *Phys. Rev. B: Condens. Matter Mater. Phys.* **2006**, *74*, 205105.
- (18) Bientien, A.; Johnsen, S.; Madsen, G. K. H.; Iversen, B. B.; Steglich, F. Colossal Seebeck coefficient in strongly correlated semiconductor FeSb<sub>2</sub>. *Europhysics Letters (EPL)* **2007**, *80*, 17008.
- (19) Rogl, P. *Thermoelectrics Handbook*; CRC Press: Boca Raton, FL, 2005; Chapter 32, pp 1–24.
- (20) Shevelkov, A. V.; Kovnir, K. In *Zintl Phases*; Fässler, T. F., Ed.; Structure and Bonding 139; Springer: Berlin Heidelberg, 2011; pp 97–142.
- (21) Blöchl, P. E. Projector augmented-wave method. *Phys. Rev. B: Condens. Matter Mater. Phys.* **1994**, *50*, 17953–17979.
- (22) Kresse, G.; Joubert, D. From ultrasoft pseudopotentials to the projector augmented-wave method. *Phys. Rev. B: Condens. Matter Mater. Phys.* **1999**, *59*, 1758–1775.
- (23) Kresse, G.; Hafner, J. Ab initio molecular dynamics for liquid metals. *Phys. Rev. B: Condens. Matter Mater. Phys.* **1993**, *47*, 558–561.
- (24) Kresse, G.; Furthmüller, J. Efficiency of ab-initio total energy calculations for metals and semiconductors using a plane-wave basis set. *Comput. Mater. Sci.* **1996**, *6*, 15–50.
- (25) Perdew, J. P.; Burke, K.; Ernzerhof, M. Generalized Gradient Approximation Made Simple. *Phys. Rev. Lett.* **1996**, *77*, 3865–3868; Erratum: Generalized Gradient Approximation Made Simple. *Phys. Rev. Lett.* **1997**, *78*, 1396.
- (26) Sanchez, J. M.; Ducastelle, F.; Gratias, D. Generalized cluster description of multicomponent systems. *Phys. A* **1984**, *128*, 334.
- (27) Sanchez, J. M. Cluster expansion and the configurational theory of alloys. *Phys. Rev. B: Condens. Matter Mater. Phys.* **2010**, *81*, 224202.
- (28) Candes, E.; Wakin, M. An Introduction To Compressive Sampling. *Signal Processing Magazine, IEEE* **2008**, *25*, 21–30.
- (29) Nelson, L. J.; Hart, G. L. W.; Zhou, F.; Ozolins, V. Compressive sensing as a new paradigm for model building. *Phys. Rev. B: Condens. Matter Mater. Phys.* **2013**, *87*, 035125.
- (30) Yin, W.; Osher, S.; Goldfarb, D.; Darbon, J. Bregman Iterative Algorithms for  $l_1$ -Minimization with Applications to Compressed Sensing. *SIAM Journal on Imaging Sciences* **2008**, *1*, 143–168.
- (31) Goldstein, T.; Osher, S. The Split Bregman Method for  $L_1$ -Regularized Problems. *SIAM Journal on Imaging Sciences* **2009**, *2*, 323–343.
- (32) Madsen, G. K.; Singh, D. J. BoltzTraP. A code for calculating band-structure dependent quantities. *Comput. Phys. Commun.* **2006**, *175*, 67–71.
- (33) Ziman, J. M. *Electrons and Phonons*; Clarendon Press: Oxford, 1960.
- (34) Blake, N. P.; Möllnitz, L.; Kresse, G.; Metiu, H. Why clathrates are good thermoelectrics: A theoretical study of Sr<sub>8</sub>Ga<sub>16</sub>Ge<sub>30</sub>. *J. Chem. Phys.* **1999**, *111*, 3133.
- (35) Blake, N. P.; Lattner, S.; Bryan, J. D.; Stucky, G. D.; Metiu, H. Band structures and thermoelectric properties of the clathrates Ba<sub>8</sub>Ga<sub>16</sub>Ge<sub>30</sub>, Sr<sub>8</sub>Ga<sub>16</sub>Ge<sub>30</sub>, Ba<sub>8</sub>Ga<sub>16</sub>Si<sub>30</sub>, and Ba<sub>8</sub>In<sub>16</sub>Sn<sub>30</sub>. *J. Chem. Phys.* **2001**, *115*, 8060.
- (36) Becke, A. D.; Johnson, E. R. A simple effective potential for exchange. *J. Chem. Phys.* **2006**, *124*, 221101.
- (37) Tran, F.; Blaha, P. Accurate Band Gaps of Semiconductors and Insulators with a Semilocal Exchange-Correlation Potential. *Phys. Rev. Lett.* **2009**, *102*, 226401.
- (38) Symmetry analyses were carried out using the spglib library written by Togo, A. See the following: <http://atztogo.github.io/spglib>.
- (39) Christensen, M.; Johnsen, S.; Iversen, B. B. Thermoelectric clathrates of type I. *Dalton Trans.* **2010**, *39*, 978–992.
- (40) Sales, B. C.; Chakoumakos, B. C.; Jin, R.; Thompson, J. R.; Mandrus, D. Structural, magnetic, thermal, and transport properties of X<sub>8</sub>Ga<sub>16</sub>Ge<sub>30</sub> (X = Eu, Sr, Ba) single crystals. *Phys. Rev. B: Condens. Matter Mater. Phys.* **2001**, *63*, 245113.
- (41) Bryan, J. D.; Blake, N. P.; Metiu, H.; Stucky, G. D.; Iversen, B. B.; Poulsen, R. D.; Bientien, A. Nonstoichiometry and chemical purity effects in thermoelectric Ba<sub>8</sub>Ga<sub>16</sub>Ge<sub>30</sub> clathrate. *J. Appl. Phys.* **2002**, *92*, 7281–7290.
- (42) Saramat, A.; Svensson, G.; Palmqvist, A. E. C.; Stiewe, C.; Mueller, E.; Platzeck, D.; Williams, S. G. K.; Rowe, D. M.; Bryan, J. D.; Stucky, G. D. Large thermoelectric figure of merit at high temperature in Czochralski-grown clathrate Ba<sub>8</sub>Ga<sub>16</sub>Ge<sub>30</sub>. *J. Appl. Phys.* **2006**, *99*, 023708.
- (43) Christensen, M.; Lock, N.; Overgaard, J.; Iversen, B. B. Crystal Structures of Thermoelectric n- and p-type Ba<sub>8</sub>Ga<sub>16</sub>Ge<sub>30</sub> Studied by Single Crystal, Multitemperature, Neutron Diffraction, Conventional X-ray Diffraction and Resonant Synchrotron X-ray Diffraction. *J. Am. Chem. Soc.* **2006**, *128*, 15657–15665.
- (44) Toberer, E. S.; Christensen, M.; Iversen, B. B.; Snyder, G. J. High temperature thermoelectric efficiency in Ba<sub>8</sub>Ga<sub>16</sub>Ge<sub>30</sub>. *Phys. Rev. B: Condens. Matter Mater. Phys.* **2008**, *77*, 075203.
- (45) Cederkrantz, D.; Saramat, A.; Snyder, G. J.; Palmqvist, A. E. C. Thermal stability and thermoelectric properties of p-type Ba<sub>8</sub>Ga<sub>16</sub>Ge<sub>30</sub> clathrates. *J. Appl. Phys.* **2009**, *106*, 074509.
- (46) Blake, N. P.; Bryan, J. D.; Lattner, S.; Möllnitz, L.; Stucky, G. D.; Metiu, H. Structure and stability of the clathrates Ba<sub>8</sub>Ga<sub>16</sub>Ge<sub>30</sub>, Sr<sub>8</sub>Ga<sub>16</sub>Ge<sub>30</sub>, Ba<sub>8</sub>Ga<sub>16</sub>Si<sub>30</sub>, and Ba<sub>8</sub>In<sub>16</sub>Sn<sub>30</sub>. *J. Chem. Phys.* **2001**, *114*, 10063–10074.
- (47) Madsen, G. K. H.; Schwarz, K.; Blaha, P.; Singh, D. J. Electronic structure and transport in type-I and type-VIII clathrates containing strontium, barium, and europium. *Phys. Rev. B: Condens. Matter Mater. Phys.* **2003**, *68*, 125212.
- (48) Madsen, G. K. H.; Santi, G. Anharmonic lattice dynamics in type-I clathrates from first-principles calculations. *Phys. Rev. B: Condens. Matter Mater. Phys.* **2005**, *72*, 220301.
- (49) Eisenmann, B.; Schäfer, H.; Zagler, R. Die Verbindungen A<sup>II</sup><sub>8</sub>B<sup>III</sup><sub>16</sub>B<sup>IV</sup><sub>30</sub> (A<sup>II</sup> = Sr, Ba; B<sup>III</sup> = Al, Ga; B<sup>IV</sup> = Si, Ge, Sn) und ihre Käfigstrukturen. *J. Less-Common Met.* **1986**, *118*, 43–55.
- (50) Christensen, M.; Iversen, B. B. Host Structure Engineering in Thermoelectric Clathrates. *Chem. Mater.* **2007**, *19*, 4896.
- (51) Ångqvist, M.; Erhart, P., *in preparation*.
- (52) Bertini, L.; et al. Thermoelectric performance of large single crystal clathrate Ba<sub>8</sub>Ga<sub>16</sub>Ge<sub>30</sub>. *International Conference on Thermoelectrics Proceedings* **2003**, 127.

- (53) Kuznetsov, V. L.; Kuznetsova, L. A.; Kaliazin, A. E.; Rowe, D. M. Preparation and thermoelectric properties of  $A_8B_{16}^{III}P_{30}^{IV}$  clathrate compounds. *J. Appl. Phys.* **2000**, *87*, 7871–7875.
- (54) Okamoto, N. L.; Kishida, K.; Tanaka, K.; Inui, H. Crystal structure and thermoelectric properties of type-I clathrate compounds in the Ba-Ga-Ge system. *J. Appl. Phys.* **2006**, *100*, 073504.
- (55) Okamoto, N. L.; Kishida, K.; Tanaka, K.; Inui, H. Effect of In additions on the thermoelectric properties of the type-I clathrate compound  $Ba_8Ga_{16}Ge_{30}$ . *J. Appl. Phys.* **2007**, *101*, 113525.
- (56) Note that in general, one also requires the electronic lifetimes for computing the Seebeck coefficient. This dependence, however, vanishes if the lifetime is assumed to be momentum- and mode-independent.
- (57) Yu, P. Y.; Cardona, M. *Fundamentals of Semiconductors*, 4th ed.; Springer: Berlin, 2001; Chapter 5.2.
- (58) Pfeifer, V.; Erhart, P.; Li, S.; Rachut, K.; Morasch, J.; Brötz, J.; Reckers, P.; Mayer, T.; Rühle, S.; Zaban, A.; Mora Seró, I.; Bisquert, J.; Jaegermann, W.; Klein, A. Energy Band Alignment between Anatase and Rutile  $TiO_2$ . *J. Phys. Chem. Lett.* **2013**, *4*, 4182–4187.
- (59) Note that while other defects, most notably vacancies, are present in real materials, their numbers are relatively smaller than the number of such antisite defects. For simplicity, they were therefore not considered in the present work.
- (60) Lany, S.; Zunger, A. Assessment of correction methods for the band-gap problem and for finite-size effects in supercell defect calculations: Case studies for ZnO and GaAs. *Phys. Rev. B: Condens. Matter Mater. Phys.* **2008**, *78*, 235104.
- (61) Erhart, P.; Åberg, D.; Lordi, V. Extrinsic point defects in aluminum antimonide. *Phys. Rev. B: Condens. Matter Mater. Phys.* **2010**, *81*, 195216.
- (62) Order parameters are commonly used to describe phase transitions, which is, however, not the objective here. Rather, we use the total energy merely as a convenient (single scalar) parameter to discriminate different structures by order.
- (63) Bhattacharya, S.; Madsen, G. K. H. High-throughput exploration of alloying as design strategy for thermoelectrics. *Phys. Rev. B: Condens. Matter Mater. Phys.* **2015**, *92*, 085205.
- (64) Usui, H.; Shibata, S.; Kuroki, K. Origin of coexisting large Seebeck coefficient and metallic conductivity in the electron doped  $SrTiO_3$  and  $KTaO_3$ . *Phys. Rev. B: Condens. Matter Mater. Phys.* **2010**, *81*, 205121.
- (65) Hao, S.; Shi, F.; Dravid, V. P.; Kanatzidis, M. G.; Wolverton, C. Computational Prediction of High Thermoelectric Performance in Hole Doped Layered GeSe. *Chem. Mater.* **2016**, *28*, 3218–3226.
- (66) Christensen, M.; Johnsen, S.; Söndergaard, M.; Overgaard, J.; Birkedal, H.; Iversen, B. B. Fast Preparation and Characterization of Quarternary Thermoelectric Clathrates. *Chem. Mater.* **2009**, *21*, 122–127.
- (67) Martin, J.; Erickson, S.; Nolas, G. S.; Alboni, P.; Tritt, T. M.; Yang, J. Structural and transport properties of  $Ba_8Ga_{16}Si_xGe_{30-x}$  clathrates. *J. Appl. Phys.* **2006**, *99*, 044903.
- (68) Martin, J.; Nolas, G. S.; Wang, H.; Yang, J. Thermoelectric properties of silicon-germanium type I clathrates. *J. Appl. Phys.* **2007**, *102*, 103719.
- (69) Deng, S.; Tang, X.; Li, P.; Zhang, Q. High temperature thermoelectric transport properties of p-type  $Ba_8Ga_{16}Al_xGe_{30-x}$  type-I clathrates with high performance. *J. Appl. Phys.* **2008**, *103*, 073503.
- (70) Voneshen, D. J.; et al. Suppression of thermal conductivity by rattling modes in thermoelectric sodium cobaltate. *Nat. Mater.* **2013**, *12*, 1028.
- (71) Barabash, S. V.; Ozolins, V.; Wolverton, C. First-Principles Theory of Competing Order Types, Phase Separation, and Phonon Spectra in Thermoelectric  $AgPb_mSbTe_{m+2}$  Alloys. *Phys. Rev. Lett.* **2008**, *101*, 155704.
- (72) Barabash, S. V.; Ozolins, V.; Wolverton, C. First-principles theory of the coherency strain, defect energetics, and solvus boundaries in the  $PbTe-AgSbTe_2$  system. *Phys. Rev. B: Condens. Matter Mater. Phys.* **2008**, *78*, 214109.
- (73) Schröder, T.; Rosenthal, T.; Giesbrecht, N.; Nentwig, M.; Maier, S.; Wang, H.; Snyder, G. J.; Oeckler, O. Nanostructures in Te/Sb/Ge/Ag (TAGS) Thermoelectric Materials Induced by Phase Transitions Associated with Vacancy Ordering. *Inorg. Chem.* **2014**, *53*, 7722–7729.
- (74) Shafeie, S.; Guo, S.; Hu, Q.; Fahlquist, H.; Erhart, P.; Palmqvist, A. High-entropy alloys as high-temperature thermoelectric materials. *J. Appl. Phys.* **2015**, *118*, 184905.
- (75) Kazem, N.; Zaikina, J. V.; Ohno, S.; Snyder, G. J.; Kauzlarich, S. M. Coinage-Metal-Stuffed  $Eu_9Cd_4Sb_9$ : Metallic Compounds with Anomalous Low Thermal Conductivities. *Chem. Mater.* **2015**, *27*, 7508–7519.



# Paper II

## **Understanding Chemical Ordering in Intermetallic Clathrates from Atomic Scale Simulations**

Mattias Ångqvist and Paul Erhart

Chemistry of Materials **29**, 7554 (2017)



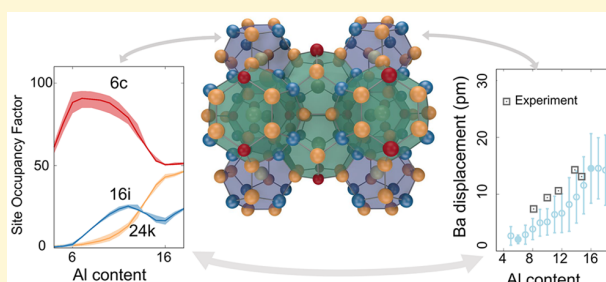
# Understanding Chemical Ordering in Intermetallic Clathrates from Atomic Scale Simulations

Mattias Ångqvist and Paul Erhart\*

Department of Physics, Chalmers University of Technology, S-412 96 Gothenburg, Sweden

Supporting Information

**ABSTRACT:** Intermetallic clathrates exhibit great variability with respect to elemental composition and distribution. While this provides a lot of flexibility for tuning properties, it also poses a challenge with regard to developing a comprehensive understanding of these systems. Here, we employ a combination of alloy cluster expansions and density functional theory calculations to exhaustively sample the compositional space with ab initio accuracy. We apply this methodology to study chemical ordering and related properties in the clathrate systems  $\text{Ba}_8\text{Ga}_x\text{Ge}_{46-x}$ ,  $\text{Ba}_8\text{Ga}_x\text{Si}_{46-x}$ ,  $\text{Ba}_8\text{Al}_x\text{Ge}_{46-x}$ , and  $\text{Ba}_8\text{Al}_x\text{Si}_{46-x}$  as a function of composition and temperature. We achieve very good agreement with the available experimental data for the site occupancy factors (SOFs) even for stoichiometries outside the composition range considered during construction of the cluster expansions. This validation enables us to reconcile the variations in the experimental data and explain nonmonotonic variations of the SOFs. In particular, we provide a rationale for the extreme SOF behavior with varying composition observed in Al-based clathrates. Furthermore, we quantify the effect of chemical ordering on both heat capacity and lattice expansion. Finally, we determine the effect of chemical disorder on the displacements of the guest species (Ba), which enables us to at least partially explain experimental observations of the nuclear density of Ba in different clathrates.



## INTRODUCTION

Clathrates represent a broad class of chemical substances with a defined lattice structure that can trap atomic or molecular species.<sup>1</sup> In particular, so-called intermetallic clathrates such as  $\text{Ba}_8\text{Ga}_{16}\text{Ge}_{30}$  or  $\text{Sr}_8\text{Ga}_{16}\text{Ge}_{30}$  have received a lot of attention due to their thermoelectric performance.<sup>2–6</sup> In these systems, alkaline and earth alkaline but also some rare earth atoms can occupy cages in the host structure, which is most commonly composed of elements from groups 13 and 14, although other constituents are possible.<sup>7</sup> These structures are realizations of the Zintl concept, i.e. the stoichiometric compounds are fully charge balanced, small gap semiconductors.<sup>2,7–9</sup> In practice, deviations from perfect stoichiometry are common, leading to intrinsically doped materials, a feature that can be beneficial, for example, for manipulating electrical transport properties.

Clathrates are classified according to their symmetry.<sup>2,7</sup> The majority of known intermetallic clathrates belong to type I and crystallize in space group  $Pm\bar{3}n$  (international tables of crystallography number 223).<sup>7</sup> Many of the compounds studied so far have the general composition  $\text{A}_8\text{B}_{16}\text{C}_{30}$ , where B and C form the host structure and occupy 6c, 16i, and 24k Wyckoff sites (Figure 1).<sup>9</sup> While it is most common for the guest species A to be cationic and B and C to be anions, there also exist so-called inverse (cationic) clathrates, in which the host–guest polarity is reversed.<sup>10</sup>

Experimental measurements of the site occupancy factors (SOFs) in many clathrates show that the elemental distribution

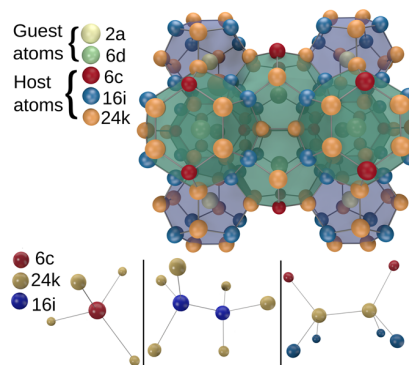


**Figure 1.** Crystal structure of type I clathrates. The guest species (Ba) occupies Wyckoff sites of type 2a and 6d, while the host species (Ga, Al, Ge, and Si) occupy Wyckoff sites of type 6c, 16i, and 24k. The configurations in the bottom row illustrate the environments for 6c, 16i, and 24k sites, respectively.

over the different crystallographic sites is not simply random.<sup>3</sup> For example, in the case of  $\text{Ba}_8\text{Ga}_{16}\text{Ge}_{30}$ , analysis of diffraction data yields Ga occupancies between 60 and 76% for the 6c site, which deviates considerably from the value of 35% correspond-

Received: June 28, 2017

Revised: August 3, 2017

Published: August 3, 2017

ing to the stoichiometry of the compound.<sup>11</sup> The experimental observations have been condensed into a set of rules for the SOFs,<sup>3</sup> partially based on calculations,<sup>12</sup> which have shown that bonds between trivalent species are energetically unfavorable.

The degree of chemical order has been found to vary not only between different compounds but also with stoichiometry with subsequent effects on the host atom structure.<sup>3,13,14</sup> By extension, chemical order has also been shown to impact the transport properties in these materials.<sup>15</sup> This suggests that a fine control of properties, in particular pertaining to transport, can be achieved by adjusting composition and stoichiometry. As a result of the complexity of navigating this multidimensional space as well as the experimental effort required to resolve order in the form of SOFs, this is, however, a very challenging task.<sup>16</sup>

Here, we therefore present a systematic computational study of chemical order and its effect on structure and thermodynamics in a series of ternary intermetallic clathrates with  $A = \text{Ba}$ ,  $B = \text{Al/Ga}$ , and  $C = \text{Si/Ge}$ . To this end, we employ a combination of first-principles calculations and lattice Hamiltonians (alloy cluster expansions) that enables us to sample both temperature and composition space with high accuracy. Where comparison is possible, our simulations closely match experimental data, which allows us to reveal the general behavior of these materials and effects that are not immediately apparent from the experimental data. We demonstrate that by varying the composition of these materials, the SOFs and thus the degree of chemical ordering can be altered dramatically. Furthermore, the chemical ordering is shown to systematically affect the average displacement of the guest species (Ba). This provides a key to understanding the origin of the nonspherical nuclear density of Ba observed experimentally in some clathrates.<sup>13</sup>

Recent computational work on inorganic clathrates has addressed ground state structures in  $\text{Ba}_8\text{Ga}_{16}\text{Ge}_{30}$  (ref 15) as well as  $\text{Ba}_8\text{Al}_x\text{Si}_{46-x}$  (ref 17) with an emphasis on electronic properties. In addition, the SOFs in stoichiometric  $\text{Ba}_8\text{Ga}_{16}\text{Ge}_{30}$  have been analyzed.<sup>15</sup> In the present work, we go beyond these studies by addressing the variation of the SOFs with composition and temperature and by conducting this investigation for a series of clathrates. Furthermore, we emphasize the coupling between order and thermodynamic properties as well as the connection to experiment.

The remainder of this paper is organized as follows. In the next section, we outline the construction of the alloy cluster expansions used in this work as well as the density functional theory calculations that were carried out to obtain input data. This is followed by the presentation of results for stoichiometric materials, in particular the temperature dependence of the site occupancy factors, which sets up an analysis of the contributions of chemical order on heat capacity and lattice expansion. We then extend the scope to nonstoichiometric compositions, which provide a comprehensive picture of ordering in these materials along with a rather extensive comparison with experimental data. Finally, we describe the coupling between chemical order and the off-center displacement of the guest species (Ba) atoms.

## METHODOLOGY

**Alloy Cluster Expansions.** Given a 16:30 ratio between group 13 and 14 elements, there are  $46!/30!/16! \approx 10^{12}$  different ways of distributing the atoms in the primitive unit cell. While this number is reduced by about one order of magnitude when taking into account

symmetry, the remaining space is still extremely large and cannot be sufficiently sampled by density functional theory (DFT) calculations alone. Here, we therefore resort to the alloy cluster expansion (CE) technique which allows at least in principle an exact mapping of ordering energetics onto an effective lattice Hamiltonian.<sup>18,19</sup> The energy of the system is expressed in the form of a generalized Ising model, which not only includes pair (second order) terms but also higher order “clusters”, including, e.g., triplets (involving three sites) or quadruplets (four sites). Using a CE, the energy can be formally written as

$$E(\sigma) = E_0 + \sum_{\alpha} m_{\alpha} J_{\alpha} \bar{\Pi}_{\alpha}(\sigma) \quad (1)$$

Here,  $J_{\alpha}$  are the so-called effective cluster interactions (ECIs) that are associated with the symmetry inequivalent clusters  $\alpha$ , which occur with multiplicity  $m_{\alpha}$ . The occupation of different sites is represented by the “spin” vector  $\sigma$ , each value of which indicates the occupation of a site in the system (here,  $-1$  and  $+1$  for group 13 and 14 elements, respectively). Finally,  $\bar{\Pi}_{\alpha}$  is a symmetrized product over the spin variables which, approximately speaking, represents the average occupation (decoration) of cluster  $\alpha$  by the species considered in the CE. It is important to emphasize that while the CE is itself restricted to a rigid lattice, atomic relaxation and strain contributions to the energy are effectively incorporated in the ECIs if the CE is trained using relaxed structures. Furthermore, we note that the expansion eq 1 is not restricted to the energy but can be extended to other properties, including, e.g., electronic properties<sup>15</sup> or, as in the present work, the lattice parameter.

To construct the CE, i.e. obtain the set of ECIs representing the energy landscape for a certain material, we employed compressive sampling<sup>20</sup> in conjunction with the split-Bregman algorithm,<sup>21,22</sup> which has been shown to be very efficient for constructing physically sound and very accurate CEs.<sup>23</sup> To this end, we used our in-house integrated cluster expansion toolkit (ICET). Recently, we successfully employed the same approach to describe chemical ordering and its effect on transport properties in stoichiometric  $\text{Ba}_8\text{Ga}_{16}\text{Ge}_{30}$ .<sup>15</sup>

For each of the four elemental combinations, we constructed a CE based on a set of 290 structures for  $\text{Ba}_8\text{Ga}_x\text{Ge}_{46-x}$  and 240 for the remaining three alloys, which were relaxed and characterized using DFT calculations. For  $\text{Ba}_8\text{Ga}_x\text{Ge}_{46-x}$  the set included 101, 163, 21, and 6 structures with stoichiometries of 16:30, 15:31, 14:32, and 13:33, respectively. For the remaining three materials, the set comprised 171, 42, 21, and 6 structures with stoichiometries of 16:30, 15:31, 14:32, and 13:33, respectively.

The cluster space considered during the optimization of the ECIs included 90 clusters up to third order. The  $\mu$  parameter, which controls the sparsity of the CS solution, was set to 0.001, while the  $\lambda$  parameter that enters in the split-Bregman algorithm was set to 100 (see ref 23 for a discussion of these parameters). These values were chosen based on a preliminary screening study. This specific choice has, however, only a minor impact on the final results and mostly affects the efficiency of the optimization procedure.

We note that experimentally vacancies are known to be present in notable concentrations, especially for samples that are very far from the stoichiometric composition, e.g., for  $\text{Ba}_8\text{Ga}_x\text{Ge}_{46-x}$  with  $x = 3.5-5$ .<sup>24</sup> Here, we do not include this effect, whence our results for these extreme compositions should be regarded as idealized approximations of the real behavior.

The CEs were sampled using Monte Carlo (MC) simulations. Simulated annealing runs were carried out by initializing a system composed of one unit cell at 1200 K, after which the temperature was gradually reduced at a rate of at most 25 K/20 000 MC cycles.<sup>25</sup> At each temperature, the system was equilibrated for 2000 MC cycles followed by 30 000 MC cycles, during which statistics were gathered. In addition, simulations were carried out at constant temperature and variable composition using the variance constrained semigrand canonical ensemble.<sup>26</sup>

**Electronic Structure Calculations.** The parametrization of the CE Hamiltonian described in the previous section requires total energies for a set of representative structures. To this end, DFT

calculations were carried out using the projector augmented wave method<sup>27,28</sup> as implemented in the Vienna ab initio simulation package.<sup>29,30</sup> The generalized gradient approximation as parametrized in ref 31 was employed to represent the exchange-correlation functional. The Brillouin zone was sampled using a  $\Gamma$ -centered  $3 \times 3 \times 3$   $k$ -point mesh, and the plane wave basis set was expanded up to cutoff energies of 319 eV ( $\text{Ba}_8\text{Al}_x\text{Si}_{46-x}$ ,  $\text{Ba}_8\text{Ga}_x\text{Si}_{46-x}$ ), 312 eV ( $\text{Ba}_8\text{Al}_x\text{Ge}_{46-x}$ ), and 243 eV ( $\text{Ba}_8\text{Ga}_x\text{Ge}_{46-x}$ ).

Structures comprising a single unit cell of 54 atoms were created by randomly assigning Ga and Ge atoms to the 6c, 16i, and 24k Wyckoff sites of the host structure. For each structure, both the ionic positions and the cell metric were fully relaxed until atomic forces were less than 10 meV/Å and absolute stresses were below 0.1 kbar.

We note that more refined algorithms are available for generating input structures.<sup>23,32</sup> They are, however, difficult if not prohibitive to apply in the present context due to the very large number of possible chemical distributions that can be realized already for the primitive unit cell. The validation presented below demonstrates though that the approach taken here succeeds in providing predictive as well as accurate CEs.

For the ground state structures obtained by simulated annealing (see below), we evaluated the thermal lattice expansion and heat capacity at the level of the quasi-harmonic approximation using the PHONOPY package.<sup>33</sup> To this end, we conducted additional calculations at several volumes spanning a range of approximately  $0.85a_0$  to  $1.05a_0$ , where  $a_0$  is the calculated lattice parameter.

## RESULTS AND DISCUSSION

**Validation of Cluster Expansions.** The performance of each CE was evaluated using the leave-one-out cross-validation score, and the final CEs achieved very low scores of 0.6, 0.8, 0.8, and 1.2 meV/atom for  $\text{Ba}_8\text{Ga}_x\text{Ge}_{46-x}$ ,  $\text{Ba}_8\text{Al}_x\text{Ge}_{46-x}$ ,  $\text{Ba}_8\text{Ga}_x\text{Si}_{46-x}$  and  $\text{Ba}_8\text{Al}_x\text{Si}_{46-x}$  respectively. This accuracy is not restricted to stoichiometric compositions but applies to a wide concentration range (Figure 2).

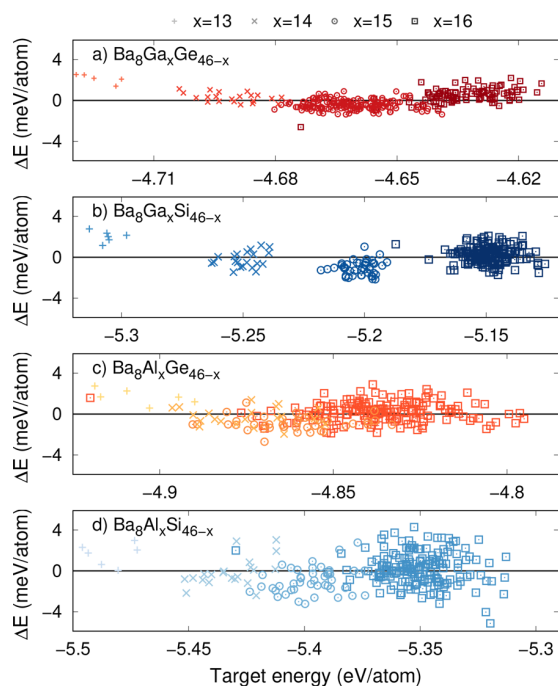


**Figure 2.** Performance of cluster expansions constructed in this work. Prediction errors for (a)  $\text{Ba}_8\text{Ga}_x\text{Ge}_{46-x}$ , (b)  $\text{Ba}_8\text{Ga}_x\text{Si}_{46-x}$ , (c)  $\text{Ba}_8\text{Al}_x\text{Ge}_{46-x}$  and (d)  $\text{Ba}_8\text{Al}_x\text{Si}_{46-x}$  as a function of the DFT target energy.

The ECIs decrease in magnitude by approximately one order of magnitude for each increase in order (Figure 3). The singlet

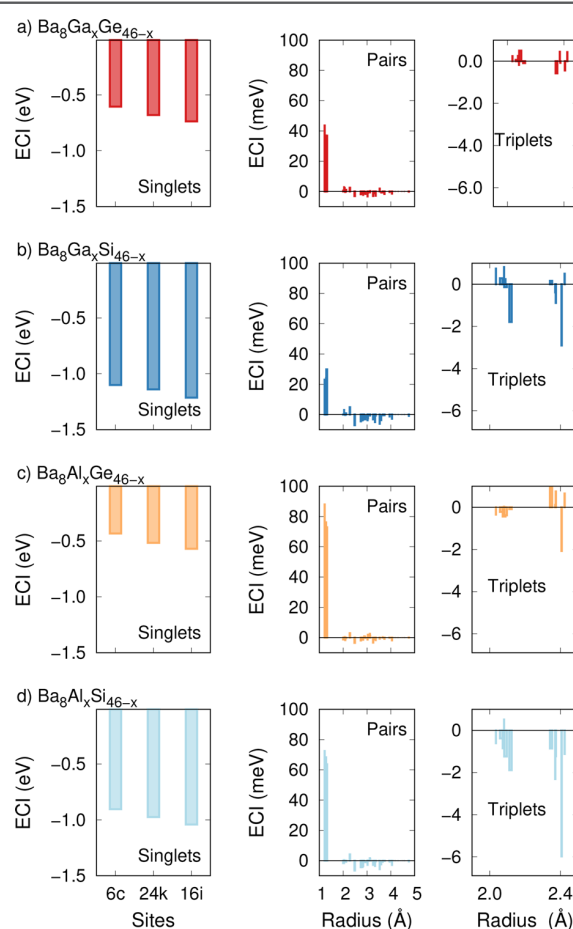


**Figure 3.** Effective cluster interactions as a function of cluster radius for (a)  $\text{Ba}_8\text{Ga}_x\text{Ge}_{46-x}$ , (b)  $\text{Ba}_8\text{Ga}_x\text{Si}_{46-x}$ , (c)  $\text{Ba}_8\text{Al}_x\text{Ge}_{46-x}$  and (d)  $\text{Ba}_8\text{Al}_x\text{Si}_{46-x}$  as a function of the radius.

interactions exhibit a clear hierarchy where  $6c > 24k > 16i$ , which implies that in the absence of group 13/group 13 interactions, the occupation of 6c sites is energetically the most favorable.

One can furthermore observe that the pair interactions are considerably larger if the clathrate contains Al compared to Ga. As is discussed below, this causes an inversion of the ordering of the occupation factors for 24k and 16i sites in  $\text{Ba}_8\text{Al}_x\text{Si}_{46-x}$  and  $\text{Ba}_8\text{Al}_x\text{Ge}_{46-x}$  compared to the Ga-containing variants. Beyond-nearest-neighbor pair as well as triplet terms are generally much smaller and can be even set to zero without a big loss of accuracy, in agreement with similar observations for  $\text{Ba}_8\text{Al}_x\text{Si}_{46-x}$  and  $\text{Sr}_8\text{Al}_x\text{Si}_{46-x}$ .<sup>17</sup>

The ordering of the singlet ECIs is in line with the established rule that at least for Ga-based clathrates, the 16i site is preferentially occupied by group 14 species.<sup>12</sup> As will be shown below, this rule alone is, however, insufficient to explain the variation of the SOFs in nonstoichiometric Al-based clathrates because pair interactions play an important role.

Using simulated annealing, we determined the ground state structures at stoichiometric composition, which were subsequently relaxed at the DFT level. For all four materials, the CEs predicted the DFT energy of the ground state structure to

within 2 meV/atom. In all cases, the chemical distribution corresponds to the one reported previously for  $\text{Ba}_8\text{Ga}_{16}\text{Ge}_{30}$ <sup>15</sup> and the ground state structures belong to space group R3 (International Tables of Crystallography no. 146) and are provided in the [Supporting Information](#).

**Stoichiometric Compositions. Site Occupancy Factors.** Following the successful validation of the CEs, further MC simulations were carried out to gather statistics concerning the elemental distribution and in particular the site occupancy factors (SOFs) as a function of both composition and temperature.

We first consider the behavior of the stoichiometric systems (group 13:group 14 = 16:30). The materials exhibit some qualitative similarities in the temperature dependence of the SOFs ([Figure 4](#)). At high temperatures (1000–1200 K), the

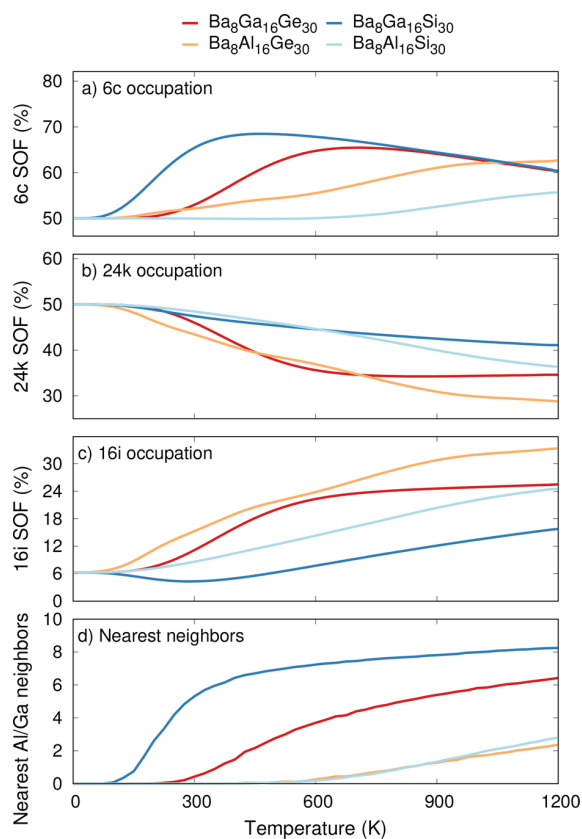


**Figure 4.** Site occupancy factors of stoichiometric intermetallic clathrates as a function of temperature for Wyckoff sites (a) 6c, (b) 24k, and (c) 16i. (d) Fraction of Al–Al or Ga–Ga nearest neighbors.

SOF for 6c sites ranges from 55 to 65%, while for 16i sites, it falls between 20 and 30%. For 24k sites, values from 30 to 40% are obtained. The statistical limit of 16:30 = 35% is only reached for all sites in the very high temperature limit (>20 000 K).

For all four systems, the SOFs for 6c and 24k sites approach 50% at low temperatures, whereas the 16i SOF converges to 6.25%. Ultimately, this leads to the ground state structure described above.<sup>15</sup> It is interesting to note that the SOFs for this structure coincide with those of the lowest energy structure described in [ref 12](#), which was obtained by simultaneously minimizing the 16i SOF and the number of Ga–Ga bonds.

While the four materials considered here exhibit very similar behavior in the low and high-temperature limits, there are clear differences in the intermediate temperature region. Most notably, we obtain higher 6c SOFs for the Ga-based clathrates, which can be traced back to the ECIs according to which pair interactions are weaker than in the case of the Al-based clathrates. As a result, the Ga-based clathrates can occupy more of the energetically favorable 6c sites, tolerating the cost of relatively more Ga–Ga nearest neighbors.

**Heat Capacity.** The variation of chemical order with temperature is driven by the balance between energy and entropy. Hence, there should also be a configurational energy term that contributes to the heat capacity of the material. The latter can be obtained from the temperature dependence of the average energy  $\langle E \rangle$  recorded during MC sampling or, more directly, the variance of the energy  $\langle \Delta E^2 \rangle$  according to

$$\Delta c^{\text{chem}} = \frac{\langle \Delta E^2 \rangle}{k_B T^2} \quad (2)$$

According to the MC simulations, at the stoichiometric composition, the contribution to the heat capacity due to chemical order can reach values of up to 15  $k_B$ /unit cell in the case of  $\text{Ba}_8\text{Ga}_{16}\text{Ge}_{30}$  and  $\text{Ba}_8\text{Al}_{16}\text{Si}_{30}$  and of about 10  $k_B$ /unit cell for  $\text{Ba}_8\text{Ga}_{16}\text{Si}_{30}$  and  $\text{Ba}_8\text{Al}_{16}\text{Ge}_{30}$  ([Figure 5a](#)). By comparison with the temperature variation of the SOFs ([Figure 4](#)), it is apparent that  $\Delta c^{\text{chem}}$  becomes maximal approximately in those temperature regions, at which the SOFs undergo the largest change. This effect is about 1 order of magnitude smaller than the vibrational contribution to the (isobaric) heat capacity. The latter can be obtained from calculations of the phonon density of states in the quasi-harmonic approximation, which for the ground state structures yields values between 1200 ( $\text{Ba}_8\text{Al}_{16}\text{Si}_{30}$ ) to 1400 J/(mol K) ( $\text{Ba}_8\text{Ga}_{16}\text{Ge}_{30}$ ) 144 to 168  $k_B$ /unit cell in the temperature range between 300 and 900 K and thus above the Debye temperature, which is commonly around 300 K.

In the experimental literature, several studies have reported anomalies in the temperature dependence of the heat capacity of clathrates.<sup>34,35</sup> In particular, May et al. observed an abrupt increase in the heat capacity of nearly stoichiometric  $\text{Ba}_8\text{Ga}_{16}\text{Ge}_{30}$  at about 650 K by 0.03 J/mol/g = 15  $k_B$ /unit cell, which is comparable in magnitude to the contribution of chemical order predicted above ([Figure 5a](#)). Furthermore, the temperature of 650 K, at which the feature is observed, falls in the temperature range of 600–700 K, in which one can expect the chemical order to be frozen in (see below). This suggests that the observed jump in heat capacity could be at least partly caused by chemical ordering. We note that this feature in the heat capacity is not observed in all studies. This could be caused by different heating/cooling rates as well as the sensitivity of  $\Delta c^{\text{chem}}$  to composition (see [Figure S3](#) in the [Supporting Information](#)).

**Chemical Expansion.** From the configurations, for which DFT calculations have been conducted, it is apparent that the degree of chemical order also affects the lattice parameter. To provide a more quantitative description of this coupling, additional CEs for the cell volume were constructed and sampled in parallel during the simulated annealing simulations described above (details pertaining to the construction of these CEs can be found in the [Supporting Information](#)).

The results demonstrate that chemical disordering can change the lattice parameter by as much as 0.08 Å over the

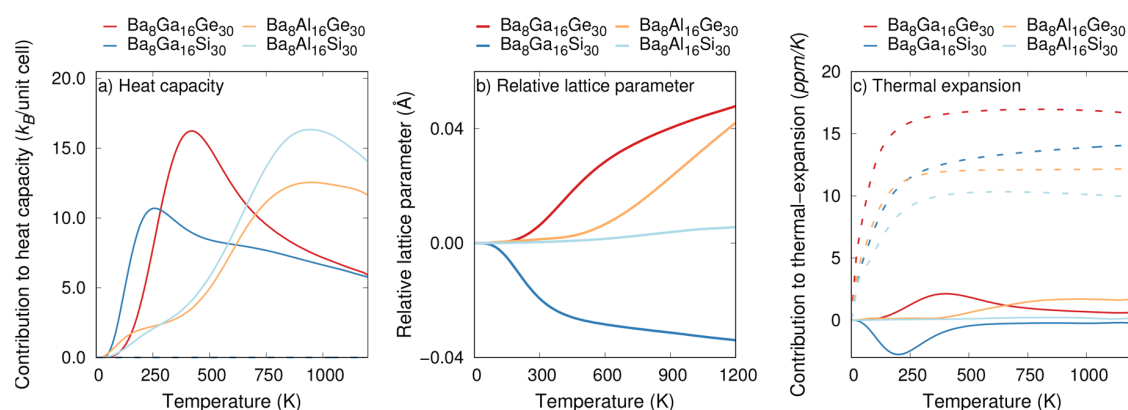


**Figure 5.** Contributions due to chemical ordering to (a) heat capacity and (b) lattice parameter. (c) Contribution to thermal expansion due to lattice vibrations (dotted lines) and chemical ordering (solid lines).

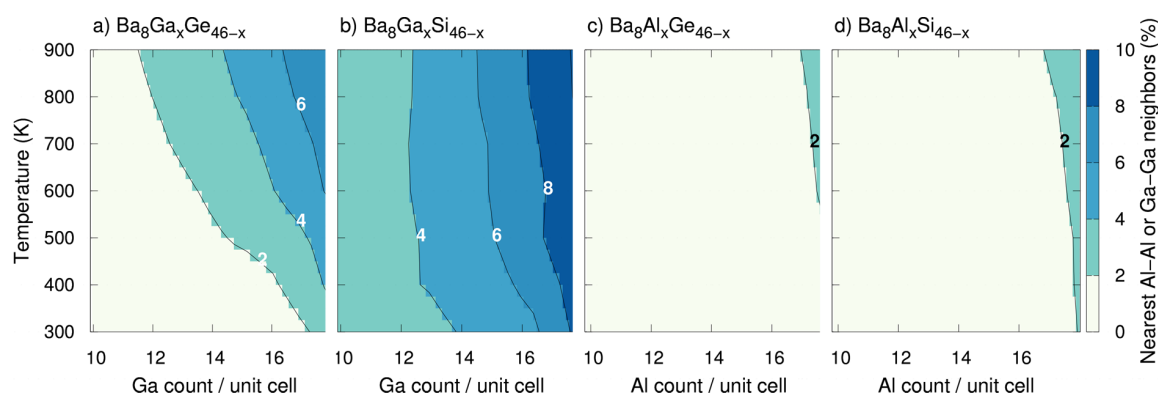


**Figure 6.** Fraction of Al–Al or Ga–Ga nearest neighbors for (a)  $\text{Ba}_8\text{Ga}_x\text{Ge}_{46-x}$  (b)  $\text{Ba}_8\text{Ga}_x\text{Si}_{46-x}$  (c)  $\text{Ba}_8\text{Al}_x\text{Ge}_{46-x}$  and (d)  $\text{Ba}_8\text{Al}_x\text{Si}_{46-x}$ .

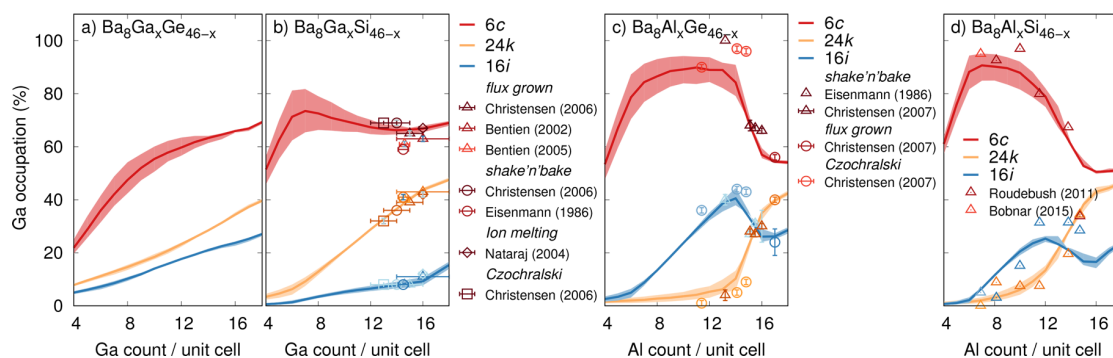


**Figure 7.** Site occupancy factors in intermetallic clathrates as a function of composition for Wyckoff sites 6c (red), 16i (blue), and 24k (orange). Solid lines show simulation results obtained at 700 K whereas the shaded regions indicate a variation by  $\pm 100$  K.

temperature range from 0 to 1200 K, both in the negative ( $\text{Ba}_8\text{Ga}_{16}\text{Si}_{30}$  in Figure 5b) and positive direction ( $\text{Ba}_8\text{Al}_{16}\text{Ge}_{30}$  and  $\text{Ba}_8\text{Ga}_{16}\text{Ge}_{30}$  in Figure 5b). The effect is only negligible in the case of  $\text{Ba}_8\text{Al}_{16}\text{Si}_{30}$ . The variation of the lattice parameter with order translates to a chemical contribution  $\alpha_l^{\text{chem}}$  to the linear thermal expansion coefficient. It is largest in the case of  $\text{Ba}_8\text{Al}_{16}\text{Ge}_{30}$ , where it reaches  $1.6 \times 10^{-6}/\text{K}$  (Figure 5b) to be compared with a thermal expansion coefficient due to phonons obtained in the quasi-harmonic approximation of  $\alpha_l^{\text{phonon}} = 17 \times 10^{-6}/\text{K}$  (Figure 5c). The chemical expansion in these systems is thus typically at least 1 order of magnitude smaller than the phononic contribution.

**Nonstoichiometric Compositions.** One can readily synthesize nonstoichiometric intermetallic clathrates with compositions that deviate substantially from the ideal 16:30 ratio between trivalent and tetravalent ions.<sup>3,14</sup> Nonstoichiometry is often desirable because it provides a convenient means for tuning the charge carrier concentration in these small band gap systems by (intrinsic) doping. As will be shown in the following, there is an intimate and nonmonotonic coupling between the SOFs and the composition that translates into distinct changes in the structure of the cages (see below).

All four systems were sampled at several different temperatures. In addition, we conducted simulated annealing runs in

which the temperature was reduced to zero Kelvin to obtain purely energy optimized ground state structures.

**Site Occupancy Factors.** For the Ga based clathrate systems, the SOFs show a relatively smooth variation with composition. The SOFs increase in the order 16i to 24k to 6c, which corresponds to the energetic ordering of the singlet ECIs (Figures 3a and b). At the same time the number of Ga–Ga neighbors decreases continuously with decreasing Ga content (Figures 6a and b). This observation correlates with Ga–Ga repulsion being weaker than Al–Al repulsion, as evident from the pair ECIs (Figure 3).

A compilation of experimental SOFs from various sources<sup>9,36–39</sup> reveals that the calculated SOFs for  $\text{Ba}_8\text{Ga}_x\text{Si}_{46-x}$  are in excellent agreement with these data and in fact clearly reveal the chemical trends in this material.

In contrast to the Ga based materials, in the case of the Al containing systems, we observe a very pronounced, non-monotonic dependence of the SOFs on Al content (Figures 7c and d), which is in very good agreement with available experimental data.<sup>9,13,14,40</sup>

The composition dependence exhibits two distinct regions that meet at  $x \approx 14$ , which becomes even more apparent in the zero temperature limit (Figure 8). For  $x > 14$ , the SOFs follow

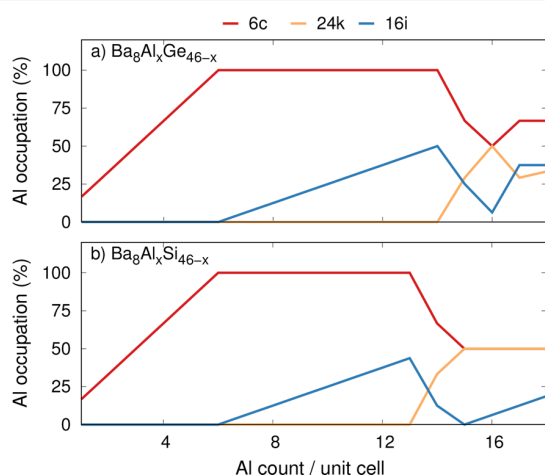


**Figure 8.** Site occupancy factors for the ground states in (a)  $\text{Ba}_8\text{Al}_x\text{Si}_{46-x}$  and (b)  $\text{Ba}_8\text{Al}_x\text{Ge}_{46-x}$  as a function of composition for Wyckoff sites 6c (red), 16i (blue), and 24k (orange).

the same order as in the case of the Ga based clathrates, whereas the 24k and 16i SOFs are reversed for  $x \lesssim 14$ . This behavior can be rationalized by invoking not only the singlet ECIs but also the pair interactions (Figure 3).

First, we note that for compositions below  $x = 14$  (but not above), it is possible to accommodate all Al atoms on 6c and 16i sites without the need to occupy 24k sites. Because there are no bonds between 16i and 6c sites (Figure 1), this strategy effectively avoids nearest neighbor Al–Al pairs. Because the pair ECIs for the Al systems are larger by a factor of 2–5 compared to the Ga containing clathrates, avoiding Al–Al neighbors is energetically more important, and 16i sites become effectively favored over 24k sites. The strength of the Al–Al repulsion is also apparent in the much lower fraction of Al–Al neighbors, which is below 2% for practically the entire temperature–composition plane (Figure 6c and d).

The effect of the pair ECIs is even notable when comparing  $\text{Ba}_8\text{Al}_x\text{Ge}_{46-x}$  and  $\text{Ba}_8\text{Al}_x\text{Si}_{46-x}$  as in the latter case the peak in

the 16i SOF around  $x = 14$  is less pronounced (Figures 7c and d), which is in line with the lower pair ECIs of  $\text{Ba}_8\text{Al}_x\text{Si}_{46-x}$  (Figures 3c and d).

Similar features as the ones described above were already observed in the experimental data for both  $\text{Ba}_8\text{Al}_x\text{Si}_{46-x}$  and  $\text{Ba}_8\text{Al}_x\text{Ge}_{46-x}$ , which prompted the formulation of a set of rules for the SOFs.<sup>3</sup> The present analysis provides a rigorous basis for these rules and demonstrates how the underlying interaction strengths can be obtained quantitatively, which allows one to extend the approach more easily to a larger class of clathrates. We note that the variation of the SOFs at zero temperature described here (Figure 8) was also observed in a recent simulation study that focused on the ground state structures in  $\text{Ba}_8\text{Al}_x\text{Si}_{46-x}$  and  $\text{Sr}_8\text{Al}_x\text{Si}_{46-x}$ .<sup>17</sup>

The temperature dependence of the SOFs predicted by our simulations represents the behavior of materials that have achieved thermodynamic equilibrium with regard to the distribution of different chemical species over the available lattice sites. Experimentally, equilibrium can be expected to be achieved only above a certain minimum temperature, corresponding to the onset of mobility for intrinsic defects that can mediate atomic rearrangement.<sup>41</sup> This temperature range can thus be estimated by comparison of calculated and experimental SOFs. More specifically, it should correspond to the temperature below which the calculated SOFs start to deviate from the experimental data. This yields an estimate for the temperature, at which chemical order is frozen, between 600 and 700 K.

**Off-Center Displacements of Ba Atoms.** Experimental measurements of the nuclear density have shown a non-spherical distribution of the Ba atoms around the 6d sites of the type-I clathrate structure in several of the materials considered here.<sup>3,11,13,14,40</sup> This effect has also been included in Rietveld refinements of diffraction data by assigning six of the Ba atoms in the structure to either 24k or 24j Wyckoff sites with a partial occupancy of 25%, corresponding to a fourfold splitting of the 6d site. To assess whether this behavior can at least be partially explained in terms of the variation of chemical composition of the cages with Al/Ga content, we extracted representative configurations from MC simulations at 700 K and relaxed them using DFT calculations. We then mapped each configuration onto the respective ideal crystal structure scaled to the lattice parameter corresponding to the composition (Figure S2 in the Supporting Information) and computed the displacement of the Ba atom from the ideal 6d site.

In all four materials near the stoichiometric composition, the Ba atom is displaced by 15–19 pm from the ideal 6d site (Figure 9). These numbers are in good agreement with the radius of the ring-like nuclear density extracted experimentally.<sup>3,13</sup> Unfortunately, our statistics are insufficient to extract the full three-dimensional nuclear density. We can, however, obtain the radial distribution, which exhibits a shape that is consistent with a ring-like nuclear density (shown exemplarily for  $\text{Ba}_8\text{Al}_x\text{Ge}_{46-x}$  in Figure 9e).

While in all four materials the off-center displacement (OCD) is maximal for  $x \approx 16$ , they exhibit differences with respect to its variation with composition. For  $\text{Ba}_8\text{Ga}_x\text{Ge}_{46-x}$  and  $\text{Ba}_8\text{Al}_x\text{Ge}_{46-x}$  the OCD falls off only slowly with Ga/Al content for  $8 \leq x \leq 15$  with an average value of about 10 to 13 pm. In contrast, for the Si-containing clathrates, the OCD decreases strongly and monotonically with composition, reaching minimal values of about 2 pm at  $x \approx 6$ .

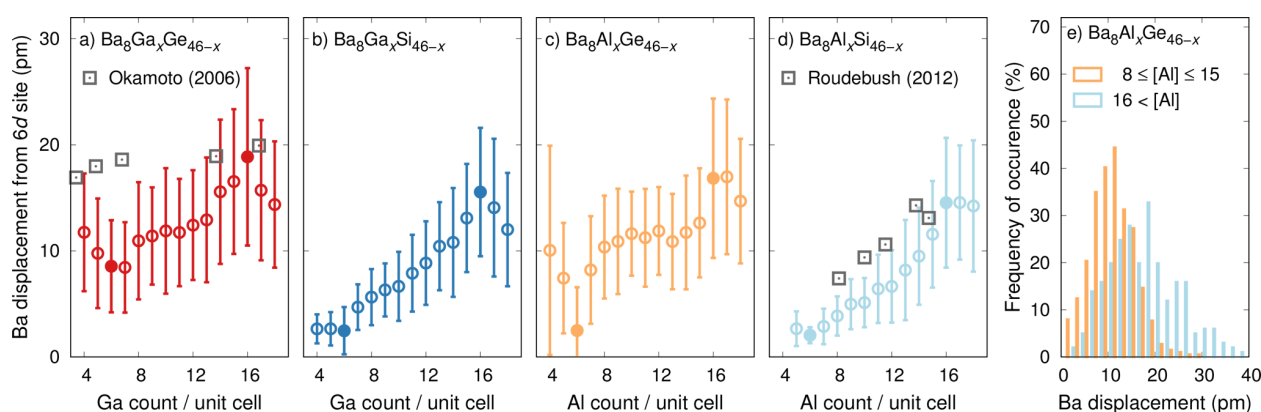


**Figure 9.** Off-center displacements of Ba atoms on 6d sites as a function of composition for (a)  $\text{Ba}_8\text{Ga}_x\text{Ge}_{46-x}$  (b)  $\text{Ba}_8\text{Ga}_x\text{Si}_{46-x}$  (c)  $\text{Ba}_8\text{Al}_x\text{Ge}_{46-x}$  and (d)  $\text{Ba}_8\text{Al}_x\text{Si}_{46-x}$  as well as the distribution of displacements for (e)  $\text{Ba}_8\text{Al}_x\text{Ge}_{46-x}$ . Experimental data for the atomic displacement parameters in  $\text{Ba}_8\text{Ga}_x\text{Ge}_{46-x}$  and  $\text{Ba}_8\text{Al}_x\text{Si}_{46-x}$  have been taken from refs 24 and 14, respectively.

The trends in the OCDs correlate with the variation of the lattice parameter with composition (Figure S2 in the Supporting Information). While in the case of  $\text{Ba}_8\text{Ga}_x\text{Si}_{46-x}$  and  $\text{Ba}_8\text{Al}_x\text{Si}_{46-x}$  the lattice parameter increases with Al/Ga content, a weaker correlation with the opposite sign is observed for  $\text{Ba}_8\text{Ga}_x\text{Ge}_{46-x}$  and  $\text{Ba}_8\text{Al}_x\text{Ge}_{46-x}$ . The size of the cages in which Ba resides scales with the average atomic volume of the structure and thus the lattice constant (Figure S5 in the Supporting Information). The strong reduction in the OCD in the former two materials can therefore be related to a general decrease in the cage size.

It is noteworthy that the OCDs calculated here in the zero temperature limit, compare well both in trend and magnitude with experimental data for the atomic displacement parameter (ADP) of the Ba 6d site in  $\text{Ba}_8\text{Ga}_x\text{Ge}_{46-x}$  and  $\text{Ba}_8\text{Al}_x\text{Si}_{46-x}$ .<sup>14,24</sup> Because the ADPs indicate the magnitude of thermal displacements as obtained from Rietveld refinements, a direct comparison with the OCDs is, however, not meaningful. Nonetheless, the underlying structural features, including cage size and Al content of the cages, are the same, which helps to explain the correlation of the parameters.

**Comment on Nuclear Densities in  $\text{Ba}_8\text{Al}_x\text{Ge}_{46-x}$ .** The symmetry of the Ba site in  $\text{Ba}_8\text{Al}_x\text{Ge}_{46-x}$  appears to be sensitive to the synthesis route.<sup>13</sup> While for a “shake-and-bake” sample the Ba 6d site has been found to split fourfold at low temperatures, yielding 24k or 24j sites, the 6d site symmetry was maintained in the case of a Czochralski grown crystal. This difference between the samples is also apparent from the nuclear densities. It has furthermore been found that the shake-and-bake sample had an Al content of 15.5 and a 6c SOF of 67%, whereas the Czochralski grown crystals gave 14.8 and 96%, respectively.<sup>3</sup> These two points fall in the composition region for which our simulations show a relatively sharp transition in the SOFs (Figure 7). The analysis of the Ba displacements shows that this transition also leads to a rather abrupt change in the OCDs, in accordance with the experimental trend.

## CONCLUSIONS

In the present work, we combined density functional theory calculations with alloy cluster expansions to study chemical ordering in four prototypical clathrates ( $\text{Ba}_8\text{Ga}_x\text{Ge}_{46-x}$ ,  $\text{Ba}_8\text{Ga}_x\text{Si}_{46-x}$ ,  $\text{Ba}_8\text{Al}_x\text{Ge}_{46-x}$  and  $\text{Ba}_8\text{Al}_x\text{Si}_{46-x}$ ). The energy landscape was sampled as a function of temperature and

composition using Monte Carlo simulations from which we extracted site occupancy factors, heat capacities, and lattice constants.

The predicted SOFs are in very good agreement with experimental data, where comparison is possible (Figure 7). More importantly, the simulations clarify the experimental observations and reveal trends across materials. For Ga-based materials as well as Al-based materials with an Al content above  $x = 14$ , the different sites are occupied in the sequence  $6c - 24k - 16i$ . If the Al content drops, however, to  $x \approx 14$  or below, 16i sites become more preferable than 24k sites. This behavior can be explained in terms of the ECI parameters of the underlying CEs. The latter show that Al–Al repulsion is much stronger than Ga–Ga repulsion (Figure 3), which drives the redistribution from 24k to 16i sites with decreasing Al content.

Chemical ordering is shown to impact various properties, including the heat capacity (Figures 5a and Figure S3 of the Supporting Information) and the lattice parameter (Figures 5b and c) and Figure S2 of the Supporting Information). Specifically in the former case, the present results suggest that the jump in the heat capacity observed in some experimental measurements can be related to the entropic contribution associated with chemical (dis)order.

For convenience, let us summarize the essential chemical trends that have emerged from the comparison of four different clathrate systems. The singlet ECIs, which determine the energy cost for occupying different Wyckoff sites, follow the order  $6c > 24k > 16i$  in all materials considered here. The pair interaction between group 13 species are, however, notably more repulsive for Al–Al than for Ga–Ga (Figure 3). As a result, Al–Al bonds are strongly suppressed at all temperatures and compositions, whereas the Ga-based materials are more tolerant to the formation of Ga–Ga bonds (Figure 6). The repulsive Al–Al interaction furthermore causes an inversion in the ordering of the SOFs for compositions above  $x \approx 14$ , with the 16i SOF exceeding the 24k SOF (Figure 7). This behavior also translates to, e.g., the heat capacity and the lattice parameter, for which the chemical ordering effect in Al-containing systems kicks in at higher temperatures than in Ga-based materials.

While the group 13 component is more dominant in the case of heat capacity, lattice parameter, and SOFs, the variation of lattice parameter and Ba OCD with composition is more sensitive to the group 14 component (Figure 9 and Figure S2 in

the Supporting Information). Here, both lattice constant and OCD in Si-based materials exhibit a pronounced positive correlation with Al/Ga content. By contrast, a much weaker variation with the opposite sign is obtained for the lattice constant in the Ge-containing systems.

We note that in the present work we made some approximations. Most notably, although experimental data shows vacancies to be present in substantial concentrations, in particular at the lower end of the composition range, we did not include these defects in our simulations. As our results are in good or very good agreement with experimental data, this reflects the fact that the inclusion of vacancies is of lesser importance for the properties considered here. Explicitly including vacancies implies moving from a quasi-binary (group 13/group 14) to a quasi-ternary (group-13/group 14/vacancy) system. While the inclusion of vacancies is beyond the scope of the present work, it can thus in principle be accomplished with cluster expansions and could be addressed in future work.

Generally, the present results demonstrate the potential of alloy cluster expansions to resolve microscopic features and reveal trends in complex inorganic materials that otherwise require extensive experimental work. This is not only very useful for understanding existing materials but ultimately creates an avenue for a more systematic exploration of a larger chemical space.

## ■ ASSOCIATED CONTENT

### Supporting Information

The Supporting Information is available free of charge on the ACS Publications website at DOI: 10.1021/acs.chemmater.7b02686.

Figures of 6c SOFs, lattice constants, and heat capacities as a function of temperature and composition; figures of effective cluster interactions for cluster expansions of the cell volume; and compilation of experimental SOF data included in Figure 7 in the form of a table (PDF)

Structures obtained by simulated annealing at different compositions (ZIP)

## ■ AUTHOR INFORMATION

### Corresponding Author

\*E-mail: [erhart@chalmers.se](mailto:erhart@chalmers.se).

### ORCID

Paul Erhart: 0000-0002-2516-6061

### Notes

The authors declare no competing financial interest.

## ■ ACKNOWLEDGMENTS

The authors gratefully acknowledge many helpful discussions with Joakim Brorsson and Anders Palmqvist. This work was funded by the Knut and Alice Wallenberg Foundation. Computer time allocations by the Swedish National Infrastructure for Computing at NSC (Linköping) and PDC (Stockholm) are gratefully acknowledged.

## ■ REFERENCES

- (1) Moss, G. P.; Smith, P. A. S.; Tavernier, D. Glossary of class names of organic compounds and reactivity intermediates based on structure (IUPAC Recommendations 1995). *Pure Appl. Chem.* **1995**, *67*, 1307–1375.
- (2) Rogl, P. *Thermoelectrics Handbook*; CRC Press: Boca Raton, FL, 2005; Chapter 32, pp 1–24.
- (3) Christensen, M.; Johnsen, S.; Iversen, B. B. Thermoelectric clathrates of type I. *Dalton Trans.* **2010**, *39*, 978–992.
- (4) Toberer, E. S.; Christensen, M.; Iversen, B. B.; Snyder, G. J. High temperature thermoelectric efficiency in  $\text{Ba}_8\text{Ga}_{16}\text{Ge}_{30}$ . *Phys. Rev. B: Condens. Matter Mater. Phys.* **2008**, *77*, 075203.
- (5) Nolas, G. S.; Cohn, J. L.; Slack, G. A.; Schujman, S. B. Semiconducting Ge clathrates: Promising candidates for thermoelectric applications. *Appl. Phys. Lett.* **1998**, *73*, 178–180.
- (6) Christensen, S.; Schmökel, M. S.; Borup, K. A.; Madsen, G. K. H.; McIntyre, G. J.; Capelli, S. C.; Christensen, M.; Iversen, B. B. Glass-like thermal conductivity gradually induced in thermoelectric  $\text{Sr}_8\text{Ga}_{16}\text{Ge}_{30}$  clathrate by off-centered guest atoms. *J. Appl. Phys.* **2016**, *119*, 185102.
- (7) Shevelkov, A. V.; Kovnir, K. In *Zintl Phases*; Fässler, T. F., Ed.; Springer: Berlin, Heidelberg, 2011; Structure and Bonding Chapter 139; pp 97–142.
- (8) Schäfer, H.; Eisenmann, B.; Müller, W. Zintl Phases: Transitions between Metallic and Ionic Bonding. *Angew. Chem., Int. Ed. Engl.* **1973**, *12*, 694–712.
- (9) Eisenmann, B.; Schäfer, H.; Zagler, R. Die Verbindungen  $\text{A}_8^{\text{II}}\text{B}_{16}^{\text{III}}\text{B}_{30}^{\text{IV}}$  ( $\text{A}^{\text{II}} = \text{Sr, Ba}$ ;  $\text{B}^{\text{III}} = \text{Al, Ga}$ ;  $\text{B}^{\text{IV}} = \text{Si, Ge, Sn}$ ) und ihre Käfigstrukturen. *J. Less-Common Met.* **1986**, *118*, 43–55.
- (10) Shevelkov, A. V.; Kovnir, K. A.; Zaikina, J. V. *The Physics and Chemistry of Inorganic Clathrates*, Springer Series in Materials Science; Springer: Dordrecht, 2014; pp 125–167.
- (11) Christensen, M.; Lock, N.; Overgaard, J.; Iversen, B. B. Crystal Structures of Thermoelectric n- and p-type  $\text{Ba}_8\text{Ga}_{16}\text{Ge}_{30}$  Studied by Single Crystal, Multitemperature, Neutron Diffraction, Conventional X-ray Diffraction and Resonant Synchrotron X-ray Diffraction. *J. Am. Chem. Soc.* **2006**, *128*, 15657–15665.
- (12) Blake, N. P.; Bryan, D.; Lattturner, S.; Möllnitz, L.; Stucky, G. D.; Metiu, H. Structure and stability of the clathrates  $\text{Ba}_8\text{Ga}_{16}\text{Ge}_{30}$ ,  $\text{Sr}_8\text{Ga}_{16}\text{Ge}_{30}$ ,  $\text{Ba}_8\text{Ga}_{16}\text{Si}_{30}$ , and  $\text{Ba}_8\text{In}_{16}\text{Sn}_{30}$ . *J. Chem. Phys.* **2001**, *114*, 10063–10074.
- (13) Christensen, M.; Iversen, B. B. Host Structure Engineering in Thermoelectric Clathrates. *Chem. Mater.* **2007**, *19*, 4896.
- (14) Roudebush, J. H.; de la Cruz, C.; Chakoumakos, B. C.; Kauzlarich, S. M. Neutron Diffraction Study of the Type I Clathrate  $\text{Ba}_8\text{Al}_x\text{Si}_{46-x}$ : Site Occupancies, Cage Volumes, and the Interaction between the Guest and the Host Framework. *Inorg. Chem.* **2012**, *51*, 1805–1812.
- (15) Ångqvist, M.; Lindroth, D. O.; Erhart, P. Optimization of the Thermoelectric Power Factor: Coupling between Chemical Order and Transport Properties. *Chem. Mater.* **2016**, *28*, 6877–6885.
- (16) Christensen, M.; Johnsen, S.; Søndergaard, M.; Overgaard, J.; Birkedal, H.; Iversen, B. B. Fast Preparation and Characterization of Quarternary Thermoelectric Clathrates. *Chem. Mater.* **2009**, *21*, 122–127.
- (17) Troppenz, M.; Rigamonti, S.; Draxl, C. Predicting Ground-State Configurations and Electronic Properties of the Thermoelectric Clathrates  $\text{Ba}_8\text{Al}_x\text{Si}_{46-x}$  and  $\text{Sr}_8\text{Al}_x\text{Si}_{46-x}$ . *Chem. Mater.* **2017**, *29*, 2414.
- (18) Sanchez, J. M.; Ducastelle, F.; Gratias, D. Generalized cluster description of multicomponent systems. *Phys. A* **1984**, *128*, 334.
- (19) Sanchez, J. M. Cluster expansion and the configurational theory of alloys. *Phys. Rev. B: Condens. Matter Mater. Phys.* **2010**, *81*, 224202.
- (20) Candes, E.; Wakin, M. An Introduction To Compressive Sampling. *IEEE Signal Processing Magazine* **2008**, *25*, 21.
- (21) Yin, W.; Osher, S.; Goldfarb, D.; Darbon, J. Bregman Iterative Algorithms for  $l_1$ -Minimization with Applications to Compressed Sensing. *SIAM Journal on Imaging Sciences* **2008**, *1*, 143–168.
- (22) Goldstein, T.; Osher, S. The Split Bregman Method for  $L_1$ -Regularized Problems. *SIAM Journal on Imaging Sciences* **2009**, *2*, 323–343.
- (23) Nelson, L. J.; Hart, G. L. W.; Zhou, F.; Ozolins, V. Compressive sensing as a new paradigm for model building. *Phys. Rev. B: Condens. Matter Mater. Phys.* **2013**, *87*, 035125.

(24) Okamoto, N. L.; Kishida, K.; Tanaka, K.; Inui, H. Crystal structure and thermoelectric properties of type-I clathrate compounds in the Ba-Ga-Ge system. *J. Appl. Phys.* **2006**, *100*, 073504.

(25) We note that we have previously shown<sup>15</sup> that a unit cell is sufficient to obtain the SOFs with good accuracy.

(26) Sadigh, B.; Erhart, P. Calculations of excess free energies of precipitates via direct thermodynamic integration across phase boundaries. *Phys. Rev. B: Condens. Matter Mater. Phys.* **2012**, *86*, 134204.

(27) Blöchl, P. E. Projector augmented-wave method. *Phys. Rev. B: Condens. Matter Mater. Phys.* **1994**, *50*, 17953.

(28) Kresse, G.; Joubert, D. From ultrasoft pseudopotentials to the projector augmented-wave method. *Phys. Rev. B: Condens. Matter Mater. Phys.* **1999**, *59*, 1758.

(29) Kresse, G.; Furthmüller, J. Efficient iterative schemes for ab initio total-energy calculations using a plane-wave basis set. *Phys. Rev. B: Condens. Matter Mater. Phys.* **1996**, *54*, 11169.

(30) Kresse, G.; Furthmüller, J. Efficiency of ab-initio total energy calculations for metals and semiconductors using a plane-wave basis set. *Comput. Mater. Sci.* **1996**, *6*, 15–50.

(31) Perdew, J. P.; Burke, K.; Ernzerhof, M. Generalized Gradient Approximation Made Simple. *Phys. Rev. Lett.* **1996**, *77*, 3865–3868; erratum. *Phys. Rev. Lett.* **1997**, *78*, 1396.

(32) Nelson, L. J.; Ozoliņš, V.; Reese, C. S.; Zhou, F.; Hart, G. L. W. Cluster expansion made easy with Bayesian compressive sensing. *Phys. Rev. B: Condens. Matter Mater. Phys.* **2013**, *88*, 155105.

(33) Togo, A.; Oba, F.; Tanaka, I. First-principles calculations of the ferroelastic transition between rutile-type and CaCl<sub>2</sub>-type SiO<sub>2</sub> at high pressures. *Phys. Rev. B: Condens. Matter Mater. Phys.* **2008**, *78*, 134106.

(34) May, A. F.; Toberer, E. S.; Saramat, A.; Snyder, G. J. Characterization and analysis of thermoelectric transport in *n*-type Ba<sub>8</sub>Ga<sub>16-x</sub>Ge<sub>30+x</sub>. *Phys. Rev. B: Condens. Matter Mater. Phys.* **2009**, *80*, 125205.

(35) Reardon, H.; Blichfeld, A. B.; Kasai, H.; Yin, H.; Bojesen, E. D.; Iversen, B. B. Revealing the slow decomposition kinetics of type-I clathrate Ba<sub>8</sub>Ga<sub>16</sub>Ge<sub>30</sub>. *Phys. Chem. Chem. Phys.* **2017**, *19*, 15734.

(36) Nataraj, D.; Nagao, J. Structure and Raman scattering study on Ba<sub>8</sub>Ga<sub>x</sub>Si<sub>46-x</sub> (*x* = 10 and 16) type I clathrates. *J. Solid State Chem.* **2004**, *177*, 1905–1911.

(37) Bienten, A.; Iversen, B.; Bryan, J.; Stucky, G.; Palmqvist, A.; Schultz, A.; Henning, R. Maximum entropy method analysis of thermal motion and disorder in thermoelectric clathrate Ba<sub>8</sub>Ga<sub>16</sub>Si<sub>30</sub>. *J. Appl. Phys.* **2002**, *91*, 5694–5699.

(38) Bienten, A.; Nishibori, E.; Paschen, S.; Iversen, B. Crystal structures, atomic vibration, and disorder of the type-I thermoelectric clathrates Ba<sub>8</sub>Ga<sub>16</sub>Si<sub>30</sub>, Ba<sub>8</sub>Ga<sub>16</sub>Ge<sub>30</sub>, Ba<sub>8</sub>In<sub>16</sub>Ge<sub>30</sub>, and Sr<sub>8</sub>Ga<sub>16</sub>Ge<sub>30</sub>. *Phys. Rev. B: Condens. Matter Mater. Phys.* **2005**, *71*, 144107.

(39) Christensen, M.; Iversen, B. Investigations of Clathrate Type I Structures: Ba<sub>8</sub>Ga<sub>16</sub>Si<sub>30</sub>. In *Proceedings of the 4th European Conference on Thermoelectrics*; Rowe, D. M., Ed.; Cardiff: 2006.

(40) Bobnar, M.; Böhme, B.; Wedel, M.; Burkhardt, U.; Ormeci, A.; Prots, Y.; Drathen, C.; Liang, Y.; Nguyen, H. D.; Baitinger, M.; Grin, Y. Distribution of Al atoms in the clathrate-I phase Ba<sub>8</sub>Al<sub>x</sub>Si<sub>46-x</sub> at *x* = 6.9. *Dalton Trans.* **2015**, *44*, 12680–12687.

(41) Erhart, P.; Albe, K. Thermodynamics of mono- and di-vacancies in barium titanate. *J. Appl. Phys.* **2007**, *102*, 084111.